COPPE
UFRJ
Instituto Alberto Luiz Coimbra de
Pós-Graduação e Pesquisa de Engenharia

HYBRID CONTROL SCHEME FOR VSC PRESENTING BOTH GRID-FORMING AND GRID-FOLLOWING CHARACTERISTICS

Luiz André Moysés Lima

Tese de Doutorado apresentada ao Programa de Pós-graduação em Engenharia Elétrica, COPPE, da Universidade Federal do Rio de Janeiro, como parte dos requisitos necessários à obtenção do título de Doutor em Engenharia Elétrica.

Orientador: Edson Hirokazu Watanabe

Rio de Janeiro
Dezembro de 2022

HYBRID CONTROL SCHEME FOR VSC PRESENTING BOTH GRID-FORMING AND GRID-FOLLOWING CHARACTERISTICS

Luiz André Moysés Lima

TESE SUBMETIDA AO CORPO DOCENTE DO INSTITUTO ALBERTO LUIZ COIMBRA DE PÓS-GRADUAÇÃO E PESQUISA DE ENGENHARIA DA UNIVERSIDADE FEDERAL DO RIO DE JANEIRO COMO PARTE DOS REQUISITOS NECESSÁRIOS PARA A OBTENÇÃO DO GRAU DE DOUTOR EM CIÊNCIAS EM ENGENHARIA ELÉTRICA.

Orientador: Edson Hirokazu Watanabe

Aprovada por: Prof. Edson Hirokazu Watanabe
Prof. Glauco Nery Taranto
Prof. Luís Guilherme Barbosa Rolim
Prof. José Antenor Pomílio
Prof. Luiz Antônio de Souza Ribeiro

RIO DE JANEIRO, RJ – BRASIL
DEZEMBRO DE 2022

Lima, Luiz André Moysés

Hybrid Control Scheme for VSC Presenting Both Grid-Forming and Grid-Following Characteristics/Luiz André Moysés Lima. – Rio de Janeiro: UFRJ/COPPE, 2022.

XXI, 138 p.: il.; 29, 7cm.

Orientador: Edson Hirokazu Watanabe

Tese (doutorado) – UFRJ/COPPE/Programa de Engenharia Elétrica, 2022.

Referências Bibliográficas: p. 130 – 138.

1. DC transmission. 2. frequency support. 3. grid following. 4. grid forming. 5. hybrid control. 6. inertial response. 7. renewable energy. I. Watanabe, Edson Hirokazu. II. Universidade Federal do Rio de Janeiro, COPPE, Programa de Engenharia Elétrica. III. Título.

Agradecimentos

Ao Professor Watanabe, pela orientação, paciência e por sua maneira leve, porém precisa e inteligente, de lidar com todos os assuntos. É uma grande inspiração.

À minha esposa, Bia, pelo companheirismo e apoio incondicionais, sem os quais nada disso seria possível.

A meus pais Beth e Luiz, minha avó Maria, meu irmão Rodrigo, e todos mais da família, pelo carinho e compreensão desde sempre.

A todos os meus amigos, pela diversão e descontração, que são essenciais para deixar a mente mais leve. E também para desabafar quando a paciência com os estudos está em baixa.

A todos que participaram direta ou indiretamente deste trabalho, minha mais profunda e sincera gratidão!

"Quando escolho ver o lado bom das coisas, não estou sendo inocente. É estratégico e necessário. [...] A única coisa que sei é que devemos ser gentis. É assim que eu luto."

Waymond Wang - *Tudo em Todo Lugar ao Mesmo Tempo*

Resumo da Tese apresentada à COPPE/UFRJ como parte dos requisitos necessários para a obtenção do grau de Doutor em Ciências (D.Sc.)

SISTEMA DE CONTROLE HÍBRIDO PARA VSC COM CARACTERÍSTICAS DE FORMADOR E SEGUIDOR DE REDE

Luiz André Moysés Lima

Dezembro/2022

Orientador: Edson Hirokazu Watanabe

Programa: Engenharia Elétrica

Fontes renováveis de energia são vitais para combater as mudanças climáticas, mas podem trazer problemas de estabilidade para os sistemas elétricos onde estão instaladas. Elas são conectadas por meio de conversores com controle Seguidor de Rede (*Grid Follower* - GFL), necessário para maximizar sua geração. Entretanto, GFLs possuem capacidade de suporte à rede muito limitada.

Este trabalho propõe o Conversor de Controle Híbrido (*Hybrid Control Converter* - HCC), um novo tipo de sistema de controle para VSC (Conversores Fonte de Tensão, ou *Voltage-Source Converters*). O HCC emula a operação de dois conversores individuais, que estariam operando em paralelo e simultaneamente, sendo um GFL e o outro com controle Formador de Rede (*Grid Former* - GFM). Assim, o HCC apresenta características de ambos ao mesmo tempo: o controle de potência rápido e preciso do GFL, e as capacidades de suporte à rede e black-start do GFM.

O modelo matemático do HCC é desenvolvido e análises de estabilidade e robustez são apresentadas. Resultados mostram que o HCC é tão estável e robusto quanto as estratégias de controle usuais (GFL/GFM) para os casos analisados.

Duas possíveis applicações do HCC são apresentadas. A primeira lida com capacidade de suporte à rede de turbinas eólicas. É mostrado que o HCC confere performance superior à turbina, comparado com o controle tradicional (GFL), levando a transitórios de frequência mais amenos. A segunda aplicação mostra que o HCC permite uma conexão autônoma entre redes ac que estejam conectadas por um sistema HVDC ramificado. Assim, o sistema HVDC apresenta suporte automático às redes ac, permitindo um compartilhamento natural de geração e carga entre as mesmas, sem a necessidade de ações específicas de controle pelo operador do sistema.

Abstract of Thesis presented to COPPE/UFRJ as a partial fulfillment of the requirements for the degree of Doctor of Science (D.Sc.)

HYBRID CONTROL SCHEME FOR VSC PRESENTING BOTH GRID-FORMING AND GRID-FOLLOWING CHARACTERISTICS

Luiz André Moysés Lima

December/2022

Advisor: Edson Hirokazu Watanabe

Department: Electrical Engineering

Renewable energy sources are vital to fight against climate change, but they may bring stability issues to the electrical systems. They are connected to the grid through converters with grid-following (GFL) control, which is needed to maximize their generation. The problem is that GFLs have very limited grid support capability.

This work proposes the Hybrid Control Converter (HCC), a novel kind of VSC control structure. It enables the converter to emulate the operation of two individual converters working in parallel and simultaneously, being one GFL and the other with grid-forming (GFM) control. This way, the HCC can show behavioral characteristics of both at the same time: the fast and accurate power control of the GFL, and the inherent support and black-start capabilities of the GFM.

The full mathematical model of the HCC is developed, and stability and robustness studies are also conducted. Results show that the HCC is at least as stable and robust as usual converter control strategies (GFL/GFM) for the analyzed cases.

Two possible applications for the HCC are presented. The first one is related to grid support of wind turbines (WT). Results show that, when applied to WT converters, the HCC presents superior performance when compared to the conventional GFL, resulting in a smaller grid frequency drop during transients. The second application shows that the HCC allows for autonomous connection of multiple distinct ac systems using a meshed HVDC transmission system. This enables automatic frequency support, and also generation and load sharing between the ac grids, without requiring any specific action by the system operator.

Table of Contents

List of Figures

List of Tables

List of Symbols

This list includes the most relevant symbols used throughout this work. For simplicity and to avoid an excessively long list, the following notation rules are applied to the symbols of voltage and current:

- lower-case is applied for time-domain variables, omitting the indicator "(t)" for conciseness, such as: $v(t) \rightarrow v$;
- upper-case is applied for frequency-domain variables, omitting the indicator "(s)" for conciseness, such as: $V(s) \rightarrow V$;
- bold is applied for vector notations of 3-phase variables (in either the *abc*- or *dq*-frames), such as: $\boldsymbol{v}(t) = [v_a(t), v_b(t), v_c(t)]^T$;
- in principle, all variables are represented in the *abc*-frame. When the *dq*-frame is used, it is indicated in a subscript. The *abc*-frame can also be indicated in a subscript in specific cases to emphasize it, such as: $\boldsymbol{v}_{dq}$, $\boldsymbol{v}_{abc}$;
- variables that exist for converter 1 and converter 2 (in the two-converter system) are described with a subscript "12" that means *1 or 2*, to avoid duplicity, such as: $\boldsymbol{v}_1, \boldsymbol{v}_2 \rightarrow \boldsymbol{v}_{12}$;
- reference values used in control systems are represented by adding a superscript to the base variable, such as: $\boldsymbol{v}^*$.

f	Grid frequency, in Hz, p. 20
f^*_{drp}	Reference frequency modified by the droop, p. 23
F_x	Auxiliary transfer functions used in the stability analysis, where $1 \leq x \leq 4$, p. 73
G_x	Auxiliary transfer functions used in the stability analysis, where $1 \leq x \leq 5$, p. 74
$\boldsymbol{i}_{12}$	Output current of converter 1 or 2 (in the two-converter system), p. 41
$\boldsymbol{i}_{conv}$	Output current of a converter or group of converters, p. 15

$\boldsymbol{i}_{loop}$	Loop current used in the calculations of the two-converter system, p. 36
k_{12}	Impedance ratio of converter 1 or 2 (of the two-converter system), p. 37
$k_{drp,f}$	Gain of the frequency droop, p. 23
$k_{drp,p}$	Gain of the active power droop, p. 20
$k_{drp,q}$	Gain of the reactive power droop, p. 20
$k_{drp,V}$	Gain of the voltage droop, p. 23
k_L	Inductance mismatch factor, p. 86
k_p	Proportional gain of a PI controller, p. 18
$k_{p,i}$	Proportional gain of the current control loop's PI controller, p. 26
$k_{p,v}$	Proportional gain of the voltage control loop's PI controller, p. 26
k_{RL}	Symmetrical mismatch factor, p. 86
k_R	Resistance mismatch factor, p. 86
L_{12}	Filter inductance of converter 1 or 2 (in the two-converter system), p. 33
$L_{eq,2conv}$	Equivalent inductance of the two-converter system, p. 38
L_f	Converter filter inductance, p. 26
L_{tot}	Total inductance, defined as $L_t = L_1 + L_2$, p. 66
n	Number of output signals generated by the switching algorithm, p. 20
Ω	Transformation matrix, based on the Park Transform, p. 62
ω	Grid frequency, in rad/s, p. 18
p	Instantaneous real power, p. 18
p^*_{drp}	Reference instantaneous real power modified by the droop, p. 19

PI_{12}	PI-controller of the converter 1 or 2 (in the two-converter or virtual systems), p. 72
q	Instantaneous imaginary power, p. 18
q^*_{drp}	Reference instantaneous imaginary power modified by the droop, p. 19
R_{12}	Filter resistance of converter 1 or 2 (in the two-converter system), p. 33
$R_{eq,2conv}$	Equivalent resistance of the two-converter system, p. 38
R_f	Converter filter resistance, p. 26
R_{tot}	Total resistance, defined as $R_t = R_1 + R_2$, p. 66
TF_{open}	Equivalent open-loop transfer function, p. 70
θ	Phase angle of the grid voltage, estimated by the PLL, p. 18
T_i	Integral time constant of a PI controller, p. 18
$T_{i,i}$	Time constant of the current control loop's PI controller, p. 26
$T_{i,v}$	Time constant of the voltage control loop's PI controller, p. 26
T	Park Transform matrix, p. 62
T_Σ	Converter equivalent time delay, p. 26
$\boldsymbol{v}_{12}$	Output voltage of converter 1 or 2 (in the two-converter system), p. 33
V_{DC}	DC-link voltage, p. 93
$\boldsymbol{v}_{eq}$	Equivalent voltage of a generic electrical system, p. 34
$\boldsymbol{v}_{eq,1conv}$	Equivalent voltage of the single-converter system, p. 35
$\boldsymbol{v}_{eq,2conv}$	Equivalent voltage of the two-converter system, p. 35
$\boldsymbol{v}_{HCC}$	Output voltage of the HCC, p. 33
$\boldsymbol{v}_{oc}$	Open-circuit voltage, used in the two-converter system calculations, p. 36
$\boldsymbol{v}_{out}$	Converter output voltage, p. 15

$\boldsymbol{v}_{pcc}$	Voltage at the PCC, p. 15
$\hat{V}^*$	Reference voltage amplitude, p. 20
$\hat{V}^*_{drp}$	Reference voltage amplitude modified by the droop, p. 23
X_{12}	Filter reactance of converter 1 or 2 (in the two-converter system), p. 36
Z_{12}	Filter impedance of converter 1 or 2 (in the two-converter system), p. 33
Z_{eq}	Equivalent impedance of a generic electrical system, p. 34
$Z_{eq,1conv}$	Equivalent impedance of the single-converter system, p. 35
$Z_{eq,2conv}$	Equivalent impedance of the two-converter system, p. 35

List of Acronyms

AC	Alternating Current, p. 13
BESS	Battery Energy Storage System, p. 5
BIBO	Bounded-Input Bounded-Output, p. 60
DBS	Dynamic Braking System, p. 126
DC	Direct Current, p. 13
DFIG	Doubly-Fed Induction Generator, p. 8
ESS	Energy Storage System, p. 4
GFL	Grid-Following Converter, p. 6
GFM	Grid-Forming Converter, p. 6
GSC	Grid-Side Converter, p. 99
HAWT	Horizontal-Axis Wind Turbine, p. 97
HCC	Hybrid Control Converter, p. 11
HVDC	High-Voltage Direct Current, p. 9
IBR	Inverter-Based Resource, p. 4
IEA	International Energy Agency, p. 1
IGBT	Insulated-Gate Bipolar Transistor, p. 14
IGCT	Integrated Gate-Commutated Thyristor, p. 14
ISO	Independent System Operator, p. 2
LCC	Line Commutated Converter, p. 113
LTI	Linear Time-Invariant, p. 77

MMC	Modular Multilevel Converter, p. 15
MPPT	Maximum Power-Point Tracking, p. 2
MVDN	Medium-Voltage Distribution Network, p. 97
NPC	Neutral-Point Clamped Converter, p. 15
OLTC	On-Load Tap Changer Transformer, p. 115
PCC	Point of Common Coupling, p. 15
PEC	Power Electronics Converter, p. 4
PI	Proportional-Integral Controller, p. 18
PLL	Phase-Locked Loop, p. 7
PR	Proportional-Resonant Controller, p. 21
PV	Photovoltaic (panel), p. 2
PWM	Pulse Width Modulation, p. 91
RES	Renewable Energy Source, p. 1
RSC	Rotor-Side Converter, p. 99
RoCoF	Rate of Change of Frequency, p. 3
SG	Synchronous Generator, p. 2
SI	Synthetic Inertia, p. 102
SM	Submodule, p. 20
SSC	Stator-Side Converter, p. 100
STATCOM	Static Synchronous Compensator, p. 9
SoC	State-of-Charge, p. 6
TL	Transmission Line, p. 106
UPS	Uninterruptible Power Supply, p. 25
VSC	Voltage Source Converter, p. 14
VSG	Virtual Synchronous Generator, p. 7
VSM	Virtual Synchronous Machine, p. 24
WT	Wind Turbine, p. 2

Chapter 1

Introduction

1.1 Motivation

1.1.1 Renewable Energy Sources and Associated Challenges

Power generation from Renewable Energy Sources (RES) has drastically increased in the past decade. As the world rallies to find solutions for the global climate crisis and avoid irreversible climate change, renewable energy has been the top candidate to reduce the emission of CO2 and other greenhouse gases. Wind and solar generation are the fastest-expanding RESs [1], as shown in Figure 1.1, with progressively lower investment costs and a technology that has been getting increasingly mature over time [2].

The drastic increase in renewable generation has even led to the decommission of conventional fossil-fuel-based power plants in some countries [2]. The International Energy Agency (IEA) estimates that, if we are to achieve the sustainable development goals discussed and agreed upon in the past years, the share of RESs in the global energy matrix must keep expanding aggressively, rising from 30% (in 2020) to around 60% in 2030 [3]. Aside from that, there is the ongoing energy transition, where electric vehicles are overtaking traditional fuel-based transportation, domestic heating systems are shifting from gas- or oil-based to electric, and so on. This paradigm shift is going to skyrocket the energy consumption in the coming decades, increasing even more the demand for renewable energy.

Even though RESs are vital to tackle the climate issue, they bring new challenges when compared to conventional power plants. Wind generation, for instance, directly depends on the wind speed that the Wind Turbines (WT) experience. Photovoltaic (PV) panels generate power proportionally to the solar irradiation to which they are subject. The stochastic variations of wind and sunlight lead to a variable power generation, which may, in turn, lead to instantaneous unbalance between generated power and demand [4, 5]. At low penetration level, this variability in

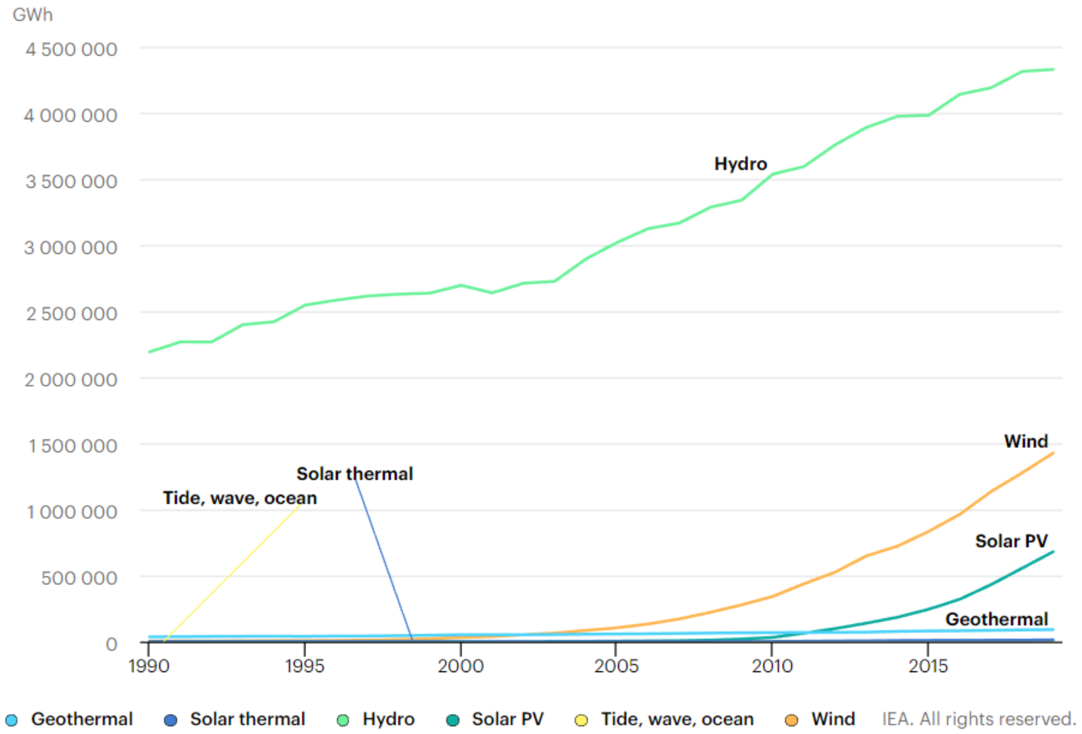

Figure 1.1: Evolution of the global energy generation by RESs [1].

generation is not very relevant, being comparable to regular variations in the energy demand [5]. Therefore, conventional units such as hydro or thermal Synchronous Generators (SG) can guarantee the electrical system stability and reliability. The problem arises when the penetration level of RESs increases, and the existing SGs are not enough to keep the system operating in a reliable manner.

Wind turbines and PV panels usually generate the maximum power they can extract from the wind or sunlight at any given time, following a Maximum Power-Point Tracking (MPPT) algorithm. This characteristic has made them quite competitive in terms of cost, but it introduces other issues. If they are always operating at their maximum possible power output, there is no possibility of further increasing the power delivered to the grid, although it can be reduced by means of inverter control. Besides that, since RES generation is directly dependent on the natural resource at any given time, these energy sources are by definition not dispatchable [5], which means that their generation level cannot be defined freely by the Independent System Operator (ISO). On the other hand, with SGs, it is usually possible to increase or decrease their generation at any given time. This is done by actuators that control the input water flow or steam, depending on the type of machine, while respecting their rated power. They are dispatchable, as the ISO can request any specific generation level at any given time, and the SGs will follow the dispatch order.

The ISO has to plan the day-ahead and the intraday system operation and also schedule, in the most economical way possible, the amount of reserve power available. Since RESs are becoming more prevalent and given the fact that they are not dispatchable, they pose a great challenge for power systems operation and planning. One of the main factors related to grid stability that is taken into account by the ISO is the frequency stability. When there is a momentary mismatch between generation and demand, the frequency of the electrical system varies. The usual way to tackle this issue is with traditional SGs, that quickly adapt their output power to match the demand, providing the necessary support to the grid. They have different layers of frequency support, with different goals. Reserve units, usually thermal generation based on SGs, are also kept operating to increase the safety margin of the system if extra generation is required. It is costly to keep these units operating as reserve, but they are required especially in grids with high RES penetration to compensate for the variations in RESs production.

Figure 1.2 illustrates different stages of frequency support, following a given grid contingency [6]. Initially, the inertial response of the generators dictates the transient response of the grid frequency right after the fault. When the frequency drops below an acceptable threshold, the primary response is automatically triggered on all generators that are able to provide this kind of support. It increases their output power, which stabilizes the system at a different (lower) frequency level. After some time, the secondary frequency support is activated for the generators that have this capability, and extra power is supplied to the grid. This brings to frequency closer to the nominal value. Finally, the tertiary frequency support is activated by the system operator, that performs redispatch of the available generators to achieve a more stable operating point and return the frequency to its nominal value, usually also taking into consideration economical aspects. In the figure, the zones depicting different types of frequency support are slanted, to emphasize that their effect is not instant from the moment they are activated.

During the first moments after a fault, the Rate of Change of Frequency (RoCoF) is dictated by the system inertia. Conventional SGs are directly coupled to the electrical grid, and their mechanical inertia inherently reduces the rate at which the grid frequency drops. The mechanical rotational energy of the SGs serves as a momentary buffer, avoiding large grid frequency excursions before the support functionality is activated to halt its drop.

For RESs, the story is different. Since they are not dispatchable, they cannot properly provide grid support, increasing their generation if and as needed. Besides that, they are usually connected to the grid using Power Electronics Converters (PEC), thus being classified as Inverter-Based Resources (IBR). The PEC is needed to optimize the RES's generation, enabling them to generate the maximum amount of power they can on any given moment regardless of the grid conditions. This

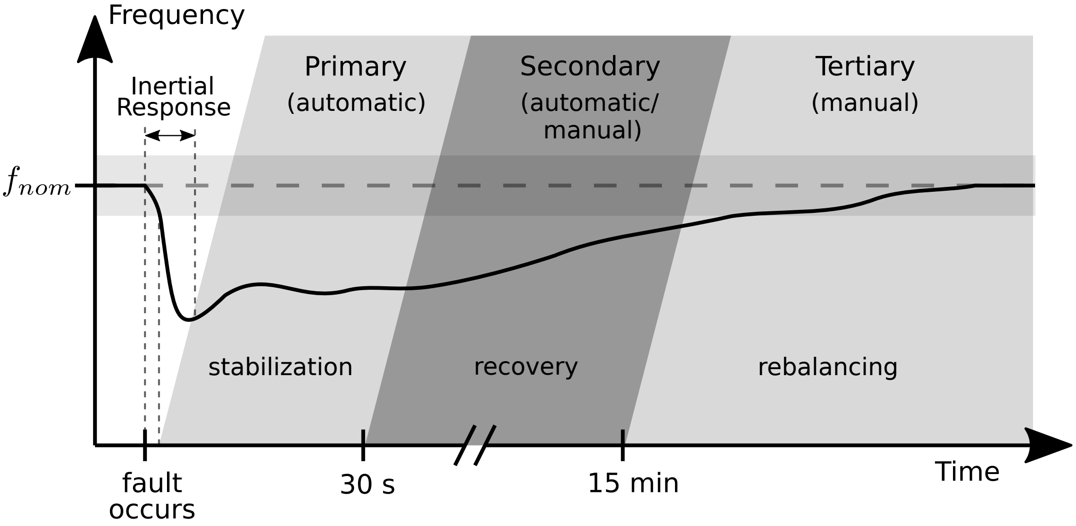

Figure 1.2: Stages of frequency support after a fault.

way, their generation is decoupled from the grid state, and they present no inherent inertial behavior to help the system stability [7–10]. With an increasing portion of the electrical generation being comprised of IBRs, the overall grid inertia and frequency support capability are steadily decreasing, and transient oscillations are becoming more severe. With low system inertia, instantaneous mismatches between generation and demand lead to larger and faster voltage and/or frequency variations, which reduce the system stability and reliability and may cause the activation of protection schemes such as load shedding.

These issues related to frequency support and grid stability are especially relevant when more than 65% of the generation is provided via IBRs [10]. Even though that is a very high value for most electrical networks in the world, subsystems of large grids already reach this threshold and may have their reliability compromised. For example, Germany and Denmark have already had 100% of their instantaneous generation via IBRs in some situations [10]. In their case, the European grid can provide the necessary support, but as RESs penetration increase, these issues will become more frequent and relevant.

1.1.2 Possibilities to Enable Grid Support Capability on RESs

To tackle the grid stability issues and enable frequency support for RESs, three main approaches have been highlighted in recent literature: to implement de-rated operation; to add support functionality in the PEC control system; and to implement Energy Storage Systems (ESSs) as reserve.

The first one consists of operating the WT or PV panel below the maximum power point so that, at any given moment, it can increase its power generation if needed, assuming enough headroom is available. This can be done by means of blade pitch or operating speed control in WTs, or by voltage control in PV panels. Since this approach consists on not utilizing the maximum power capability during steady-state operation, it is highly undesirable from an economic perspective. Nevertheless, there are studies that try to mitigate this issue. For example, Su et al. [11] propose a technique to optimize de-rated operation on a solar farm and keep an optimum amount of reserve power for primary frequency support. An algorithm that estimates the amount of inertia available in the grid (from other sources) dictates the necessary amount of reserve power, thus keeping the de-rated operation to a minimum when grid conditions are favorable.

The second approach to tackle grid stability issues consists on adding new functionalities to the PEC's control system. For example, for WTs, it can emulate an inertial response by using their stored kinetic energy. This leads to a momentary increase in delivered power (that usually lasts up to about 10 s), accompanied by a decrease in rotor speed. When the controller's emulated inertial response ends, the WT resumes regular operation but with a lower speed, and thus a lower output power than before. Even though this technique is advantageous because it does not require any extra components, this behavior could lead to a second wave of instability, depending on the electrical system conditions, due to the reduced power output at a second moment [12].

The third approach to tackle grid stability issues employs ESSs as the source of extra energy. They can be rapidly regulated to consume or provide extra active and reactive power to the grid when required, helping mitigate voltage and frequency transients. The ESSs presented in recent literature to be used together with RESs are mainly Battery Energy Storage Systems (BESS). Other types of ESS exist, such as flywheel, supercapacitor and pumped-hydro, but the main advantages of the BESS are its fast response time, flexible and accurate output power control, short installation time and a recent trend of cost reduction [4]. Similarly to most RESs, a BESS is connected to the grid via a PEC, which controls its output power. Therefore, it is also classified as an IBR.

Zhao et al. [5] present a broad review of ESSs integrated with wind power. They argue that, because of the ESSs fast response time, they could be more advantageous than conventional reserve units when compensating for fluctuations in RESs power generation, in some cases. They also mention that BESSs can provide various ancillary services, such as (but not limited to):

- emulated inertial response [6, 8], so that WTs do not have to change their operation from MPPT mode, ensuring maximum energy capture;
- reliable power dispatch [8], where the BESS compensates for the mismatch

between the dispatch order and the actual wind/solar generation;

- generation time-shifting [4, 13], where the ESS is charged (storing energy generated from a RES) when the energy prices are lower and discharged when prices are higher;
- primary frequency support [4, 8, 14], providing extra power when the measured grid frequency drops below an acceptable threshold.

It should be noted that ESSs can provide multiple ancillary services at once, depending on their power and energy rating, technology and cost. Multiple types of ESS can be combined to exploit their different characteristics and optimize the types of ancillary services they can provide. Besides that, different techniques to tackle the frequency support issue can also be employed together. For example, Tan and Zhang [14] propose a combination of a de-rated WT with a BESS to provide frequency support in different time scales. They argue that the de-rated WT can provide longer-term support, while the BESS covers the short-term due to its faster actuation speed. The ensemble can then cover different needs, from primary frequency support to day-ahead reserve market.

1.1.3 Types of Converter Control and Their Limitations

The way the PEC's control system is implemented for an IBR has a large impact on its dynamic performance. Overall, there are two different implementations, which result in the PEC being classified as a Grid-Following Converter (GFL) or Grid-Forming Converter (GFM) [15]. The GFL works essentially as a current source, since it closely controls the current (and thus power) that it provides to the grid. On the other hand, the GFM main control targets are voltage amplitude and frequency, so it behaves like a voltage source connected to the grid [16]. More detail on these control system implementations is provided in Chapter 2. Typically, RESs and BESSs are implemented with GFL, which accurately controls their output power to follow a reference value. This is needed to guarantee the RESs MPPT operation and to ensure that a BESS current and State-of-Charge (SoC) stay within safety limits.

The approaches presented in the previous section are attempts at providing/improving the grid support capability of IBRs using the GFL technique, since they are all based on controlling the output power of either the RES or the ESS. Unfortunately, studies show that, even with the aforementioned techniques, frequency support provided by IBRs that employ a GFL may not be enough for electrical grids with high penetration of RESs. In this scenario, the GFM technique has been drawing increasing interest from the scientific community.

Matevosyan et al. [10] argue that, especially for islanded or weakly interconnected systems, the need for fast active power recovery and frequency support is of great importance. Unlike GFMs, GFLs need sufficient system strength to successfully provide such support, because otherwise their Phase-Locked Loop (PLL) algorithm, used to measure the system frequency, may lose synchronization. As GFMs behave like a voltage source, they provide an immediate response to grid changes. This exact behavior is not attainable with GFLs even if extra control loops are implemented, for example to include inertia emulation. As they need measurements of voltage and frequency, their overall response to grid changes when compared to GFMs is inherently slower. GFLs can only provide enough frequency support if there is a sufficient amount of SGs or GFMs connected to the grid, guaranteeing a minimum level of inertia, so that the initial RoCoF at the first 100ms of a fault is not too risky for grid stability. Recent studies aim to improve the GFL stability issue in weak grids [17–19], but the GFL will always inherently need other energy sources to form the grid it is connected to.

Lasseter et al. [20] mention that system operators from Ireland, Texas and Australia are already facing issues related to the instantaneous high levels of RES generation, leading to low system inertia during certain periods of the day. By comparing the transient response of a GFL and a GFM, the paper shows that a large presence of GFLs reduces the system damping, leading to more severe transients after a grid fault. It demonstrates that it is possible to limit the GFM power between reference minimum and maximum values, which can help with overcurrent protection and could enable RESs to participate in frequency regulation using GFM if they work de-rated, with some adaptations.

The trend to change from GFL to GFM seems to be a feasible solution to enable power systems to work with high penetration on IBRs. And ways to integrate RESs and BESSs with GFM are being thoroughly investigated.

For example, BESSs with GFM could enable islanded microgrid operation [21] while keeping RESs operating as usual, following their MPPT control. Another possibility is to integrate them with GFM-based WTs, as proposed by Ma et al. [22]. The study assumes an ideal BESS that can control the dc-link voltage to its nominal value, rapidly charging/discharging according to power fluctuations. The rotor-side converter follows an MPPT algorithm, but it may curtail the generation in case of very high BESS SoC. The grid-side converter operates as a Virtual Synchronous Generator (VSG), using GFM control. It includes a power limitation loop that depends on the MPPT, dispatch order (assumed every 5-min) and BESS SoC.

But grid support capabilities remain a challenge. Yu et al. [23] present an overview of GFM techniques proposed to WTs. The study shows different methodologies that can be applied to the grid-side converter of the back-to-back configuration, enabling different grid support capabilities. However, it highlights various challenges to these approaches. Since the grid-side converter is now a GFM that also controls the dc-link voltage, the output active power variations that may happen to compensate for grid frequency deviation could be passed to the rotor-side, affecting MPPT operation. It also mentions that auxiliary ESSs are necessary if the GFM-based WT is to provide grid support or black-start services. Besides that, the transition from GFL to GFM mode should be further investigated to avoid unnecessary tripping of WTs.

Rodriguez-Amenedo et al. [24] mention that, since wind farms currently do not have black-start capability, they do not participate in system restoration when a blackout happens. It proposes a way to provide this capability to Doubly-Fed Induction Generator (DFIG) WTs, by employing a GFM at the rotor-side of the back-to-back unit. Instead of controlling the torque via the rotor current, the converter controls the torque via the angle and magnitude of the rotor flux. This way, the turbine generation matches the active and reactive power required by the load, enabling the system black-start. The study proposes that the turbine should change its control back to usual GFL, to enable MPPT after the system is restored. Since GFL control is faster than GFM for tracking reference values of power / current, it seems that, if the GFM mode of operation were kept during steady-state operation of the WT, the MPPT algorithm could have its accuracy compromised. Other capabilities such as frequency support were not investigated.

It appears to be a consensus that the GFM can be a vital component for enabling higher penetration of RESs in electrical grids. Studies show that it provides better support than the GFL, which may be mandatory for future systems with very low or even zero real inertia. There are several different ways to implement GFM control [15, 23, 25–27], but there is no clear winner or one-fits-all solution. The GFM has been the focus of many recent studies that aim to better understand how it works and to push its application boundaries, regarding subjects such as fault ride-through [28], grid oscillations attenuation [24, 29], power coupling [30] and stability analyses [31, 32]. What is certain is that the PEC's control methodology, for RESs and ESSs, is extremely important, and may result in completely different characteristics and capabilities for the equipment.

The main limiting factor of the GFM is that it requires an energy buffer to work properly, because the extra energy it consumes/supplies to the grid must be stored somewhere. Besides that, as it works, the output power is not the primary control action, since the GFM is actually aiming to control the grid voltage and frequency. This could lead to oscillations of the dc-link voltage and also affect the MPPT algorithm, which is highly undesirable. The GFL, on the other hand, can accurately control its output power, which is needed for proper operation of a BESS or RES. Even for RESs that could have both control methodologies, the transition between these two modes of operation when grid conditions change is sensitive and could lead to instability.

Therefore, a different control technique, merging the advantages of both the GFL and GFM, would be useful for a wide range of applications, such as (but not limited to) wind turbines, solar panels, energy storage systems and HVDC systems. More detail about possible applications is discussed in the following chapters.

1.1.4 A Possible Solution

This work proposes a new hybrid control structure. It employs two individual control systems, a GFL and a GFM, working in parallel and independently, that are merged to create the resulting output. To assess the novelty of the proposed control structure, a literature search for works that present parallel control loops was conducted.

One of the main applications of parallel control loops is for separately controlling positive- and negative-sequence components of current and voltage, which is relevant especially during grid faults. This technique can be applied to IBRs [33] and STATCOMs [34], and is usually based on decomposing the measured voltage and current into their positive- and negative-sequence components, using two independent, parallel control systems, and adding their output. In the end, the signals are transformed back to *abc* components in the output of the control system.

Another widespread application of parallel control loops is for harmonic suppression. It can be used for example to compensate for harmonics in synchronous machine drives [35], or to suppress harmonics caused by the PEC's switching effect [36]. As with the previously described application, this case performs a harmonic decomposition of the measured voltage and current. Each harmonic component of interest has its own control system, and their outputs are added in the end.

Other applications of parallel control loops were also found. Rodriguez-Amenedo et al. [37] describe the control of High-Voltage Direct Current (HVDC) transmission systems used to connect offshore wind power plants to the grid. In the analyzed case, two different HVDC transmission lines connect the onshore grid to the offshore substation. To properly split the load between the two transmission lines, a single control system has two parallel current loops, that split the reference current calculated from a common voltage loop. Guo [38] uses controlled harmonic current injection with distributed generation systems to identify islanding events. It employs a separate control loop to inject a 5^{th}-order harmonic current in the grid. When an islanding event happens, the equivalent grid impedance changes, and the harmonic injection control will also naturally change its output. This behavior is used together with classic frequency feedback detection methods to increase the assertiveness of the islanding-detection control.

Among the analyzed studies, the reference that most resembles the proposed control system is presented by Harnefors et al. [39]. It proposes a modification to a GFM control system in order to give it GFL characteristics. By appropriately choosing the gains of the control system, its behavior can be that of a GFM, GFL, or a hybrid between the two. The described experimental setup consists on two PECs on a back-to-back configuration. One of them has the proposed control system and is free to follow the chosen reference value of active power, while the other controls the dc-link voltage. It evaluates the hybrid controller behavior by performing a series of step changes in the reference active power, and showing that it behaves better than the usual GFL or GFM. The paper does not specifically discuss grid support and does not show how the converter would respond to grid transients. It is also unclear if the proposed control system would enable the converter to control the dc voltage of the back-to-back setup if required, which could limit its application.

None of the described works match the hybrid system proposed in this thesis, highlighting its originality.

1.2 Objectives

The previous section showed that there is great interest in the electric industry related to the converter control system. The number of grid-connected IBRs is increasing, and the issues related to reduced grid inertia and frequency support are becoming increasingly important. In this scope, developing a new converter control scheme that includes the main advantages of the two currently most used control topologies, the GFL and GFM, could prove very useful for a number of applications. Therefore, the core contribution of this study is:

To propose and develop the Hybrid Control Converter (HCC), a novel kind of converter control structure that can exploit the advantages of both the GFL and GFM at once.

Some correlate topics are explored, resulting also in the following contributions:

- to describe the main control structure of the GFL and the GFM, discussing their operational strategies and limitations, highlighting their differences and showing how these affect their dynamic behavior;
- to study the stability of the HCC, demonstrating it is at least as stable as conventional control systems for the analyzed cases;
- to study the robustness of the HCC, demonstrating that, even with usual simplifications in the mathematical model or mismatches between the actual

and expected values of system components (such as the filter impedance), it retains stability and operates as intended;

- to identify a possible application of the HCC with wind turbines, improving their frequency support capability without hindering its MPPT control; and
- to identify a possible applications of the HCC with HVDC systems, showing it can lead to an autonomous interconnection of different ac systems.

This thesis resulted in a journal article, entitled “Hybrid Control Scheme for VSC Presenting Both Grid-Forming and Grid-Following Capabilities”, published at IEEE Transactions on Power Delivery [40].

In summary, this work proposes the Hybrid Control Converter, that encompasses the GFL’s quick and accurate power control, and the GFM’s fast and inherent grid support capability. To do that, as detailed in Chapter 3, it employs two parallel control systems that merge together, instead of a single control system, which is the usual implementation.

1.3 Document Structure

This document is structured in eight chapters. In Chapter 1, the scenario that motivated the research is presented, with a discussion about current PEC control techniques and their limitations regarding grid support capability. The main goals of this study are also described.

In Chapter 2, a detailed description of the GFL and GFM control systems is presented. Their control loops and operation strategy are described, and simulations show the difference in their dynamic behavior when facing transient situations. The main advantages and drawbacks of each kind of converter control are discussed.

In Chapter 3, the HCC is described. The mathematical principle that enables it to show characteristics of both the GFL and GFM is demonstrated, and its control system is described in detail. Simulations prove that the developed analytical equations are valid, showing that it indeed presents the behavior of both the GFL and GFM. A simulation where the HCC performs black-start is also presented, highlighting this important capability.

In Chapter 4, the stability of the proposed control system is discussed. The system transfer functions are described, both for the HCC and conventional GFL/GFM converters. Different analyses are performed to attest to the stability of the proposed control system, confirming it is at least as stable as conventional converters for the analyzed cases.

In Chapter 5, the concept of robustness is presented and discussed. Some situations where the mathematical modeling could differ from reality, including parameters mismatch and the inclusion of previously neglected factors such as switching harmonics, are analyzed. Mathematical and simulation results show that the HCC does not become unstable when faced with these adverse scenarios, confirming its robustness.

In Chapter 6, an application of the HCC with wind turbines is presented. First, the operating principle of the WT's PEC converter is presented. Then, a small adjustment to the HCC control system (that was developed in Chapter 3) is described, to enable the proposed behavior during transient situations. Simulation results show that the HCC improves the WT's frequency support capability when compared to a traditional GFL, while maintaining MPPT operation and thus not hindering its power generation capacity.

In Chapter 7, an application of the HCC with HVDC systems is presented. First, a small description of HVDC systems is presented. Then, the operating principle of the new HCC-HVDC system is discussed, and a necessary adaptation to the control system is applied. Simulation results including a meshed HVDC network and different ac systems show that the HCC improves the overall frequency stability of the system.

Finally, in Chapter 8, the entire thesis is summarized. A list of topics for further research is also presented.

Chapter 2

Power Electronics Converters

This chapter presents the two main control strategies for Voltage Source Converters: the Grid-Following Converter and the Grid-Forming Converter. First, their basic control systems are described, highlighting differences and similarities. Then, their transient behaviors are compared by simulating changes in reference power and system load. The difference in how they react to these changes is explained and linked to their control scheme, exposing the main advantages and drawbacks of each one.

2.1 Basic Structure and Main Applications

Power electronics converters are a type of equipment increasingly present in the electrical grid [10]. Most applications employ them as coupling between an Alternating Current (ac) and a Direct Current (dc) system, controlling the voltages, currents and power exchange between them. As renewable generation grows, the number of converters connected to the grid increases, since both solar panels and wind turbines employ a converter as an interface to the grid. On the demand side, electronic devices and controlled motor drives employ converters, which indicates a high positive trend for the overall amount of converters connected to the grid.

A few examples of power converters' applications are shown in Figure 2.1. The schematic of a solar power plant is shown in Figure 2.1a, where groups of solar panels generate power in dc; they are connected to junction boxes that feed into a converter, which transforms the power to ac in order to deliver it to the electrical grid [41]. A permanent-magnet full-converter wind turbine generator is shown in Figure 2.1b, where two converters are used in back-to-back configuration [41]. The generator-side converter controls the amplitude and frequency of the current on the stator windings, therefore controlling its rotating speed and torque, and the grid-side converter delivers the generated power to the grid. A BESS connected to the grid via a converter is shown in Figure 2.1c. In this case, the converter adjusts its operating voltage according to a given reference value, controlling the battery charge or discharge during its operation [42]. Figure 2.1d shows an HVDC transmission system, where the generation from a given power plant (in this example, an offshore wind farm) is transmitted to the consumption center usually over very long distances, using a dc transmission line. The converter next to the power plant transforms its generated power to dc, and the one close to the consumption center transforms it back do ac, so it can be more easily distributed [43]. Many other applications exist, such as DFIG WTs, STATCOMs, back-to-back connections between asynchronous systems and other kinds of storage devices.

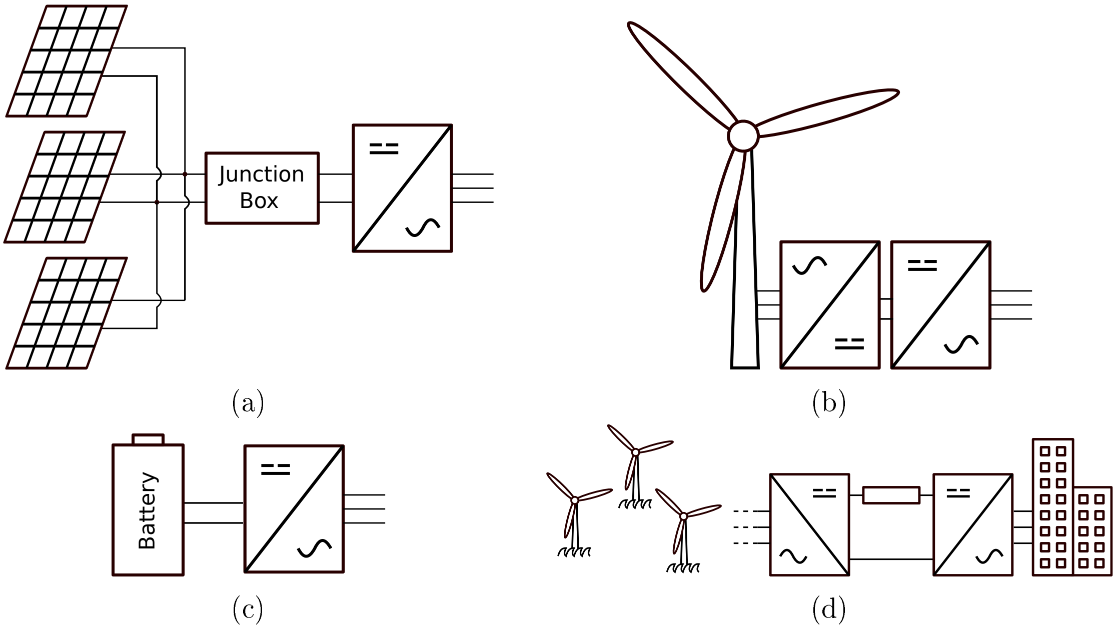

(a) (b)

(c) (d)

Figure 2.1: Examples of power converter applications: (a) solar plants, (b) full-converter wind turbines, (c) BESSs and (d) HVDC transmission systems.

The kind of converter analyzed in this thesis is the three-phase Voltage Source Converter (VSC) [41]. It is comprised of fast-switching semiconductor devices, such as IGBTs or IGCTs, and can be controlled to transfer power from the dc side to the ac side, in what is called inverter operation, or from the ac side to the dc side, in rectifier operation. A schematic of a general 2-level converter [44] is shown in Figure 2.2.

The converter itself is usually connected to the ac grid using a filter, to attenuate harmonic components in the output voltage and current caused by the switching process. There are various filter topologies available that behave differently in terms of harmonic filtering. The most common ones are the RL and the LCL filters, as shown in Figure 2.3.

Measurements of the ac voltage and current (and other optional signals, such as dc voltage) are input into the control system. Based on specific reference values to follow, the control system calculates the reference output voltage. Then, a switching

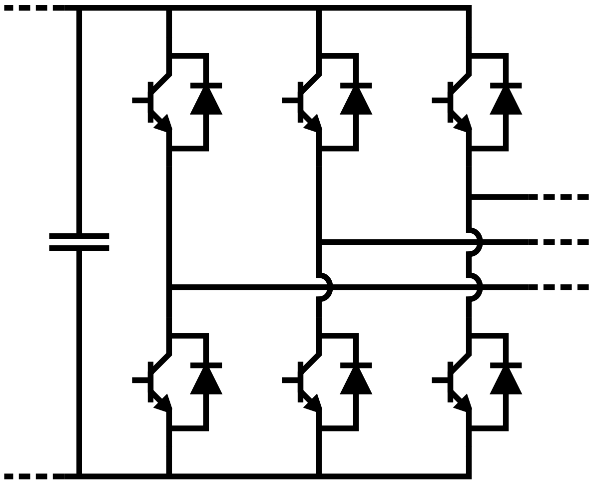

Figure 2.2: Schematic diagram of a 2-level converter.

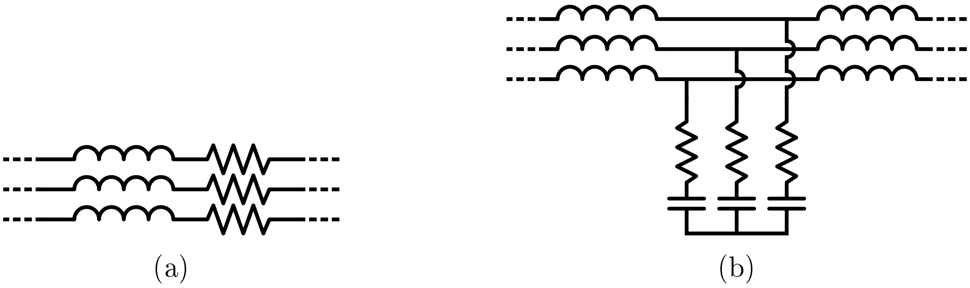

(a)

(b)

Figure 2.3: Different filter topologies that can be employed with converters: (a) RL filter and (b) LCL filter.

algorithm sends the appropriate switching signals to each of the converter's switches so that the reference output voltage appears at the converter ac terminals. The switching effect is discussed in more detail in Chapter 5.

Furthermore, the converter itself can be implemented with different topologies, granting it different output harmonic characteristics and operational behavior. Aside from the 2-level converter shown in Figure 2.2, other examples of converter topology [45, 46] are shown in Figure 2.4.

A general representation of a VSC system is shown in Figure 2.5, where $\boldsymbol{v}^*_{out}$ and $\boldsymbol{v}_{out}$ are the converter reference and actual output voltage, $\boldsymbol{v}_{pcc}$ is the voltage at the Point of Common Coupling (PCC) and $\boldsymbol{i}_{conv}$ is the converter's output current. Variables in bold denote the vector representation of signals, usually three-phase signals in the time domain, such as: $\boldsymbol{v}(t) = [v_a(t), v_b(t), v_c(t)]^T$. The figure also shows, in general, that the control system can receive different reference signals.

This thesis focuses on the design of the converter's control system. Based on its overall implementation and on its main targets, the converter can be classified into two categories: Grid-Following Converter (GFL) and Grid-Forming Converter (GFM) [15].

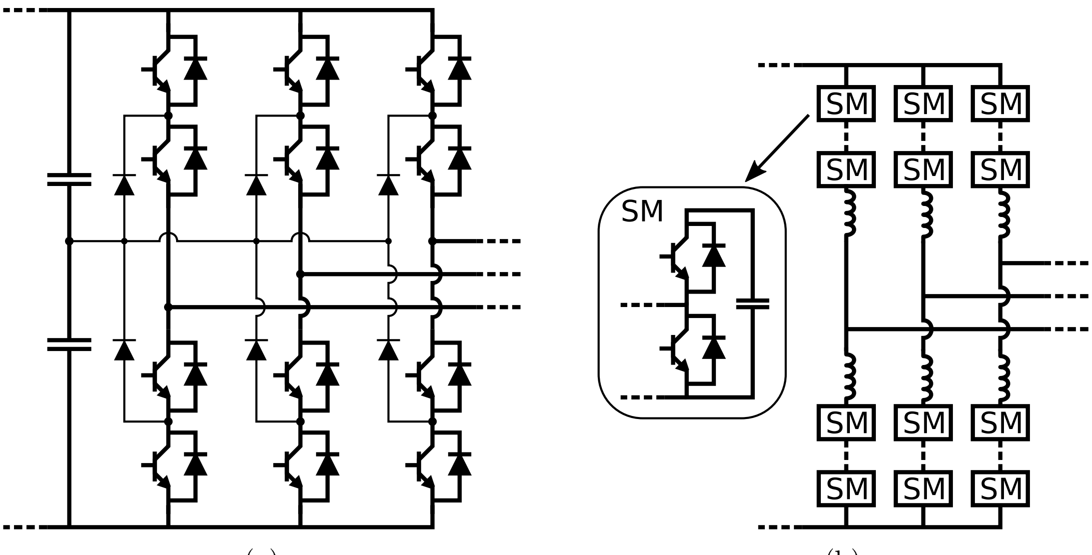

(a) (b)

Figure 2.4: Other examples of converter topology: (a) three-level, or Neutral-Point Clamped converter (NPC), (b) Modular Multilevel Converter (MMC).

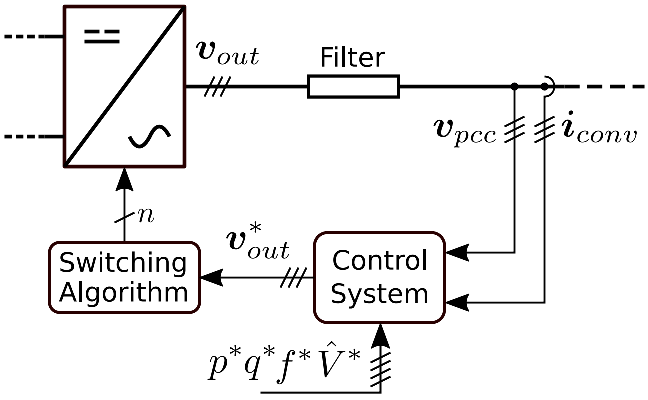

Figure 2.5: Schematic of a general VSC system.

2.2 Grid-Following Converter (GFL)

The Grid-Following Converter, also known as Grid Follower, is the most predominant kind of converter nowadays. Its control system is aimed at quickly and accurately following given references of active and reactive power, and the rationale behind this behavior can be easily understood. For instance, if the converter is connecting a BESS to the grid, the amount of power it delivers or consumes from the grid dictates the battery charge or discharge, and it is vital to accurately control that behavior to keep the BESS under safety limits of charge current and SoC [9]. The converter connected to a solar panel or wind turbine works to keep it operating at the optimal power point using an MPPT algorithm; to do that, it must accurately control the power delivered to the grid to ensure maximum possible generation for a given solar or wind condition [47]. Since usually the converter controls the delivered power by controlling its output current, the usual behavior of the GFL can then be approximated to that of a controlled current source in parallel with a large impedance [15].

This type of control relies on a pre-existing electrical grid. Even if a transient situation leads to variations of grid voltage and frequency, the GFL does not change its reference signals of active and reactive power, since they are not directly dependent on the grid voltage. As a consequence, the GFL does not inherently support the grid during faults and transients. Specific (optional) control schemes must be applied to make grid supporting capabilities available to the GFL [15]. One of the possibilities is to implement droops [48], which modify the converters' references of active and reactive power, depending on the grid frequency and voltage amplitude. This way, the converter can help during frequency and voltage transients, even though it is ultimately controlling its active and reactive power. Nevertheless, it loses the ability to accurately track its original references of active and reactive power.

There are various ways to implement the GFL control system. This thesis employs the Synchronous Reference Frame control for VSCs, based on the Park Transform [49]. Also known as *dq*-control, this is one of the most common ways to implement the VSC control system. Other implementations are presented at the end of this section.

2.2.1 GFL Based on Synchronous Reference Frame Control (*dq*-control)

The *dq*-control method is based on transforming 3-phase sinusoidal ac variables (*abc*) into dc components (*dq0*) using the Park Transform [49] and its inverse. They are defined, respectively, as:

$$\begin{bmatrix} x_d(t) \\ x_q(t) \\ x_0(t) \end{bmatrix} = \frac{2}{3} \begin{bmatrix} \cos(\theta) & \cos(\theta - \frac{2\pi}{3}) & \cos(\theta + \frac{2\pi}{3}) \\ -\sin(\theta) & -\sin(\theta - \frac{2\pi}{3}) & -\sin(\theta + \frac{2\pi}{3}) \\ \frac{1}{2} & \frac{1}{2} & \frac{1}{2} \end{bmatrix} \begin{bmatrix} x_a(t) \\ x_b(t) \\ x_c(t) \end{bmatrix}, \tag{2.1}$$

and

$$\begin{bmatrix} x_a(t) \\ x_b(t) \\ x_c(t) \end{bmatrix} = \begin{bmatrix} \cos(\theta) & -\sin(\theta) & 1 \\ \cos(\theta - \frac{2\pi}{3}) & -\sin(\theta - \frac{2\pi}{3}) & 1 \\ \cos(\theta + \frac{2\pi}{3}) & -\sin(\theta + \frac{2\pi}{3}) & 1 \end{bmatrix} \begin{bmatrix} x_d(t) \\ x_q(t) \\ x_0(t) \end{bmatrix}, \tag{2.2}$$

where x represents a generic ac variable in the time domain, usually a current or voltage, and $\theta = \omega t$ is its phase angle.

Unlike the *abc* components which are ac values, the *dq0* components are constant in steady-state (considering balanced, sinusoidal *abc* components). For a 3-phase circuit, the instantaneous real and imaginary power (p, q) [50] can be calculated from the dq-components of the current and voltage. For the general converter system shown in 2.5, these values, at the PCC, are calculated respectively as:

$$p(t) = \frac{3}{2}\left[v_{pcc,d}(t)i_{conv,d}(t) + v_{pcc,q}(t)i_{conv,q}(t)\right], \tag{2.3}$$

$$q(t) = \frac{3}{2}\left[v_{pcc,q}(t)i_{conv,d}(t) - v_{pcc,d}(t)i_{conv,q}(t)\right]. \tag{2.4}$$

The phase angle used in the transformation must be calculated from the measurements of current and/or voltage, since it cannot be directly measured. For that purpose the control system usually employs a PLL, an algorithm designed specifically to estimate the frequency and phase angle of sinusoidal signals. There are many ways to implement a PLL [51], but in general they take the ac measurements as inputs and give frequency and/or phase as outputs. A simple way to implement the PLL is shown in Figure 2.6, where the q-component of the measured voltage is delivered to a Proportional-Integral (PI) controller, which acts to keep it at a reference value, chosen equal to zero. The output of this PI controller is the estimated grid frequency ω, which is then integrated to result in the estimated value of the phase angle θ. If the q-component deviates from zero, it indicates that the frequency of the voltage signal changed and the dq-frame suffered a rotation; the PI controller reacts accordingly, updating the estimation of grid frequency.

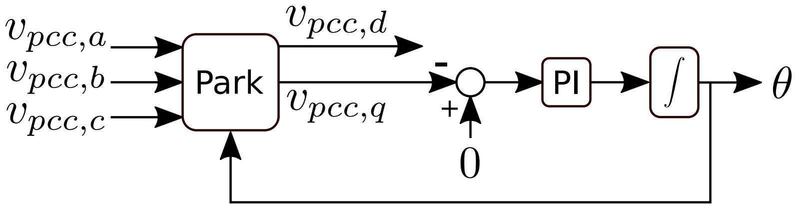

Figure 2.6: Schematic of a Phase-Locked Loop.

A PI controller is represented in the frequency domain with the following transfer function:

$$PI(s) = k_p\left(1 + \frac{1}{sT_i}\right), \tag{2.5}$$

where k_p is the proportional gain and T_i is the integral time constant.

As mentioned before, the GFL control system is designed to follow reference values of power. The *current control loop* is implemented as shown in Figure 2.7 [15, 52]. Usually, the reference values of active and reactive power (p^*, q^*) are used to calculate the reference currents $(i^*_{conv,d}, i^*_{conv,q})$ using (2.3) and (2.4). Since the PLL is usually tuned to orient the dq-axes in such a way that $v_{pcc,q} = 0$, those calculations can be further simplified. Then, the error between the reference current and the actual measured current $(i_{conv,d}, i_{conv,q})$ goes through a PI controller, that generates the reference values of output voltage ($v^*_{out,d}$, $v^*_{out,q}$) that should appear at the converter's ac terminals. Finally, these are transformed back to *abc* components using (2.2). Other functionalities may be added to the control system, such as saturation units to protect against overcurrent during fault conditions. It can be noted that for some applications, such as electrical machine drives, the reference values of current may be calculated differently.

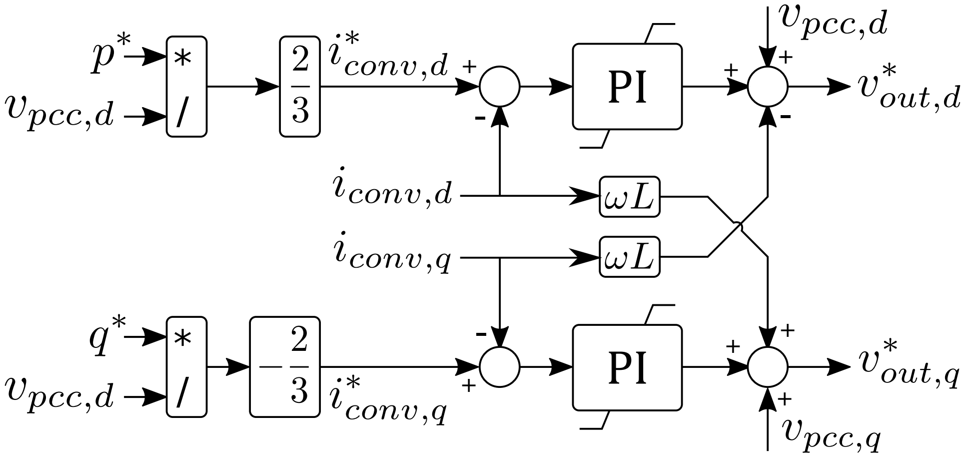

Figure 2.7: Current control loop for the GFL.

As mentioned before, the reference output voltage then goes through a switching algorithm that controls the semiconductor switches in a specific way, so that the converter output voltage matches the reference value. These algorithms change the switches state multiple times per second, turning them on or off, as described by a switching function $S(t)$. This way, the control loop is complete. The measurements of voltage and current tell the controller about the ongoing state of the system; the controller calculates what should be the output voltage of the converter to achieve its targets of active and reactive power; and the switching algorithm controls which switches should be activated so that the desired output voltage appears at the converter terminals.

It is possible to give the GFL grid-supporting capabilities. Due to the natural coupling in most electrical grids between active power and frequency, and reactive power and voltage [48], the converters' active and reactive power references can be modified to p^*_{drp} and q^*_{drp}, depending on the grid voltage and frequency. If the grid frequency decreases, the active power reference is increased, and vice-versa. If the grid voltage decreases, the reactive power reference is increased, and vice-versa. This way, the converter can help during frequency and voltage transients, even though it is ultimately controlling its active and reactive power. These algorithms are called droops [48], and are shown in Figure 2.8.

The error between the reference and measured frequency (f^*, f) is multiplied by a constant gain, $k_{drp,p}$, and added to the original value of reference active power.

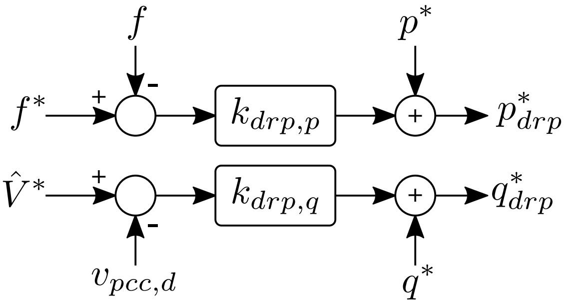

Figure 2.8: Droop control for the GFL, enabling grid support capability.

The same happens with the error between reference and measured voltage amplitude ($\hat{V}^*, v_d$) and the original value of reference reactive power, with a gain $k_{drp,q}$. Including the droops, the overall control system for the GFL using dq-control is as shown in Figure 2.9. This control system schematic is independent from the converter topology. The switching algorithm is the only control block that is adjusted to the specific converter topology, resulting in a different number or output signals depending on the number (n) of semiconductor switches in the converter (e.g. $n = 6$ for the 2-level converter, $n = 12$ for the NPC, $n = 2 \cdot n_{sm}$ for the half-bridge MMC, where n_{sm} is its number of submodules...).

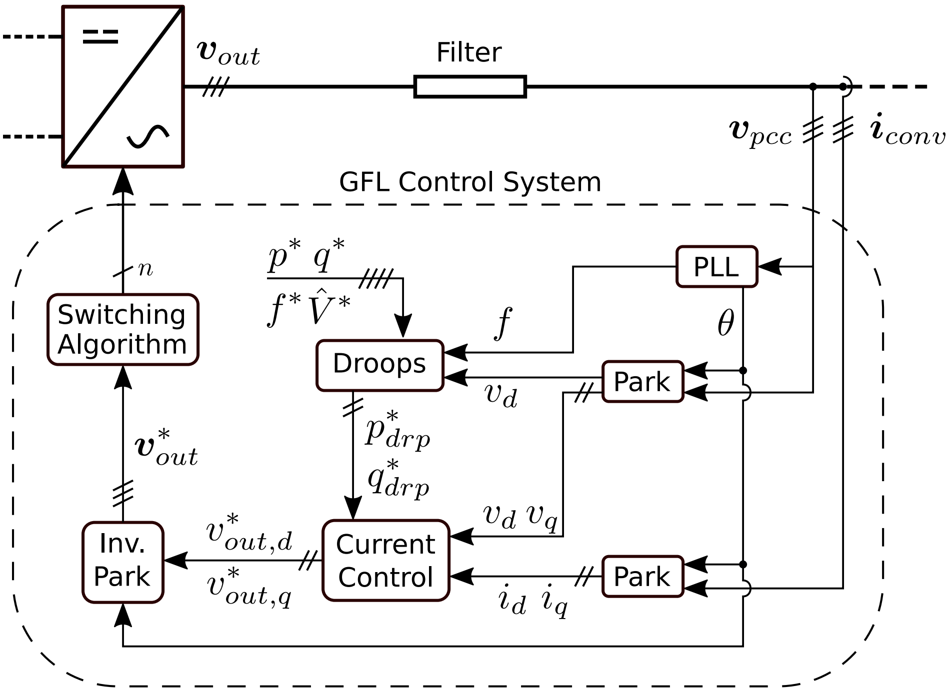

Figure 2.9: Overall control system for the GFL, including droops.

One of the main drawbacks of the GFL is its lack of black-start capability, which means it cannot restart the grid by itself after a blackout. The control system does not work if the grid voltage is zero, since the PLL needs the voltage measurement to calculate the grid frequency and achieve synchronization. This also leads to limited applicability to islanded systems, where some other voltage and frequency source must be present, forming the grid. Moreover, even though it can provide some kind of grid support, it still relies on a pre-existing and somewhat stable grid, since it needs the measurements of voltage and frequency to work properly. The need of a PLL may also reduce the converter's small-signal stability [53], even interacting with the synchronization units of other converters working in the same grid [54]. The GFL is specially sensitive to weak grids with low short-circuit ratio, where the grid voltage may be heavily influenced by the converter's own output current [16].

2.2.2 Other Implementations of the GFL Control System

Other ways to implement the control system exist. For example, Proportional-Resonant (PR) controllers can be used instead of PI controllers. In this case, there is no need for a PLL, but at the cost of difficult implementation of current limitation control loops in case of grid faults. Extra control loops may be present to achieve various objectives, such as controlling a specific harmonic [35] or negative-sequence components of the output current [33].

Besides that, the reference values of power may come from different control algorithms. These include MPPTs to maximize solar or wind power generation, a SoC algorithm to control a BESS's stored energy, or even an extra controller to provide frequency support during a grid transient [14, 55].

In the end, all variations of the GFL control the output current, synchronized with the existing grid, in order to achieve various goals.

2.3 Grid-Forming Converter (GFM)

The GFM was developed with the goal of enhancing power system stability [16], especially for weak grids with high penetration of inverter-based generation (usually renewable energy sources such as wind and solar). Unlike the GFL, the main references the GFM follows are voltage amplitude and frequency. It tries to keep the voltage and frequency at the PCC as close as possible to the desired reference values, and therefore it works in a different way than the GFL. The usual behavior of the GFM can be approximated to that of a voltage source in series with a small impedance [15].

One of the main advantages of the GFM is that it has black-start capability [10, 16] as, in a way, it creates the system voltage magnitude and frequency, serving as a reference for other converter units operating nearby. It also has faster, inherent grid support capabilities, since anytime the grid voltage or frequency deviate, it automatically acts to keep them at the reference values [16].

2.3.1 GFM Based on Synchronous Reference Frame Control (*dq*-control)

One of the possibilities of implementing the GFM control system is to use *dq*-control. Similarly to the GFL, measurements of current and voltage are transformed from *abc*- to *dq*-components using the Park Transform and then provided to the control system. One of the main differences is that the GFM does not have a PLL block to measure the grid frequency because it has its own frequency reference to follow (although a synchronization algorithm could employ a PLL during the startup of the GFM in specific cases).

The GFM with *dq*-control usually contains two control loops: the voltage loop and the current loop, as shown in Figure 2.10. Since its references are of voltage amplitude and frequency, it needs an extra part in the control system, called the *voltage control loop*. It generates the current reference values from the reference voltage and frequency and provides them to the internal current control loop. Extra control blocks, such as saturation units to protect against overcurrent, could also be present in the control system.

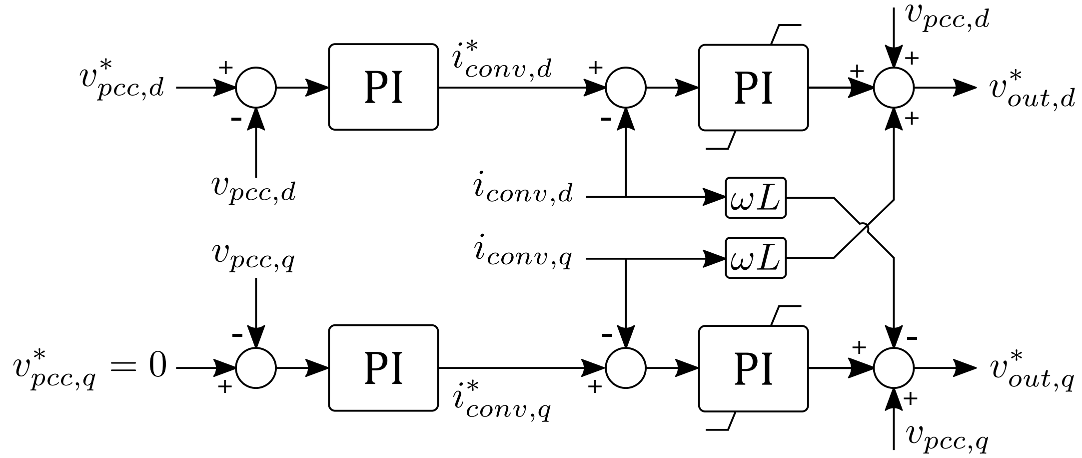

Figure 2.10: Voltage and current control loops for the GFM.

The frequency reference generates the phase angle that is applied directly in the Park transforms present in the control system. Similarly to the GFL, it is common to define that the *q*-component of the voltage (in this case, the reference voltage) as zero, following the alignment of the rotating frame axes of the Park transform. Therefore, the reference voltages in the synchronous reference frame are defined as:

$$v_d^*(t) = \hat{V}^*, \tag{2.6}$$

$$v_q^*(t) = 0. \tag{2.7}$$

The GFM control system measures the voltage and current at the PCC; based on the difference between the reference voltage and the actual measured voltage, it calculates (in the voltage control loop) what current should the converter provide to the grid. Then, based on the difference between that and the measured current, the current control loop calculates what should be the voltage at the converter terminals that results in that current flowing to the grid. Similarly to the GFL, these reference output voltage values are provided to a switching algorithm that controls the switches, so that the desired voltage appears at the converter terminals.

The described control system works well when the GFM is the only source in the grid controlling the voltage at the PCC, but may fail if there are other voltage sources. The presence of multiple voltage sources, each with stiff voltage amplitude and frequency references, leads to instability. Each one individually tries to change the voltage at the PCC, but ultimately they are all trying to set the grid voltage to possibly different values at the same time. To overcome this problem, droops are usually added to the control system [15], as shown in Figure 2.11, so that the voltage and frequency references may vary, becoming f^*_{drp} and $\hat{V}^*_{drp}$, according to the active and reactive power delivered to the grid. If the active power supplied by the converter increases, its reference frequency decreases proportionally to the gain $k_{drp,f}$; if the reactive power increases, its voltage amplitude reference decreases according to the gain $k_{drp,V}$. This way, multiple voltage sources can work in parallel in the same electrical grid since their individual references automatically adjust to reach a point of equilibrium.

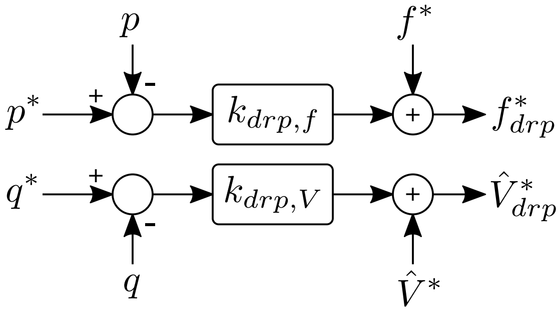

Figure 2.11: Droop control for the GFM, used to avoid instability when working in a grid with other voltage sources.

Including the droops, the overall control system for the GFM using dq-control is as shown in Figure 2.12.

One of the main drawbacks of the GFM is that its active and reactive power are not controlled as closely as the GFL, since changes in grid voltage and frequency lead to automatic variations of delivered power.

2.3.2 Other Implementations of the GFM Control System

The described dq-control takes references of voltage amplitude and frequency and applies these values into the PI controllers to calculate the reference output voltage.

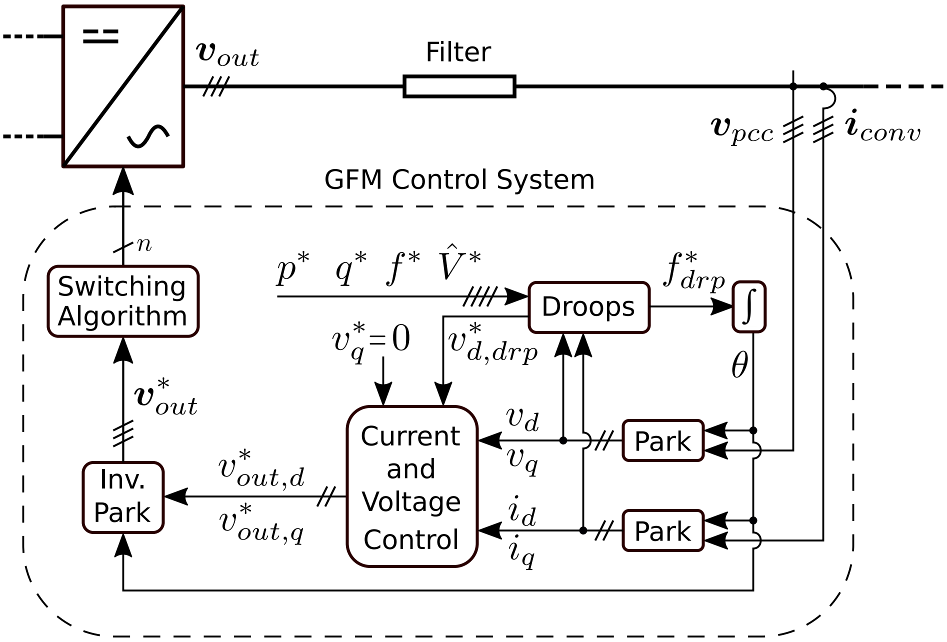

Figure 2.12: Overall control system for the GFM, including droops.

There are many possible variations of this control scheme. For example, the modified voltage references could be applied directly as v^*_{out}, or a single PI controller could be employed instead of two. A PR controller could also be employed instead of the PI.

As for the reference values of voltage amplitude and frequency, there are other possibilities besides the droops. The Power-Synchronization Control [56] emulates the synchronization behavior of a synchronous machine, employing a control structure similar to the droops but with an integral action on the power loop.

Another technique that aims at emulating the behavior of a synchronous machine may change in nomenclature among different studies, but is usually called Virtual Synchronous Machine (VSM) or Synchronverter [25, 57]. It emulates the synchronous machine inertial behavior by implementing the swing equation [58] into the calculation of the reference frequency, applying virtual terms of inertia and damping into the GFM control.

The Matching Control [59] technique draws a parallel between converters and synchronous machines. In this case, a power imbalance leads to changes in a converter's dc voltage, while for a synchronous machine it would lead to changes in frequency. This analogy is implemented to derive the converter frequency values from the dc voltage measurements.

These are a few examples showing that the GFM can have different control system implementations and characteristics. Nevertheless, being classified as a GFM, the control system ultimately controls the PCC voltage according to given reference values of voltage amplitude and frequency.

2.4 Transient Behavior Comparison

The previous section showed that both the GFL and GFM can have multiple references and thus control active power, reactive power, voltage amplitude and frequency, if the droop control loops are taken into account. It may appear that both types of converters are interchangeable, but their transient behavior turns out to be very different because of their distinct control system implementations.

To illustrate and discuss the inherent behavioral differences between these control schemes, different scenarios are simulated. The GFL without droop (called *base GFL* from now on), the GFL with droop (called *GFL+droop*) and the GFM with droop are compared against each other, while the GFM without droop is not included in the analysis. This is due to the fact that, as mentioned previously, it is not actually practical to have a working GFM without the droop control (or other similar strategy) in most applications, except if operating as a single Uninterruptible Power Supply (UPS). Therefore, for the remainder of this analysis, the GFM with droop is simply called GFM. The GFL without droop is the usual type of converter control used with wind and solar generation, while the GFL+droop and the GFM usually require some kind of energy storage device, such as a BESS. All converters employ *dq*-control, as described in the previous sections, and are modelled as controlled voltage sources in the simulations.

The simulation consists on a basic electrical system. A controlled voltage source ($\boldsymbol{v}_{grid}$) with a coupling impedance (R_{grid}, L_{grid}) represents the equivalent grid voltage, and is implemented similarly to a VSM, with a swing equation, droop mechanism ($k_{drp,p,grid}$) and inertia constant (H_{grid}) to mimic the real behavior of an electrical grid. Therefore, if its active power increases (considering a reference value of zero), its frequency decreases according to its moment of inertia, reaching a different steady-state with a frequency lower than the nominal value according to its droop. The chosen inertia constant is low to better visualize the different behavior of the analyzed converters when facing grid transients. Besides that, as it has an active power droop, this representation of the grid increases its output power when the system frequency deviates from the nominal value (just as a regular grid, containing frequency support generation units, would). The droop that changes the reference voltage amplitude according to the reactive power is neglected for this analysis. A transmission line, represented as a series connection of a resistance and an inductance (R_{TL}, L_{TL}), connects the grid voltage source to the PCC. The load is comprised of a resistance ($R_{load,1}$) connected to the PCC and a circuit breaker, that is used to change the total load during the simulation by including a second resistance ($R_{load,2}$) to the PCC. The resistance value is calculated to achieve specific values of active power on nominal grid conditions and during the simulated load step

($P_{load,1}$, $P_{load,2}$). The converter is connected to the PCC through a filter comprised of a resistance in series with an inductance (R_f, L_f) for simplicity. The switching process is neglected in this analysis, therefore the reference output voltage calculated by the converter's control system appears directly at its terminals. The main parameters of the test system are shown in Table 2.1, and a schematic is shown in Figure 2.13. Most electrical parameters are chosen as typical values of 5.0% p.u. and a 10% X/R ratio, representing a generic system instead of a specific application.

Table 2.1: Parameters of the simulated generic electrical system.

Parameter	Symbol	Value	
Nominal Values	S_{nom}	10.0 MVA	-
	V_{nom}	34.5 kV	-
	f_{nom}	60 Hz	-
Load Power	$P_{load,1}$	5.0 MW	0.5 p.u.
	$P_{load,2}$	5.0 MW	0.5 p.u.
Grid Inertia Constant	H_{grid}	0.1 s	-
Grid Internal Impedance	R_{grid}	595.1 $m\Omega$	0.005 p.u.
	L_{grid}	15.8 mH	0.05 p.u.
Transmission Line	R_{TL}	595.1 $m\Omega$	0.005 p.u.
	L_{TL}	15.8 mH	0.05 p.u.
Converter Filter	R_f	595.1 $m\Omega$	0.005 p.u.
	L_f	15.8 mH	0.05 p.u.

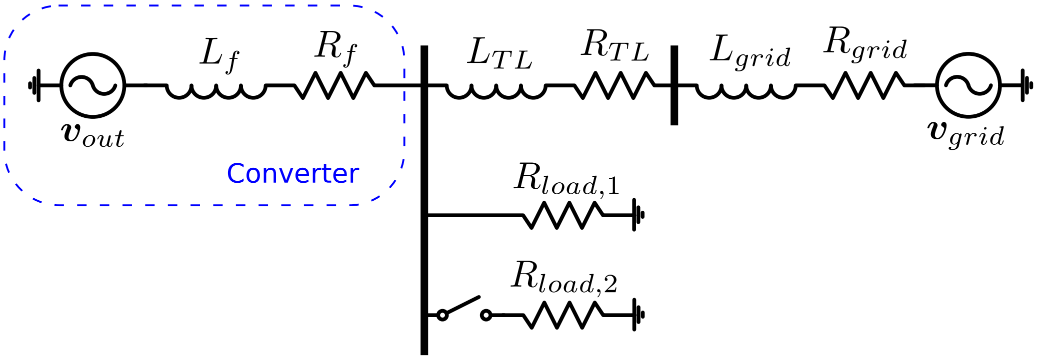

Figure 2.13: Schematic of the simulated generic electrical system.

The control system parameters are shown in Table 2.2. The current loop gains are the same both for the GFL and GFM. The voltage loop gains are only present in the GFM, since the GFL does not have this control loop. The gains for the current loop were calculated according to the Technical Optimum technique [60], while the gains for the voltage loop and droops were chosen empirically. The value of the overall converter delay T_Σ, described in more detail in Chapter 4, is adapted from Carvalho [61]. The timestep of the electrical transient simulation and the sampling frequency of the implemented control system are also described in the table.

Table 2.2: Control system parameters of the simulated generic electrical system.

Parameter	Symbol	Value
Current Loop	$k_{p,i}$	26.3 V/A
	$T_{i,i}$	26.50 ms
Voltage Loop	$k_{p,v}$	52.6 mA/V
	$T_{i,v}$	100 ms
GFL Active Power Droop	$k_{drp,p}$	2.0 MW/Hz
GFM Frequency Droop	$k_{drp,f}$	0.5 Hz/MW
Grid Active Power Droop	$k_{drp,p,grid}$	5.0 MW/Hz
Converter Delay	T_Σ	0.3 ms
Simulation Timestep	Δt_{sim}	0.1 μs
Control System Sampling Frequency	f_{sample}	10.0 kHz

The following simulations are performed separately for each of the three converter control strategies, but the results show the three response curves in the same figure, to make the comparison easier.

When the simulation is initialized, the converter chosen for that scenario has a zero reference active power. The power to supply the load comes from the grid, and as it has an inertia constant and droop mechanism, the system achieves a steady-state frequency of around 59.0 Hz, which is lower than the nominal value. At simulation time $t = 1$ s, the reference active power of the converter takes a step from zero to $P_{ref} = P_{load} = 5.0$ MW. As the converter is now fully supplying the load, the power coming from the grid is reduced to almost zero (there are still minor losses in the system), and therefore the frequency goes back to the nominal value of 60 Hz. Figure 2.14a shows the transient response of the active power supplied by the converter following the step change in reference, and Figure 2.14b shows the grid frequency.

It can be seen that, for the GFL, the active power was zero and goes to the reference value, as expected. For the GFL+droop, the initial value is different specifically because of the droop, that modifies the initial active power reference because the system frequency is below the nominal value of 60 Hz. For the GFM, the initial value is also different than zero because it tries to keep the grid frequency at the nominal value, which leads to variations of the delivered active power even

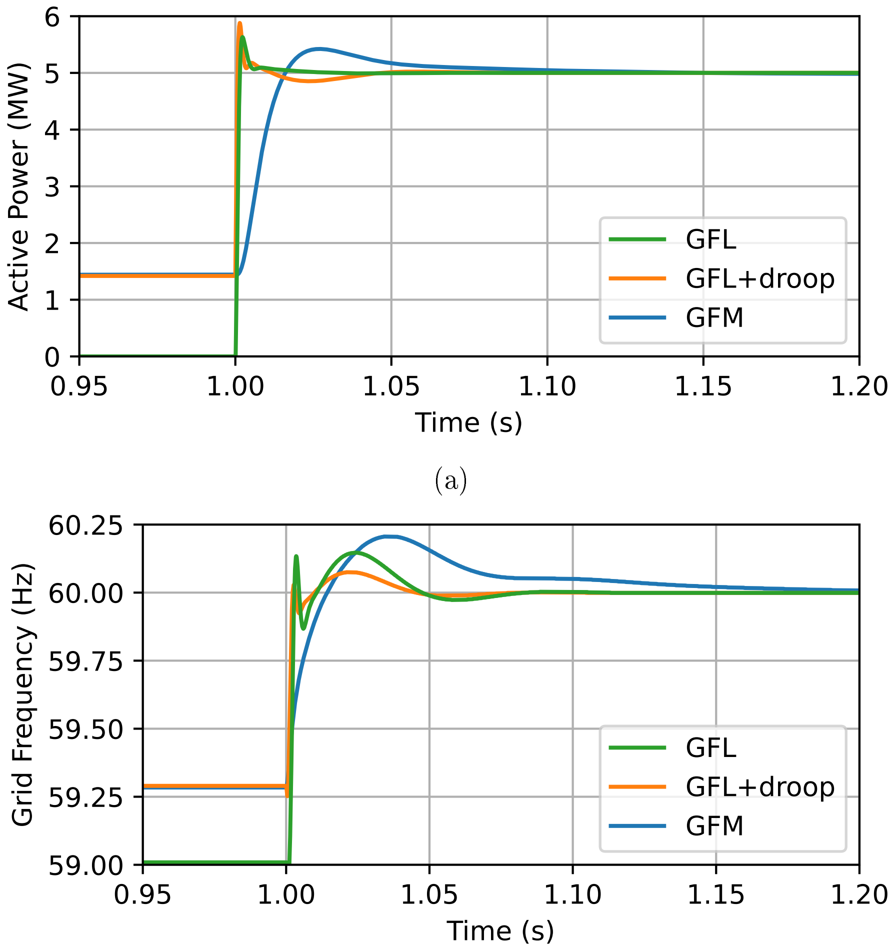

(a)

(b)

Figure 2.14: Simulation results for the GFL, GFL+droop and GFM, considering a step change in the converter's active power reference: (a) converter active power and (b) grid frequency.

though its reference is zero. They all reach the new reference of active power in the end.

Figure 2.14a shows that the GFL has a much faster response than the GFM for the step reference change. This is due to the fact that its target, the reference active power, is being controlled by a single current control loop. For the GFM, the reference active power signal goes through the voltage control loop and the current control loop, leading to a larger total delay.

The second test is a step load change. At simulation time $t = 1.5$ s, the equivalent load resistance is halved using a circuit breaker, which represents an increase of 5.0 MW (or 0.5 p.u.) in load power. This leads to a decrease in system frequency since the grid initially supplies most of the extra load power, thus reducing its own frequency setpoint. Nevertheless, the GFL+droop and the GFM also show an increase in output power because they have grid support capability. Figure 2.15 shows the converters' active power, the grid frequency and the RoCoF.

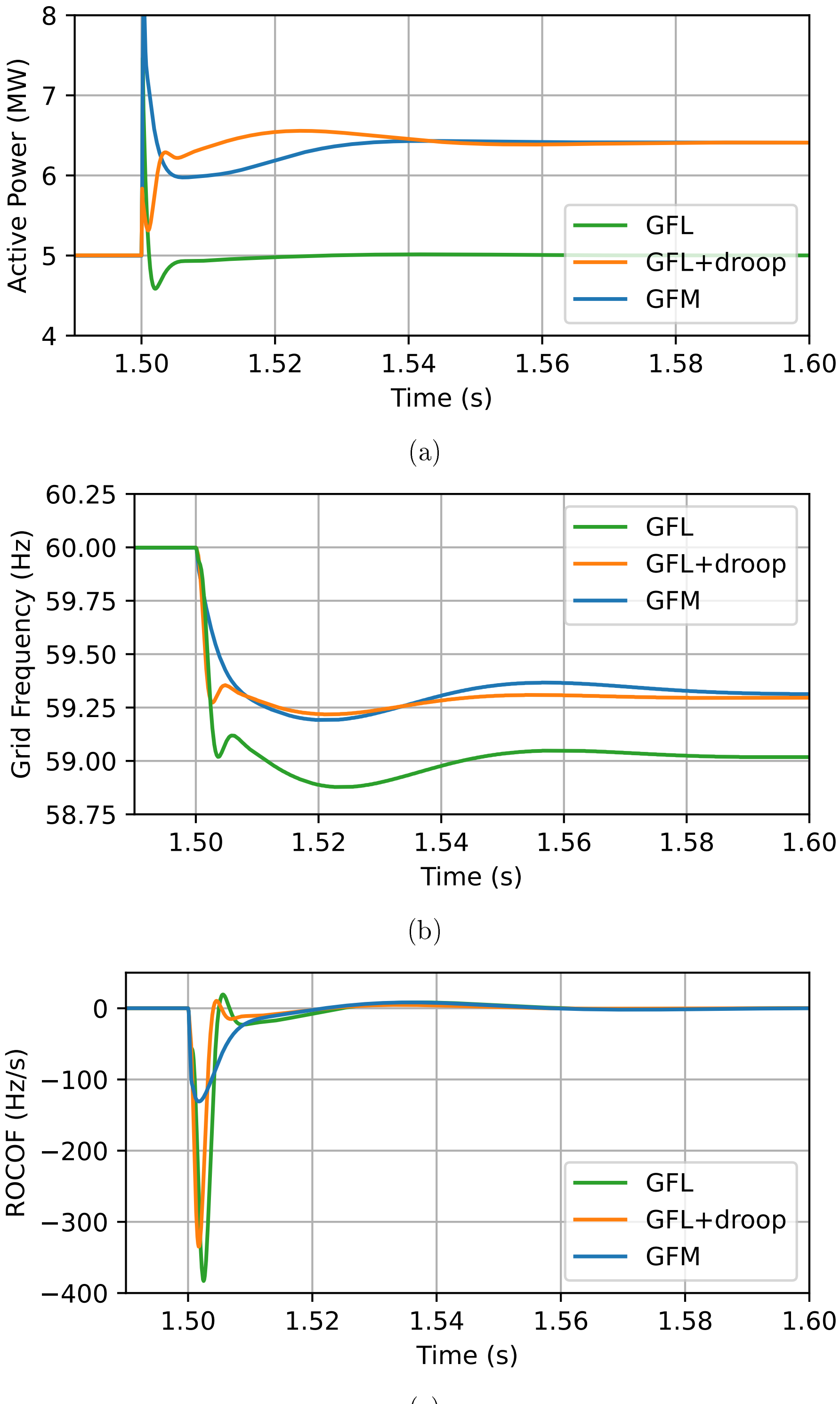

(a)

(b)

(c)

Figure 2.15: Simulation results for the GFL, GFL+droop and GFM, considering a step change in the load power: (a) converter active power, (b) grid frequency and (c) RoCoF.

As expected, after a small transient, the base GFL's power is unchanged, as there is no change to its reference power. Both the GFL+droop and the GFM increase their output power, but their behavior is quite different. The GFL's PLL detects a frequency change using the measured grid voltage; this leads to an increase in the reference power, and then the converter increases its output current to follow that new reference. As a result, the power delivered to the grid steadily increases after an initial delay. The GFM, on the other hand, is working to maintain the voltage in the PCC on its reference amplitude and frequency values. The voltage references are generated internally, from the amplitude and frequency references, so the voltage that appears at the converter terminals is, to some extent, stable. When the extra load is connected, the load current suddenly increases and the PCC voltage suddenly decreases. This leads to an increased voltage difference on the converter filter inductance, as the converter terminal voltage amplitude and frequency is initially kept unchanged. Thus, the power delivered from the converter has a sudden and almost immediate increase, as opposed to what is shown by the GFL.

This behavior from the GFM is beneficial from the point of view of the grid. Since there is some support on the first moments when the load increase occurred, the RoCoF reaches a value of only around -130 Hz/s, as opposed to the cases with the GFL and GFL+droop, when it gets to -380 and -330 Hz/s respectively, as shown in Figure 2.15c. The frequency nadir, the minimum value during the transient, is not as low as with the base GFL, but it is similar to the case with GFL+droop, as shown in Figure 2.15b. In this case, direct comparisons between the GFM and the GFL+droop must be taken with care, because the GFM also has the inherent effect of keeping the PCC voltage amplitude closer to the nominal value. Since the loads are simple resistors, this leads to an overall slightly higher load current and power, as opposed to the case with the GFL+droop where the PCC voltage suffers a slight drop, and along with it, the load power decreases. Since both the GFL+droop and GFM have a similar frequency nadir but the GFM actually supports a slightly higher load power during the transient, the edge goes to the GFM in the frequency nadir analysis. The RoCoF and frequency nadir may trigger grid protection schemes that could disconnect specific areas in case of severe oscillations, so avoiding a low nadir dip and a large negative RoCoF is very important. The worst simulated case is of course with the base GFL, which does not provide any support to the grid.

Since the GFM has this natural, automatic response to grid variations, it provides better grid support than a GFL+droop, which is becoming an increasing concern for systems with ever lower levels of inertia. Nevertheless, th GFM's output power deviates from the reference value when it provides grid support. This deviation is detrimental to some applications such as RESs and BESSs.

2.5 Partial Conclusion

This chapter presented and discussed the fundamentals of the two kinds of VSC control currently in use for different applications: the GFL and the GFM. Their base control systems were described, and simulation results demonstrated differences in their transient behavior.

The GFL has a faster, more accurate active and reactive power control. When the reference power changes, there is one single control loop involved, which results in a very fast response. Droops may be included in the control system to add frequency and voltage support capability to the GFL, at the expense of not controlling the active and reactive power exactly to the original reference values anymore. The GFM has a slower active and reactive power control because its main control targets are voltage amplitude and frequency. When the reference power value changes for the GFM, this signal goes through the voltage and the current control loops, leading to more delay in the control system and a slower overall response. The GFM also inherently changes its output power with variations of grid frequency and amplitude, meaning it may deviate from its reference power during regular operation, similarly to the GFL with droop.

As for grid support during transients, the GFM performs better than the GFL. The difference comes mainly from the basic structure of their control system: The GFL relies on its measurements of frequency (using a PLL) and voltage to detect any changes in the grid and only then act accordingly, which adds some delay to the converter response. This also means that the converter active or reactive power gradually rises from its previous value, following the integral action of the current controller. The GFM control works so that it maintains the voltage in the converter terminals; when a sudden change in grid voltage or frequency happens, the converter power immediately rises due to the voltage difference in the converter filter impedance, and then the droop control loop adjusts the internal references to reach a new steady state operating point. This means that, in the first moments of the fault, the GFM provides a faster and better grid support, which is especially important since a large initial RoCoF or a very low frequency nadir may trigger load shedding protection schemes that disconnect entire subsystems from the grid.

The base GFL is currently used in many applications that require accurate power control, such as solar panels, wind turbines, batteries, or dc transmission. The GFM is more suited to applications where voltage sources are necessary, such as uninterruptible power supplies or for islanded systems that require black-start capability.

Chapter 3

Hybrid Control Converter

In this chapter, a novel hybrid control system is proposed. First, the motivation behind the search for this kind of functionality is explained. Then, all mathematical equations that confirm the theory behind this idea are developed, showing its feasibility. The proposed hybrid control system is explained, and simulations are presented to illustrate its dynamic behavior.

3.1 Motivation and Operating Principle

In Chapter 2, it was shown that the GFL and GFM have different behaviors. Both of them can, in their own way, control the voltage, frequency, active and reactive power by using droops in the control system, but they each have their limitations. In summary, the GFL can accurately and quickly track the power reference, which is needed by many applications (e.g. wind and solar generation). The GFM has an inherently better response in terms of grid support during a transient, which is especially relevant for islanded systems or power grids with low inertia, but it needs an energy storage system in order to compensate for the variations of its output power.

To achieve the best of both worlds, the simplest solution would be to employ both types of converter in parallel, operating independently. Unfortunately, several problems arise from that scenario. If both converters are of full rating, the equipment cost would double. If the converters are of half-rating (to avoid too much cost increase), the advantage achieved from using two converters is diminished. Besides that, it would be complicated to operate most systems (such as batteries or other types of energy storage) connected to two converters in parallel. Adaptations to their control system could be necessary in order to properly control the dc-link voltage and to make the converters work together in following the desired power and voltage setpoints.

A solution to attain the advantages of both the GFL and GFM simultaneously must rely on a single converter, of full-rating as usual, with a modified, hybrid control system. In this work, this converter is called the *Hybrid Control Converter* (HCC).

Two different electrical systems are analyzed, as shown in Figure 3.1. In the two-converter system shown in Figure 3.1a, there are two converters, with distinct control systems, connecting some dc equipment (such as a RES, BESS or HVDC link) to the ac grid. The output voltages of each converter (each calculated by its own control system) are $\boldsymbol{v}_1(t)$ and $\boldsymbol{v}_2(t)$, and their filter impedances are $Z_1 = R_1 + j\omega L_1$ and $Z_2 = R_2 + j\omega L_2$. The single-converter system, shown in Figure 3.1b, has only one converter, the HCC, and its filter impedance $Z_f = R_f + j\omega L_f$. A hybrid control system controls its output voltage, $\boldsymbol{v}_{HCC}(t)$.

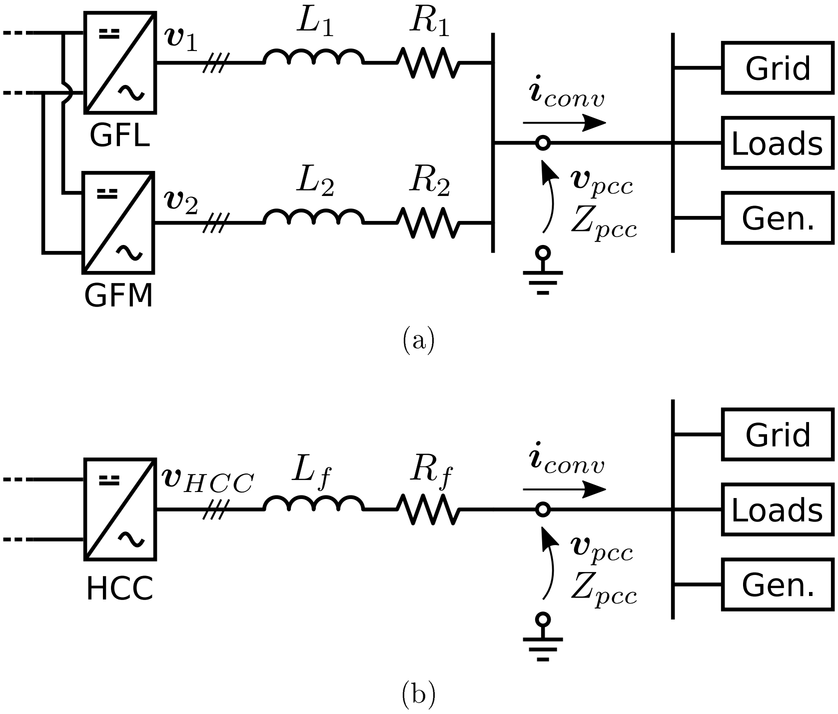

Figure 3.1: Single-line diagram of (a) a system comprised of two individual converters with distinct control systems (GFL and GFM) and (b) a system comprising a single converter with hybrid control, the HCC, which has the same overall behavior as the two-converter system.

The behavior of the two-converter system is desirable, but as mentioned before, such a system is not really economically feasible. Therefore, a hybrid control system is needed, such that the HCC by itself can have a similar behavior to that of a pair of individual converters in parallel. *The HCC is one single converter, with a hybrid control system that emulates the behavior of two individual converters (one GFL and one GFM), that would be working in parallel and simultaneously.* This is equivalent to stating that the effect of the single-converter system on the electrical grid must be the same as the effect that the two-converter system would have. From the grid's point of view, *the single-converter system is indistinguishable from the two-converter system* because both systems behave in the same way, having the same output current, active and reactive power, and presenting the same equivalent impedance (Z_{pcc}). This way, by using only the HCC (emulating two converters), there are no extra cost and issues involved in having two physical converters, while retaining the characteristics of both GFL and GFM at the same time into a single converter.

It is important to note that the following analysis does not depend on the physical converter topology, being applicable for 2- or 3-level converters, MMCs, or any other configuration. It is also unaffected by what lies in the dc-side of the converters, be it a storage system, a generation system such as a permanent-magnet wind turbine, or a terminal of an HVDC system. Therefore, the dc-side dynamics are ignored, which does not affect the validity of the developed equations.

3.2 Mathematical Model

Since the goal is to develop one converter that behaves as two, it means that the single-converter system must be made similar, or *equivalent*, to the two-converter system. Furthermore, this must hold true for both static and dynamic situations. The challenge lies in how to make the HCC behave in such a way.

One of the building blocks of electrical circuit theory is the equivalent circuit transformation [62]. It states that any circuit can be simplified to a single equivalent voltage source $\boldsymbol{v}_{eq}$ behind a single equivalent impedance Z_{eq}, as shown in Figure 3.2. The equivalent voltage and impedance are calculated in such a way that the equivalent circuit behaves just like the original one when connected to another (external) circuit.

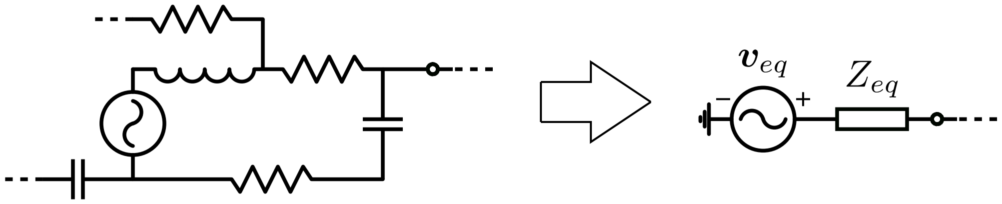

Figure 3.2: Equivalent circuit representation of an electrical circuit.

If both the two-converter and the single-converter systems are reduced to their own equivalent forms, it becomes possible to make direct comparisons. The equivalent circuits for both of these systems are considered equivalent to each other if:

$$\boldsymbol{v}_{eq,2conv} = \boldsymbol{v}_{eq,1conv}, \tag{3.1}$$

$$Z_{eq,2conv} = Z_{eq,1conv}, \tag{3.2}$$

where $\boldsymbol{v}_{eq,2conv}$ and $\boldsymbol{v}_{eq,1conv}$ are the equivalent voltages of the two-converter system and of the single-converter system, respectively, and $Z_{eq,2conv}$ and $Z_{eq,1conv}$ are their equivalent impedances.

Therefore, for the single-converter system to be equivalent to the two-converter system, the HCC's output voltage must be such that the equivalent voltages of both systems are equal. Similarly, the filter impedances must be chosen in such a way that the equivalent impedance of both systems match.

Both the GFL and GFM control techniques are employed in VSCs. This means that, even though the control system is targeting certain reference values of power, voltage and frequency, what is physically happening is that the semiconductors are switching in a controlled manner so that a specific voltage appears at the converter ac terminals. A GFL or GFM (or in fact any VSC) are in reality controlled voltage sources, even when they are controlling the power delivered to the grid. As all converters in this analysis are VSCs, they can be represented as controlled voltage sources when performing the electric circuit analyses, and their filter as a series-connected RL impedance. Even in case they are LCL filters, neglecting the parallel capacitive branch is a usual simplification performed in most control system studies, only affecting the modeling of the filter for frequencies much smaller or greater than the nominal value. The effect of LCL filters in the mathematical model is discussed in more detail in Chapter 5.

The single-converter system, as shown in Figure 3.1b, is already in the *equivalent-voltage-source-behind-an-equivalent-impedance* form. Therefore, it can be directly stated that:

$$\boldsymbol{v}_{eq,1conv} = \boldsymbol{v}_{HCC}, \tag{3.3}$$

$$Z_{eq,1conv} = R_f + j\omega L_f. \tag{3.4}$$

For the two-converter system, some mathematical manipulations must be performed to transform the two branches into a single one. The equivalent voltage is equal to the open-circuit voltage at the PCC, as in Figure 3.3a. The equivalent impedance is calculated from the impedances of the electrical circuit without the voltage sources, as in Figure 3.3b.

Kirchhoff's Voltage Law [63] can be applied to the circuit shown in Figure 3.3a. The following calculations are done in the frequency domain (denoted by uppercase variables $\boldsymbol{V}(s), \boldsymbol{I}(s)$). The loop current is:

$$\boldsymbol{V}_1(s) - \boldsymbol{V}_2(s) = (R_1 + R_2 + sL_1 + sL_2)\,\boldsymbol{I}_{loop}(s), \tag{3.5}$$

$$\boldsymbol{I}_{loop}(s) = \frac{\boldsymbol{V}_1(s) - \boldsymbol{V}_2(s)}{s(L_1 + L_2) + (R_1 + R_2)}, \tag{3.6}$$

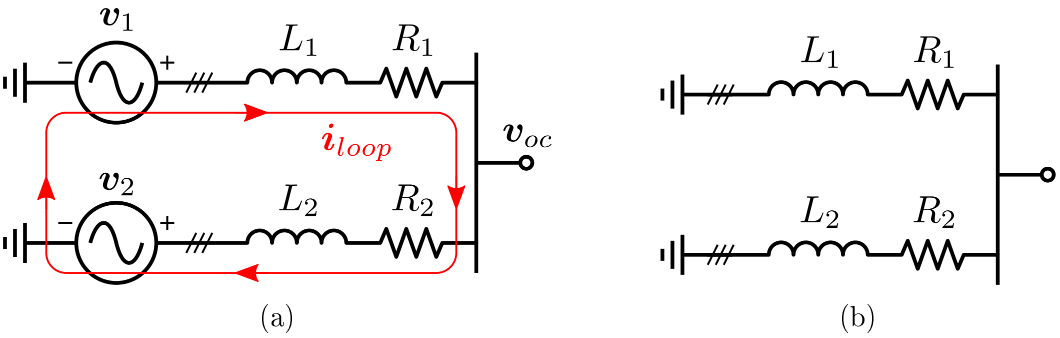

Figure 3.3: Circuits used to calculate (a) the open-circuit voltage $\boldsymbol{v}_{oc} = \boldsymbol{v}_{eq,2conv}$ and (b) the equivalent impedance $Z_{eq,2conv}$ of the two-converter system.

where $\boldsymbol{V}_1(s), \boldsymbol{V}_2(s), \boldsymbol{I}_{loop}(s)$ are the frequency domain representations of the first converter's (GFL) voltage $\boldsymbol{v}_1(t)$, the second converter's (GFM) voltage $\boldsymbol{v}_2(t)$ and the loop current $\boldsymbol{i}_{loop}(t)$, respectively.

From here on, for simplicity, the frequency domain indicator "(s)" and the time-domain indicator "(t)" are omitted from the variables representing voltages and currents. The open-circuit voltage is:

$$\boldsymbol{V}_{oc} = \boldsymbol{V}_2 + (R_2 + sL_2)\,\boldsymbol{I}_{loop}, \tag{3.7}$$

$$\boldsymbol{V}_{oc} = \boldsymbol{V}_2 + (R_2 + sL_2)\,\frac{\boldsymbol{V}_1 - \boldsymbol{V}_2}{s(L_1 + L_2) + (R_1 + R_2)}, \tag{3.8}$$

$$\boldsymbol{V}_{eq,2conv} = \boldsymbol{V}_{oc} = \left[\frac{sL_2 + R_2}{s(L_1 + L_2) + (R_1 + R_2)}\right]\boldsymbol{V}_1 + \left[\frac{sL_1 + R_1}{s(L_1 + L_2) + (R_1 + R_2)}\right]\boldsymbol{V}_2. \tag{3.9}$$

The equivalent impedance of the two-converter system is calculated using the circuit shown in Figure 3.3b. This calculation is made simpler by considering the reactance values (e.g. $X_L = \omega L$), and not the inductance-based frequency domain calculation (sL) in this case. The result is:

$$\frac{1}{Z_{eq,2conv}} = \frac{1}{R_1 + jX_1} + \frac{1}{R_2 + jX_2}, \tag{3.10}$$

$$\frac{1}{Z_{eq,2conv}} = \frac{R_1 + jX_1 + R_2 + jX_2}{(R_1 + jX_1)(R_2 + jX_2)}, \tag{3.11}$$

$$Z_{eq,2conv} = \frac{(R_1R_2) - (X_1X_2) + j(R_1X_2 + R_2X_1)}{(R_1 + R_2) + j(X_1 + X_2)}. \tag{3.12}$$

The equivalent impedance can be split into real and imaginary components by rationalization:

$$Z_{eq,2conv} = \frac{(R_1R_2) - (X_1X_2) + j(R_1X_2 + R_2X_1)}{(R_1 + R_2) + j(X_1 + X_2)} \cdot \frac{(R_1 + R_2) - j(X_1 + X_2)}{(R_1 + R_2) - j(X_1 + X_2)}. \quad (3.13)$$

Developing (3.13), the result is:

$$Z_{eq,2conv} = Z_{eq,2conv,real} + jZ_{eq,2conv,imag}, \quad (3.14)$$

$$Z_{eq,2conv,real} = \frac{(R_1 + R_2)(R_1R_2 - X_1X_2) + (X_1 + X_2)(R_1X_2 + R_2X_1)}{(R_1 + R_2)^2 + (X_1 + X_2)^2}, \quad (3.15)$$

$$Z_{eq,2conv,imag} = \frac{(R_1 + R_2)(R_1X_2 + R_2X_1) - (X_1 + X_2)(R_1R_2 - X_1X_2)}{(R_1 + R_2)^2 + (X_1 + X_2)^2}. \quad (3.16)$$

If the two converters' filters are assumed to have the same impedance ratio, i.e.:

$$\frac{L_1}{R_1} = \frac{L_2}{R_2}, \quad (3.17)$$

the developed equations can be greatly simplified and also become frequency-invariant. Nevertheless, this assumption is not necessary for the validity of the developed hybrid control system. More detail about this assumption is discussed in a later section of this chapter.

Then, to enable an easier manipulation of the equations, two constants are defined: k_1 and k_2, the *impedance ratios*. They essentially quantify the difference in size between the filter impedances of the two branches, as in:

$$k_1 = \frac{R_1}{(R_1 + R_2)} = \frac{L_1}{(L_1 + L_2)}, \quad (3.18)$$

$$k_2 = \frac{R_2}{(R_1 + R_2)} = \frac{L_2}{(L_1 + L_2)}, \quad (3.19)$$

$$k_1 + k_2 = 1. \quad (3.20)$$

Applying (3.18)-(3.19) in (3.9), the two-converter system's equivalent voltage is simplified to:

$$\boldsymbol{V}_{eq,2conv} = \left[\frac{sk_2(L_1 + L_2) + k_2(R_1 + R_2)}{s(L_1 + L_2) + (R_1 + R_2)}\right] \boldsymbol{V}_1 + \left[\frac{sk_1(L_1 + L_2) + k_1(R_1 + R_2)}{s(L_1 + L_2) + (R_1 + R_2)}\right] \boldsymbol{V}_2, \quad (3.21)$$

$$\boldsymbol{V}_{eq,2conv} = k_2\boldsymbol{V}_1 + k_1\boldsymbol{V}_2. \quad (3.22)$$

In the time domain, (3.22) becomes simply:

$$\boldsymbol{v}_{eq,2conv} = k_2\boldsymbol{v}_1 + k_1\boldsymbol{v}_2. \quad (3.23)$$

The real part of the two-converter system's equivalent impedance from (3.15) becomes:

$$\begin{aligned} Z_{eq,2conv,real} = {} & \frac{(R_1+R_2)\left[k_1k_2(R_1+R_2)^2 - k_1k_2(X_1+X_2)^2\right]}{(R_1+R_2)^2+(X_1+X_2)^2} + \\ & + \frac{(X_1+X_2)\left[k_1k_2(R_1+R_2)(X_1+X_2) + k_2k_1(R_1+R_2)(X_1+X_2)\right]}{(R_1+R_2)^2+(X_1+X_2)^2}, \end{aligned} \tag{3.24}$$

$$Z_{eq,2conv,real} = k_1k_2\frac{(R_1+R_2)\left[(R_1+R_2)^2+(X_1+X_2)^2\right]}{(R_1+R_2)^2+(X_1+X_2)^2}, \tag{3.25}$$

$$Z_{eq,2conv,real} = k_1k_2(R_1+R_2), \tag{3.26}$$

$$R_{eq,2conv} = Z_{eq,2conv,real} = k_1k_2(R_1+R_2), \tag{3.27}$$

$$R_{eq,2conv} = k_1R_2 = k_2R_1. \tag{3.28}$$

And, finally, its imaginary part from (3.16) becomes:

$$\begin{aligned} Z_{eq,2conv,imag} = {} & \frac{(R_1+R_2)\left[k_1k_2(R_1+R_2)(X_1+X_2) + k_2k_1(R_1+R_2)(X_1+X_2)\right]}{(R_1+R_2)^2+(X_1+X_2)^2} + \\ & - \frac{(X_1+X_2)\left[k_1k_2(R_1+R_2)^2 - k_1k_2(X_1+X_2)^2\right]}{(R_1+R_2)^2+(X_1+X_2)^2}, \end{aligned} \tag{3.29}$$

$$Z_{eq,2conv,imag} = k_1k_2\frac{(X_1+X_2)\left[2(R_1+R_2)^2-(R_1+R_2)^2+(L_1+L_2)^2\right]}{(R_1+R_2)^2+(X_1+X_2)^2}, \tag{3.30}$$

$$Z_{eq,2conv,imag} = k_1k_2(X_1+X_2), \tag{3.31}$$

$$L_{eq,2conv} = \frac{1}{\omega}Z_{eq,2conv,imag} = k_1k_2(L_1+L_2), \tag{3.32}$$

$$L_{eq,2conv} = k_1L_2 = k_2L_1. \tag{3.33}$$

It is worth noting that, as mentioned before, the equations for the two-converter system's equivalent voltage, resistance and reactance ((3.23), (3.28) and (3.33)) are independent of the frequency ω. This means they are frequency-invariant, which leads to a mathematical model that is valid for the entire frequency spectrum, including harmonic components.

The equivalent voltage and impedance for both the two-converter and the single-converter systems are calculated. As mentioned before, the two systems are equivalent to each other if their equivalent voltages and impedances are equal, as in (3.1)-(3.2). The calculated values lead to:

$$\boldsymbol{v}_{eq,1conv} = \boldsymbol{v}_{eq,2conv}, \tag{3.34}$$

$$\boldsymbol{v}_{HCC} = k_2\boldsymbol{v}_1 + k_1\boldsymbol{v}_2, \tag{3.35}$$

and:

$$Z_{eq,1conv} = Z_{eq,2conv}, \tag{3.36}$$

$$R_f = k_1 R_2 = k_2 R_1, \tag{3.37}$$

$$L_f = k_1 L_2 = k_2 L_1. \tag{3.38}$$

This essentially means that the two-converter system and the single-converter system are equivalent if:

- The HCC's output voltage is a linear composition of the output voltages from the individual converters of the two-converter system, as in (3.35);
- The filter impedances of the two converters are proportional to the filter impedance of the HCC, as in (3.37)-(3.38).

The requirements to make the HCC equivalent to a pair of converters working in parallel have now been established and demonstrated. The next step is to define the hybrid control system such that the single-converter system can properly emulate the two-converter system.

In the two-converter system, there are two converters with their own control systems. Each converter would have its own control software and hardware, including sensors and processing units (where the control systems are actually implemented). The sensors would measure the current and voltage just after the converters' filters. In practical converter implementations with LCL filters, the voltage is usually measured at the filter capacitor to mitigate the switching effect in the measurements; since in this case an RL filter is considered, the voltage is assumed to be measured at the PCC. These measurements would go into the processing unit, where the control system generates the reference output voltage for the converter. The HCC system only includes a single converter, with its own controller hardware, similar to the ones described previously. This is shown in Figure 3.4, where each block labeled "control system" includes all control logic, including PLLs, Park or Clarke transformations, PI or PR controllers, droops, or anything else that might be used according to a specific control strategy.

The target application is a system with one single converter, the HCC. But its output voltage, from (3.35), comes from the output voltages of two individual emulated converters, which are calculated by their own control systems.

As mentioned before, the single- and two-converter systems should be indistinguishable from the point of view of the grid. This means that, for any observer, the output current of the HCC is equal to what would be the sum of the two converters' output currents in the emulated two-converter system. Assuming the HCC

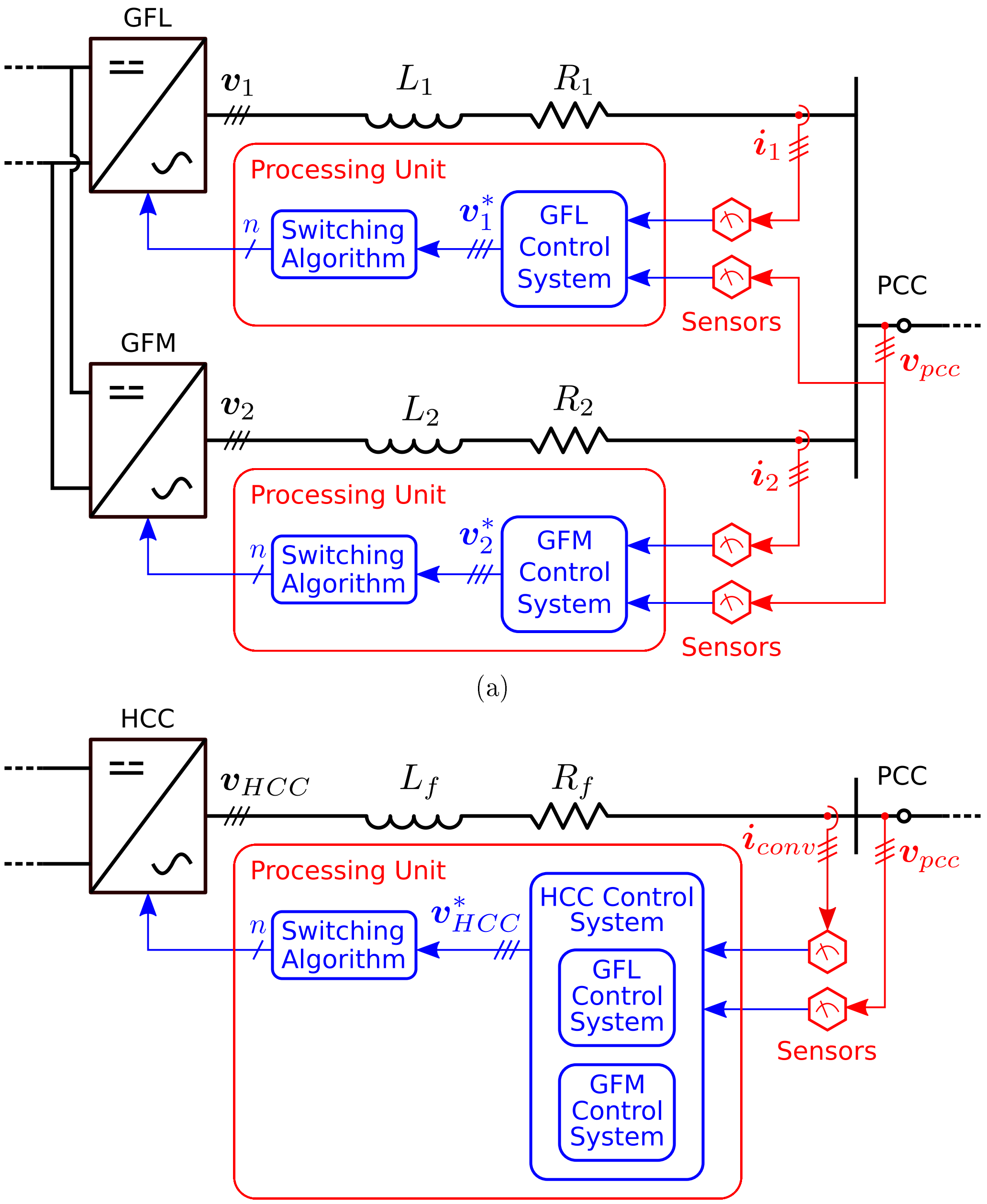

(a)

(b)

Figure 3.4: Schematic of the processing units, control systems and measurements taken by each converter in the (a) two-converter system, and in the (b) single-converter system.

can properly emulate two converters, when the HCC controller measures the current and voltage at the PCC, all it knows is that they were *either produced by a two-converter system, or by a single-converter system that behaves just like it would.* The controller cannot really discern which is the actual system, because they would both have the same output. Therefore, if the two individual control systems from the emulated two-converter system are implemented inside the HCC controller, they can take those measurements and calculate their individual reference output voltages, just as they would be if they were actually implemented in a physical two-converter system. *Because they believe they are controlling two individual converters.* The two reference output voltages are then merged, according to (3.35), and the HCC generates its output voltage. This results in the exact same effect on the grid that would happen if there were two physical converters working in parallel. Since the HCC is equivalent to a two-converter system and can emulate its behavior, each of the two individual control systems, residing inside the overall HCC control system, keep working seamlessly.

In reality, to fully make this work, two extra steps must be taken. The first is that, as described in (3.37)-(3.38), the single-converter system is actually only equivalent to a two-converter system if their filter impedances match. In this case, the actual converter being implemented is the HCC, so its filter impedance is known from manufacturer specifications. Therefore, since the two-converter system is only being emulated, its filter impedances can simply be chosen to match these equations. More detail on choosing the impedance values for the two-converter filters is discussed later.

The final step is to deal with the issue that each of these two individual control systems need as input the output current of their own emulated converter. Since in reality there is only the HCC, with its single branch, connected to the grid, the only current measurement actually available is the output current at the PCC. Therefore, the individual currents that would be present in each branch of the emulated two-converter system must be backcalculated.

These two converter currents can be calculated using Kirchhoff's Voltage Law, using the notation shown in Figure 3.5, as:

$$\boldsymbol{V}_1 - (sL_1 + R_1)\boldsymbol{I}_1 = \boldsymbol{V}_{pcc}, \tag{3.39}$$

$$\boldsymbol{V}_2 - (sL_2 + R_2)\boldsymbol{I}_2 = \boldsymbol{V}_{pcc}. \tag{3.40}$$

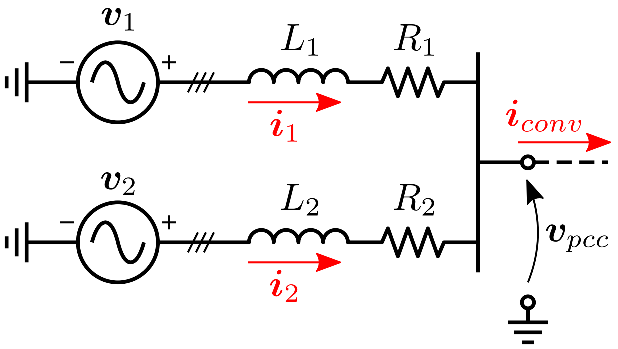

Figure 3.5: Electrical diagram used to calculate the relationship between the individual branch currents of the two-converter system and the total output current.

The current of branch 2 is:

$$\boldsymbol{I}_2 = \boldsymbol{I}_{conv} - \boldsymbol{I}_1. \tag{3.41}$$

For branch 1, the current is calculated from (3.39)-(3.41), resulting in:

$$\boldsymbol{V}_1 - (sL_1 + R_1)\,\boldsymbol{I}_1 = \boldsymbol{V}_2 - (sL_2 + R_2)\,(\boldsymbol{I}_{conv} - \boldsymbol{I}_1)\,, \tag{3.42}$$

$$(sL_1 + R_1 + sL_2 + R_2)\,\boldsymbol{I}_1 = \boldsymbol{V}_1 - \boldsymbol{V}_2 + (sL_2 + R_2)\,\boldsymbol{I}_{conv}, \tag{3.43}$$

$$\boldsymbol{I}_1 = \frac{\boldsymbol{V}_1 - \boldsymbol{V}_2}{s(L_1 + L_2) + (R_1 + R_2)} + \frac{sL_2 + R_2}{s(L_1 + L_2) + (R_1 + R_2)}\boldsymbol{I}_{conv}, \tag{3.44}$$

$$\boldsymbol{I}_1 = \frac{\boldsymbol{V}_1 - \boldsymbol{V}_2}{s(L_1 + L_2) + (R_1 + R_2)} + \frac{sk_2(L_1 + L_2) + k_2(R_1 + R_2)}{s(L_1 + L_2) + (R_1 + R_2)}\boldsymbol{I}_{conv}, \tag{3.45}$$

$$\boldsymbol{I}_1 = \frac{\boldsymbol{V}_1 - \boldsymbol{V}_2}{s(L_1 + L_2) + (R_1 + R_2)} + k_2\boldsymbol{I}_{conv}. \tag{3.46}$$

Besides that, having calculated the individual currents of the emulated two-converter system, it is possible to calculate the power each of the two converters would be producing. This way, the total output power of the HCC can be split into GFL and GFM active and reactive power, $p_{GFL}, q_{GFL}, p_{GFM}, q_{GFM}$. This brings extra flexibility in the hybrid control system design, and is explored in Chapters 6 and 7. They come from the dq-components of their reference output voltage and of the currents that were just calculated, as in:

$$p_{GFL} = \frac{3}{2}\left(v_{1,d}^{*} i_{1,d} + v_{1,q}^{*} i_{1,q}\right), \tag{3.47}$$

$$q_{GFL} = \frac{3}{2}\left(v_{1,q}^{*} i_{1,d} - v_{1,d}^{*} i_{1,q}\right), \tag{3.48}$$

$$p_{GFM} = \frac{3}{2}\left(v_{2,d}^{*} i_{2,d} + v_{2,q}^{*} i_{2,q}\right), \tag{3.49}$$

$$q_{GFM} = \frac{3}{2}\left(v_{2,q}^{*} i_{2,d} - v_{2,d}^{*} i_{2,q}\right). \tag{3.50}$$

The mathematical model of the HCC control system is then fully developed. Figure 3.6 shows the new single-converter system with its control system (in black), and the emulated two-converter system (in gray). The individual GFL and GFM control systems (in green) are common to both systems. The idea behind the figure is to emphasize that both systems are in fact equivalent. The diagram in black+green leads to the same behavior as gray+green. The HCC and the emulated system are represented side-by-side not to imply that they are actually working in parallel, but to show that they are interchangeable, as they would have the same effect on the grid. Because of this, the two individual control systems can coexist inside the HCC overall control system. They behave independently, believing they are controlling two individual converters, but in the end acting on a single converter, the HCC.

Since, as mentioned before, one of the two control systems is a GFL and the other is a GFM, they can also be called the *GFL-part* and the *GFM-part* of the HCC control system.

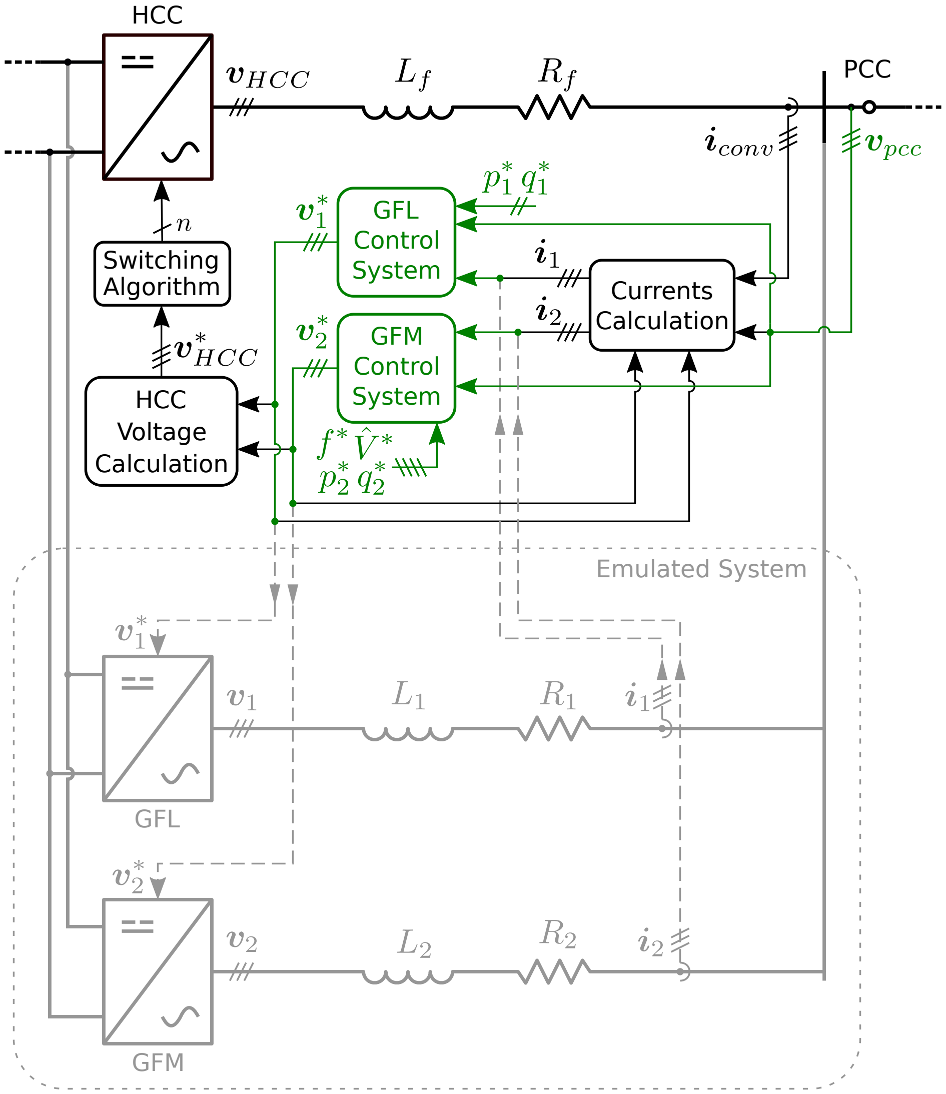

Figure 3.6: Comparison between the single-converter system (black) and the emulated two-converter system (gray). The two individual control systems (green) act on the HCC, while believing they are controlling two individual converters.

3.3 Hybrid Control System

At risk of repetition, a summary of the developed concepts and of the proposed hybrid control system is presented.

The developed equations show that it is possible for a single-converter system, employing the HCC, to emulate the behavior of a two-converter system, that includes a GFL and a GFM. These two control systems, which are now part of the overall HCC control system, operate just as they would if they were actually controlling two individual converters, even though they are both acting on the HCC. The reference output voltages of the two control systems are combined using (3.35), and delivered to the switching algorithm of the HCC. With this output voltage, the HCC has some effect on the grid, which is equal to what would happen if in reality there were two physical converters operating in parallel. The grid voltage and currents are measured, the currents that would be present in each branch of the emulated system are calculated using (3.41) and (3.46), and the two individual control systems operate as usual, believing that they are controlling two individual converters. The overall HCC control system, with the two individual control systems, its GFL- and GFM-parts, is shown in detail in Figure 3.7.

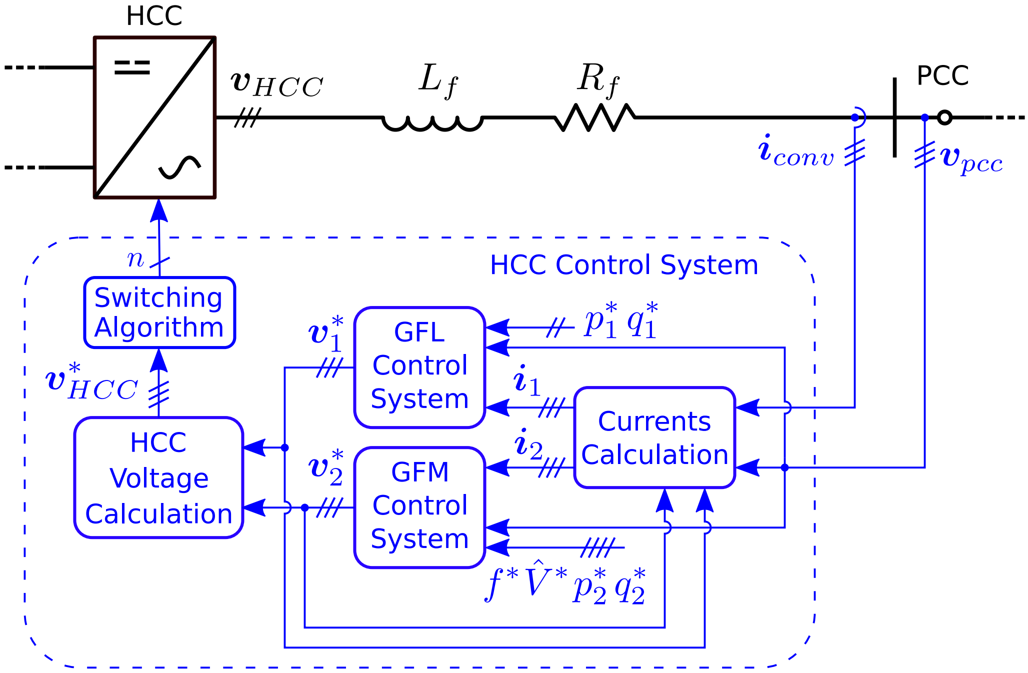

Figure 3.7: Proposed hybrid control system for the HCC.

Since the two individual converters are only emulated, there is of course no need to include a switching algorithm for the GFL- and GFM-parts of the HCC control system. This means that the two reference output voltages can be used directly to calculate the final HCC reference output voltage.

The main equations used in the HCC control system, as described in the previous section, are summarized here:

$$\boldsymbol{V}^*_{HCC} = k_2\boldsymbol{V}^*_1 + k_1\boldsymbol{V}^*_2, \tag{3.51}$$

$$\boldsymbol{I}_1 = \frac{\boldsymbol{V}_1 - \boldsymbol{V}_2}{s(L_1 + L_2) + (R_1 + R_2)} + k_2\boldsymbol{I}_{conv}, \tag{3.52}$$

$$\boldsymbol{I}_2 = \boldsymbol{I}_{conv} - \boldsymbol{I}_1, \tag{3.53}$$

$$k_1 = \frac{R_1}{(R_1 + R_2)} = \frac{L_1}{(L_1 + L_2)}, \tag{3.54}$$

$$k_2 = \frac{R_2}{(R_1 + R_2)} = \frac{L_2}{(L_1 + L_2)}, \tag{3.55}$$

$$R_f = k_1 R_2 = k_2 R_1, \tag{3.56}$$

$$L_f = k_1 L_2 = k_2 L_1. \tag{3.57}$$

In the end, the individual blocks inside the overall HCC control system have the following inputs and outputs:

- Currents Backcalculation Module
  - input: measured voltage at the PCC ($\boldsymbol{v}_{pcc}$);
  - input: measured output current ($\boldsymbol{i}_{conv}$);
  - input: reference output voltage from the GFL-part ($\boldsymbol{v}_1^*$);
  - input: reference output voltage from the GFM-part ($\boldsymbol{v}_2^*$);
  - output: calculated current of the GFL-part ($\boldsymbol{i}_1$);
  - output: calculated current of the GFM-part ($\boldsymbol{i}_2$);
- GFL control system (or GFL-part of the HCC control system):
  - input: reference values used by this particular control system implementation, usually active and reactive power (p_1^*, q_1^*);
  - input: measured voltage at the PCC ($\boldsymbol{v}_{pcc}$);
  - input: GFL converter current, calculated by the Currents Backcalculation Module ($\boldsymbol{i}_1$);
  - output: reference output voltage ($\boldsymbol{v}_1^*$);
- GFM control system:
  - input: reference values used by this particular control system implementation, usually voltage amplitude, frequency, active and reactive power ($\hat{V}^*, f^*, p_2^*, q_2^*$);
  - input: measured voltage at the PCC ($\boldsymbol{v}_{pcc}$);
  - input: GFM converter current, calculated by the Currents Backcalculation Module ($\boldsymbol{i}_2$);
  - output: reference output voltage ($\boldsymbol{v}_2^*$);
- HCC Voltage Calculation Module
  - input: reference output voltage from the GFL-part ($\boldsymbol{v}_1^*$);
  - input: reference output voltage from the GFM-part ($\boldsymbol{v}_2^*$);

  - output: reference HCC output voltage ($\boldsymbol{v}^{*}_{HCC}$).

Some points are very important to highlight. During the mathematical development, no assumption of any kind was made about the control systems of the individual converters. This means that they can be implemented as any kind of GFL or GFM. The GFL could have droops or not, be based on the Park or Clarke transform, include specific schemes for harmonic output current control or not, include low-pass filters at its input references or not. The GFM could be implemented with Synchonverter control, Matching control or any other technique, include current limitation schemes or not, etc. All that is needed is to merge their reference output voltages, and deliver the result to the HCC switching algorithm. This is a valuable characteristic of the HCC: its GFL- and GFM-parts can be implemented with usual, state-of-the-art techniques, without any inherent adaptation needed. They can be tuned and analyzed according to best practices, as if these two converters actually existed and were operating independently.

Another positive aspect is that the HCC always emulates a GFL and a GFM, which means it has characteristics of both at all times. With usual converters, a possibility to try and achieve these characteristics is to switch from GFL to GFM modes of operation depending on the grid state or transient scenario [24]. The problem is that this change could lead to instability and a delayed transient response, because the control system will need to detect some measurable metric (e.g. variations of grid voltage or frequency) to trigger the mode switch. The HCC is always GFL and GFM at the same time, not requiring any kind of transition between operating modes.

Besides that, as mentioned before, the equations result in a frequency-invariant mathematical model. This means that the HCC can emulate the behavior of a two-converter system considering any frequency involved. This is especially important if the application on which the HCC is used requires harmonic currents injection, and to enable frequency ramp-up when performing black-start.

It is worth noting that the HCC may require a processing unit with increased computational power, since it essentially implements two individual control systems at once. This is a separate analysis that should be conducted on a case-by-case basis. Besides that, a possible limitation of the HCC is that it emulates the behavior of two converters that must have a filter impedance with a value higher than the actual impedance of the HCC. This may reduce its operation range because it could limit its active and reactive power capability.

3.4 Summary of the Converter Design Process

It is useful to summarize the steps an engineer would take when designing an HCC for a proposed application.

First, the converter topology is chosen (2-level, NPC, MMC...). This choice takes into account hardware costs, dynamic performance, harmonic characteristics, required robustness and reliability metrics, and other possible requirements for this particular application. The converter filter is designed (R_f, L_f), taking into account the specific harmonic characteristics of the chosen converter topology and the grid requirements. In fact, these are the first steps in designing any kind of converter for any application.

Then, the engineer chooses the desired impedance ratios, k_1 and k_2, that define the filter impedances of the two-converter system that is emulated by the HCC. It seems intuitive to choose $k_1 = k_2 = 0.5$, resulting in the two emulated converters having the same value of filter impedance. Nevertheless, if either the GFL or GFM control systems could benefit from a lower filter impedance for some reason, these values can be tweaked to have one of the converters with a smaller filter impedance than the other. With the impedance ratios chosen, and knowing the impedance values of the actual HCC filter (R_f, L_f), the filter impedances of the two-converter system (R_1, L_1, R_2, L_2) are calculated according to (3.37) and (3.38). The two-converter system which is emulated by the HCC is established.

Finally, the GFL and GFM control systems can be chosen and designed, individually, based on the emulated two-converter system. Their gains can be designed based on their filter impedances or on any other technique, according to usual best practices. The engineer may choose any type of control system he/she wants for the GFL and GFM, based on experience, performance or any other metric. Then, these two control systems are employed in the final HCC control system.

The design process is finished. The developed equations that tie together the GFL- and GFM-parts of the HCC control system, (3.35), (3.41) and (3.46), are included, and the hybrid control system is done.

There is one detail left to discuss about the impedance ratios. As mentioned before, R_1, R_2, L_1, L_2 are the resistance and inductance values of the GFL and GFM from the two-converter system, which is being emulated by the HCC. Therefore, these values can, in principle, be defined freely and independently of each other by the engineer. The equations developed in previous sections assume that the two filters have the same L/R ratio just for simplicity. Without this assumption, the impedance ratios k_1 and k_2 can be redefined as:

$$k_{1,R} = R_1/(R_1 + R_2), \tag{3.58}$$

$$k_{1,L} = L_1/(L_1 + L_2), \tag{3.59}$$

$$k_{2,R} = R_2/(R_1 + R_2), \tag{3.60}$$

$$k_{2,L} = L_2/(L_1 + L_2), \tag{3.61}$$

$$k_{1,R} \neq k_{1,L}, \tag{3.62}$$

$$k_{2,R} \neq k_{2,L}. \tag{3.63}$$

Consequently, one of the two emulated converters may have a higher L/R ratio than the other, which could be useful for specific controller design purposes or maybe response time requirements in very specific cases. This leads to an indeterminate equation system, comprising the 2 equations used to calculate the impedances ((3.15) and (3.16)) and 4 variables ($k_{1,R}, k_{1,L}, k_{2,R}, k_{2,L}$). The engineer can solve this equation system in many ways, where a simple one is to choose the R and L values for one of the filters and simply solve for the 2 remaining variables. As for the equations that define the HCC equivalent voltage and the individual currents calculation, (3.9), (3.41) and (3.46) can be employed directly, making the mathematical model once again complete. For most cases though, it seems intuitive to design the converters in the emulated two-converter system with the same L/R ratio.

3.5 Validation

3.5.1 Proof-of-Concept Check

A simple exercise can be performed to double-check the validity of the developed equations. As mentioned before, the HCC works as if it were a two-converter system. If the filter impedance of one of the two converters approaches infinity, it is as if it were an open circuit, and the HCC would emulate a system that actually comprises only one converter connected to the PCC. This situation is shown in Figure 3.8.

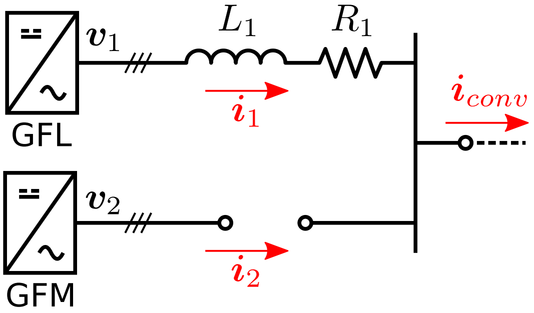

Figure 3.8: Emulated system where converter 2 is not connected to the grid, used to validate the HCC mathematical model.

Considering the scenario described, where $R_2 \to \infty$ and $L_2 \to \infty$, the impedance ratio k_2 can be calculated as:

$$k_2 = \frac{R_2}{R_1 + R_2}, \tag{3.64}$$

$$\lim_{R_2 \to \infty} k_2 = 1. \tag{3.65}$$

Converter 1's impedance R_1 can be calculated from (3.37):

$$R_f = k_2 R_1, \tag{3.66}$$

$$R_1 = \frac{R_f}{k2}, \tag{3.67}$$

$$\lim_{R_2 \to \infty} R_1 = R_f \tag{3.68}$$

Similarly, for L_1:

$$L_f = k_2 L_1, \tag{3.69}$$

$$L_1 = \frac{L_f}{k2}, \tag{3.70}$$

$$\lim_{R_2 \to \infty} L_1 = L_f \tag{3.71}$$

The HCC voltage from (3.35) becomes:

$$k_1 + k_2 = 1, \tag{3.72}$$

$$\lim_{R_2 \to \infty} k_1 = 0, \tag{3.73}$$

$$\boldsymbol{V}_{HCC} = k_2 \boldsymbol{V}_1 + k_1 \boldsymbol{V}_2, \tag{3.74}$$

$$\lim_{R_2 \to \infty} \boldsymbol{V}_{HCC} = \boldsymbol{V}_1. \tag{3.75}$$

And the converter currents from (3.41) and (3.46) become:

$$\boldsymbol{I}_1 = \frac{\boldsymbol{V}_1 - \boldsymbol{V}_2}{s(L_1 + L_2) + (R_1 + R_2)} + k_2 \boldsymbol{I}_{conv}, \tag{3.76}$$

$$\lim_{R_2 \to \infty} \boldsymbol{I}_1 = \boldsymbol{I}_{conv}, \tag{3.77}$$

$$\boldsymbol{I}_2 = \boldsymbol{I}_{conv} - \boldsymbol{I}_1, \tag{3.78}$$

$$\lim_{R_2 \to \infty} \boldsymbol{I}_2 = 0. \tag{3.79}$$

These results confirm that, in the emulated two-converter system where the GFM is actually not connected to the PCC, its current is zero, and the GFL's current is equal to the HCC current. The GFL's filter impedance is equal to the HCC impedance, and the HCC voltage reference is equal to the GFL's one. The HCC emulates a system comprised of a single converter, operating as such. This sanity check analysis corroborates the validity of the mathematical model developed for the HCC.

3.5.2 Simulations

3.5.2.1 Dynamic Behavior Validation: HCC vs GFL+GFM

To validate the proposed control strategy and confirm that the HCC actually behaves as to two converters in parallel, a simulation test system is set up similarly to the one from Section 2.4. It consists on the same grid voltage source and load connected to the PCC. Regarding the converter, two simulation cases are set up:

Case 1 is the system that was deemed economically unfeasible in the beginning of this chapter. It contains two individual converters working in parallel and connected to the PCC, as shown in Figure 3.9. The two converters are:

- one GFL, with active and reactive power references, and
- one GFM, with voltage amplitude and frequency references, and also droop control loops with active and reactive power references.

Case 2 contains, as shown in Figure 3.10, one single converter connected to the PCC, being:

- One HCC, with the same individual control systems and reference values from case 1. It is set to emulate the two converters from case 1.

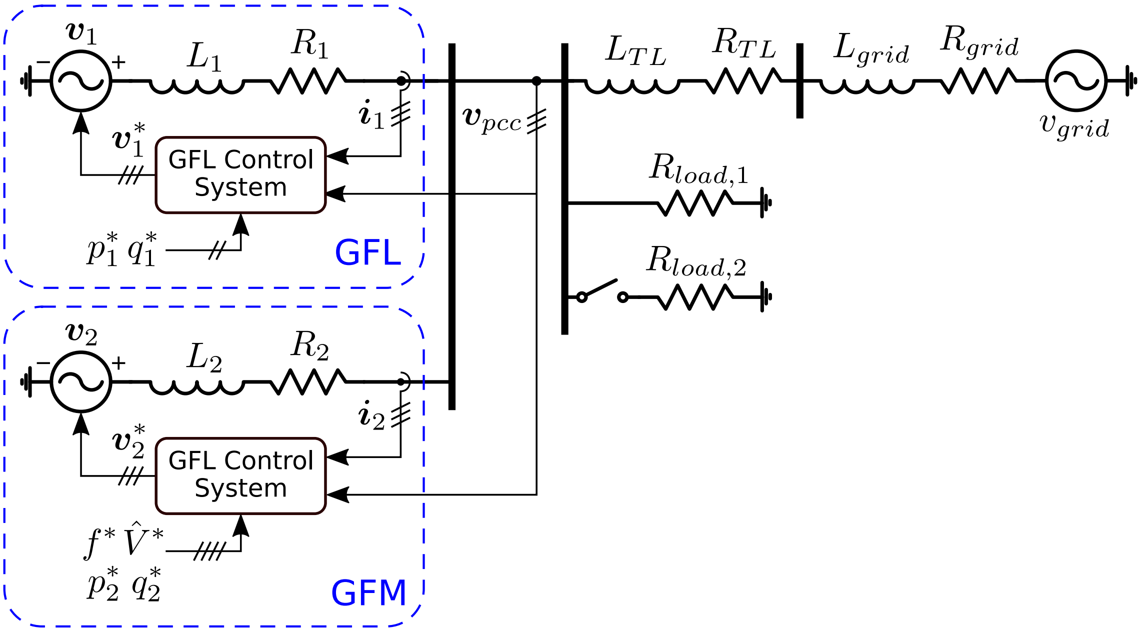

Figure 3.9: Schematic diagram of the system used to simulate case 1.

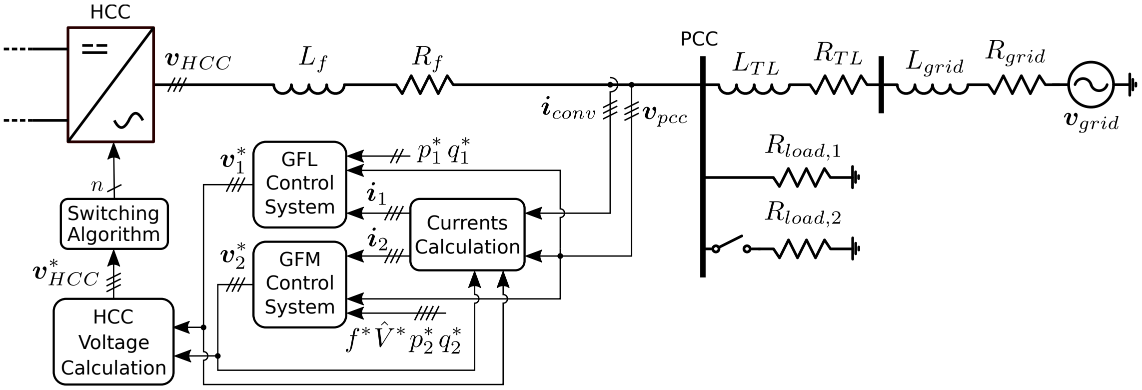

Figure 3.10: Schematic diagram of the system used to simulate case 2.

The point of interest is not on the behavior of the GFL and GFM themselves, but on the comparison between the two cases' outputs. If the HCC can really emulate a two-converter system, the output current at the PCC and the effect on the grid must be the same on both simulated cases.

The main parameters of the simulated system are the same as described previously, in Tables 2.1 and 2.2. Since both the GFL and GFM in case 1 employ the same filter impedance, as described in the tables, here the impedance values of the HCC filter, R_f and L_f are recalculated for case 2. This way, they match the impedances of the two-converter system, according to (3.37) and (3.38). This results in $R_f = 0.0025 p.u.$ and $L_f = 0.025 p.u.$.

The simulation starts in a similar manner as before. First, the system is initialized, and the converters start with a reference active power equal to zero. Just as what was shown in Section 2.4, since the load power is being supplied by the grid, the system frequency is lower than the nominal value due to the grid droop behavior. At $t = 1s$, the GFL control system receives a step in the active power reference, going from zero to 5.0 MW. Figure 3.11 shows the results for case 1. As expected, the GFL delivered power quickly goes from zero to the reference value. The GFM was already delivering some power because the grid frequency was below the nominal value, due to its automatic grid support characteristic. When the GFL power increases, the grid frequency is restored, which leads to the GFM power naturally going back to zero. The total delivered power by the ensemble GFL+GFM can also be seen in the figure.

In case 2, there is only the HCC connected to the PCC. The GFL-part of the control system receives the step change in reference power, leading to a change in its output voltage reference and, consequently, in the HCC output voltage reference. Even though there is only the HCC, it is possible to analyze the active power from its GFL- and GFM-parts, as demonstrated in (3.47) and (3.47). Figure 3.12 shows the comparison between cases 1 and 2. In Figure 3.12a, the total power delivered

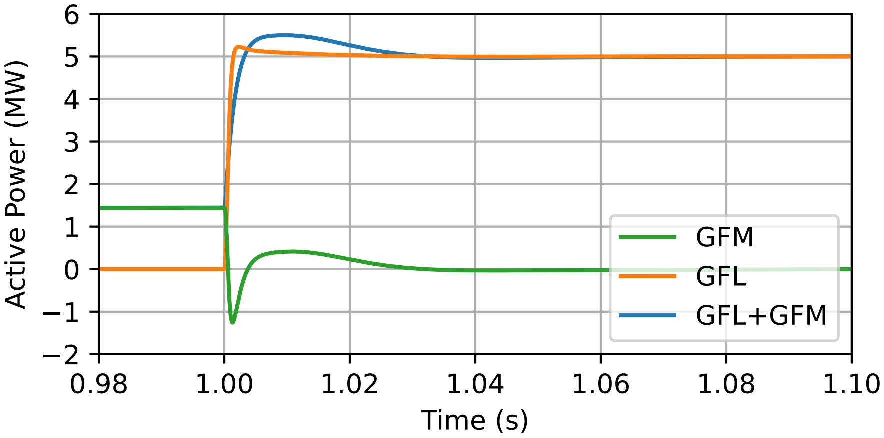

Figure 3.11: Transient response to a step in reference active power for case 1, with one GFL and one GFM.

to the PCC by the ensemble GFL+GFM is compared to the HCC output power, showcasing an essentially perfect match. Figure 3.12b shows the comparison of the individual GFL and GFM power, from case 1, with the power from the HCC's GFL- and GFM-parts in case 2, again with a near perfect match.

The effect of the power increase in the grid frequency is shown in Figure 3.13. As expected, the grid frequency increases when the converters increase their active power. Both cases lead to the same change in grid frequency. From the point of view of the grid, the ensemble GFL+GFM and an individual HCC are indistinguishable.

Next, at $t = 1.5s$, the circuit breaker is closed so that there is a step increase in load power, going from 5.0 to 10.0 MW. Figure 3.14 shows the transient behavior of both cases. In case 1, the GFL power does not change, since its reference power is kept constant, while the GFM power increases automatically to support the frequency drop due to the load increase. As part of the increased load power is now being supplied by the grid, the total output power of the ensemble GFL+GFM is lower than the full load power of 10.0 MW. In case 2, the same is observed for the total output power of the HCC, and also for the individual power of its GFL- and GFM-parts. Again, the match between the output power from cases 1 and 2 is perfect.

A comparison between the grid frequency and RoCoF after the load increase is shown in Figure 3.15. Since there is a load increase without a matching generation increase, the frequency drops, leading to a negative RoCoF in the first moments of the transient. Comparing cases 1 and 2, the grid frequency and RoCoF curves perfectly match. This means once again that, from the grid's point of view, a single HCC and a system containing a GFL and a GFM are essentially the same.

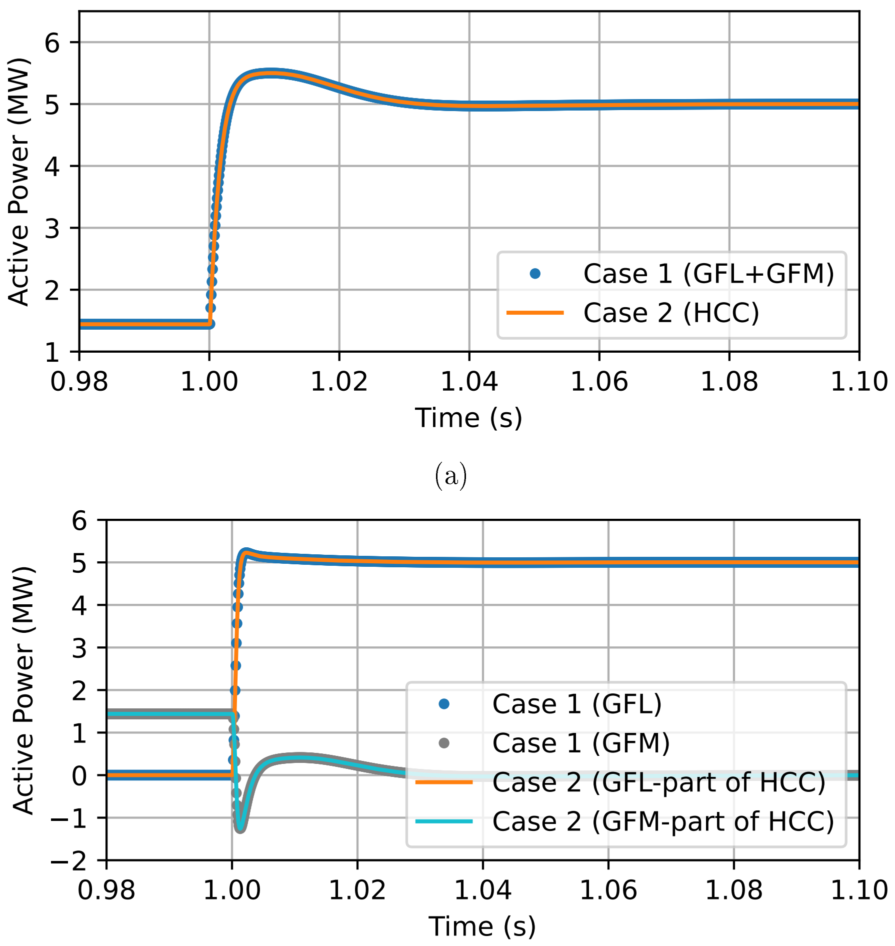

(a)

(b)

Figure 3.12: Transient response to a step in reference active power, comparing case 1 (GFL+GFM) with case 2 (HCC only). (a) Total active power delivered to the PCC and (b) individual active power delivered by each converter (GFL and GFM).

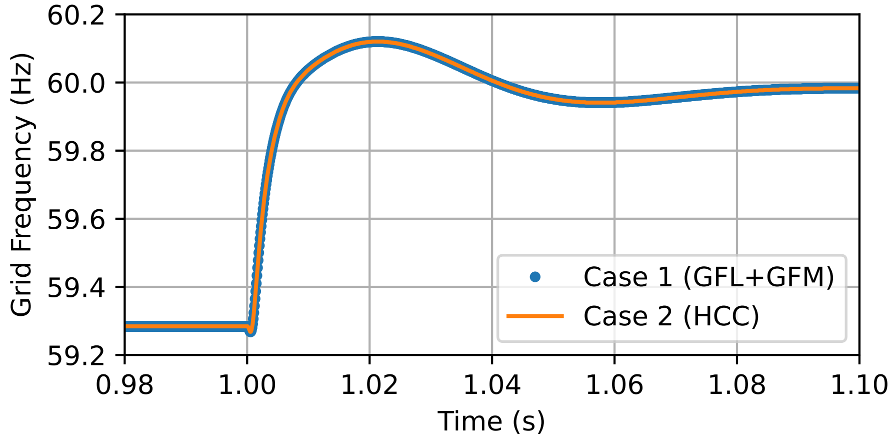

Figure 3.13: Grid frequency transient behavior following a step in reference active power, comparing case 1 (GFL+GFM) with case 2 (HCC only).

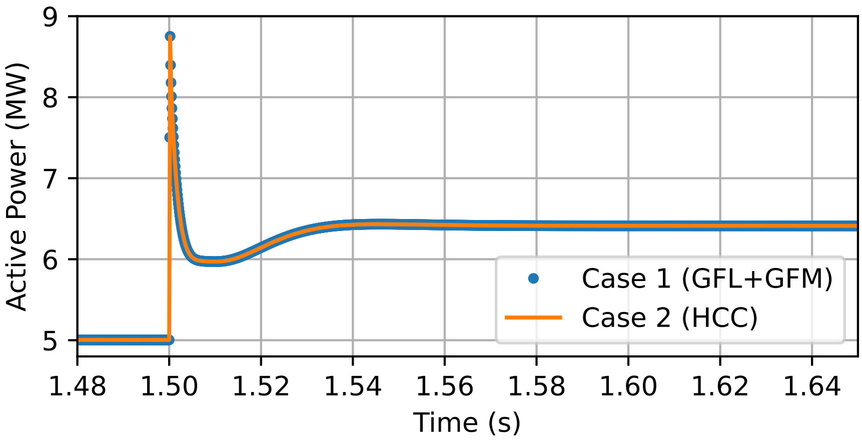

(a)

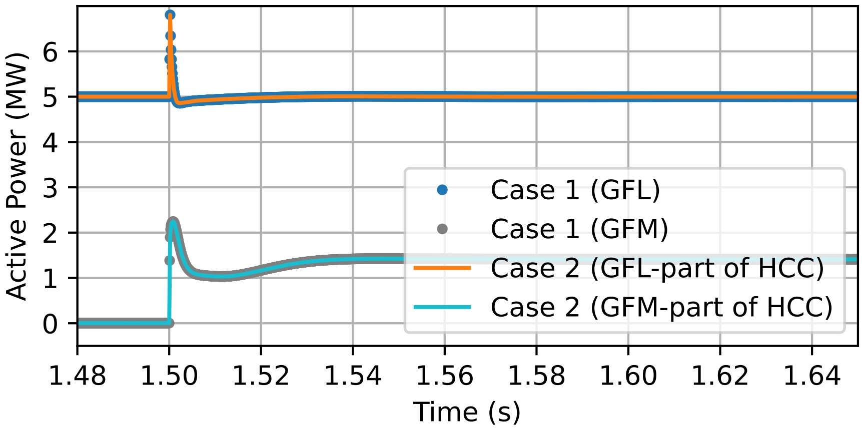

(b)

Figure 3.14: Transient response to a step load increase, comparing case 1 (GFL+GFM) with case 2 (HCC only). (a) Total active power delivered to the PCC and (b) individual active power delivered by each converter (GFL and GFM).

3.5.2.2 Black-Start

One of the main advantages of the HCC is the ability to perform black-start. Usual GFL converters need the electrical grid up and running, so they can measure the frequency using a PLL and synchronize themselves to the grid. If there is no grid, the GFL does not work, as it cannot set up the voltage reference of the grid by itself. The GFM can fulfill that role and kickstart the grid, performing the so-called *black-start*. The HCC, being both GFL and GFM at the same time, also has this capability.

To demonstrate that, the same electrical system with the HCC described in the previous section, shown in Figure 3.10, is used. The difference is that, in this case, there is no grid voltage source or transmission line, only the HCC and the load. The HCC must start the system from a standstill point of no voltage, supply the load and enable its GFL-part to work properly. No electrical or control system parameter

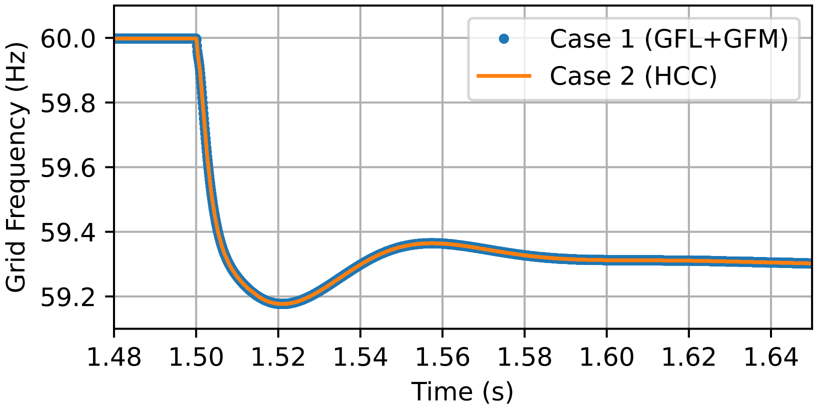

(a)

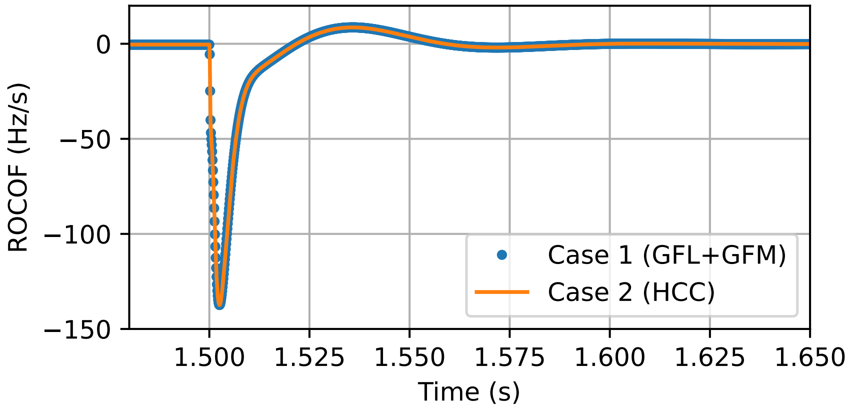

(b)

Figure 3.15: Transient response to a step increase in load power, comparing case 1 (GFL+GFM) with case 2 (HCC only). (a) Grid frequency and (b) RoCoF.

is changed from the previous section.

The simulation starts with the GFM-part of the HCC receiving ramp-up references of voltage amplitude and frequency, following a classic V/f ramp strategy. This was chosen to illustrate the scenario; other ways to perform black-start, such as starting with the frequency at nominal value, could be employed. The GFL-part receives an active power reference equal to zero. Figure 3.16 shows the phase voltage at the PCC, confirming that the HCC is able to start the system in a stable manner and follow the voltage reference.

As for the GFL-part of the HCC, Figure 3.17 shows its reference output voltage, PLL frequency and output power. It confirms that it is able to properly start working, following the grid ramp-up provided by the GFM-part, while keeping its delivered power at the reference value of zero. There are some transient disturbances right at the beginning, when the PLL is starting up and settling, but they quickly fade away. It also shows a small disturbance when the voltage ramp-up is finished, since no low-pass filter is employed in the GFM-part's ramp reference to avoid the

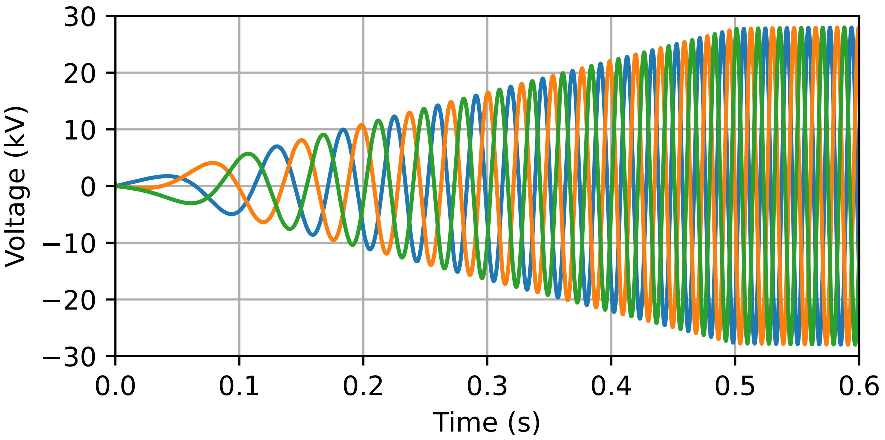

Figure 3.16: Black-start simulation, showing the PCC voltage.

abrupt change in behavior when it stops increasing.

The grid reaches a point of equilibrium. The GFM-part of the HCC is creating the grid voltage while its GFL-part is properly tracking this very same grid voltage, achieving synchronization. Due to the droop in the GFM control, since it is providing the load power, its frequency reference is reduced to around 57.5 Hz. At simulation time $t = 1.0$ s, the GFL control receives a step increase in reference active power of 5.0 MW. The GFM-part automatically adjusts; since the load starts being supplied by the GFL-part of the HCC, the GFM droop returns its reference frequency to 60 Hz. This is shown in Figure 3.18.

Then, at simulation time $t = 2.0$ s, the load increases by 5.0 MW. Since there is no change in the active power reference of the GFL control system, the GFM-part of the HCC automatically adjusts and provides the necessary power to supply the increased load. This leads to a decrease in the grid frequency setpoint. This is shown in Figure 3.19.

This result confirms that the HCC has black-start capability, due to its GFM-part, while retaining its rapid reference power tracking capability due to its GFL-part. Disturbances such as controller reference and load changes were dealt with successfully, with the HCC generating and maintaining the grid voltage by itself.

Of course, the entire premise of being able to provide black-start to a system assumes that there is an energy source in the dc-side of the converter, to provide the necessary active power to the grid during this event. This is necessary for any kind of converter that is to perform black-start, be it a regular GFM or the HCC.

3.6 Partial Conclusion

In this chapter, the operating principles of the Hybrid Control Converter (HCC) were explained and demonstrated mathematically. The proposed converter emulates

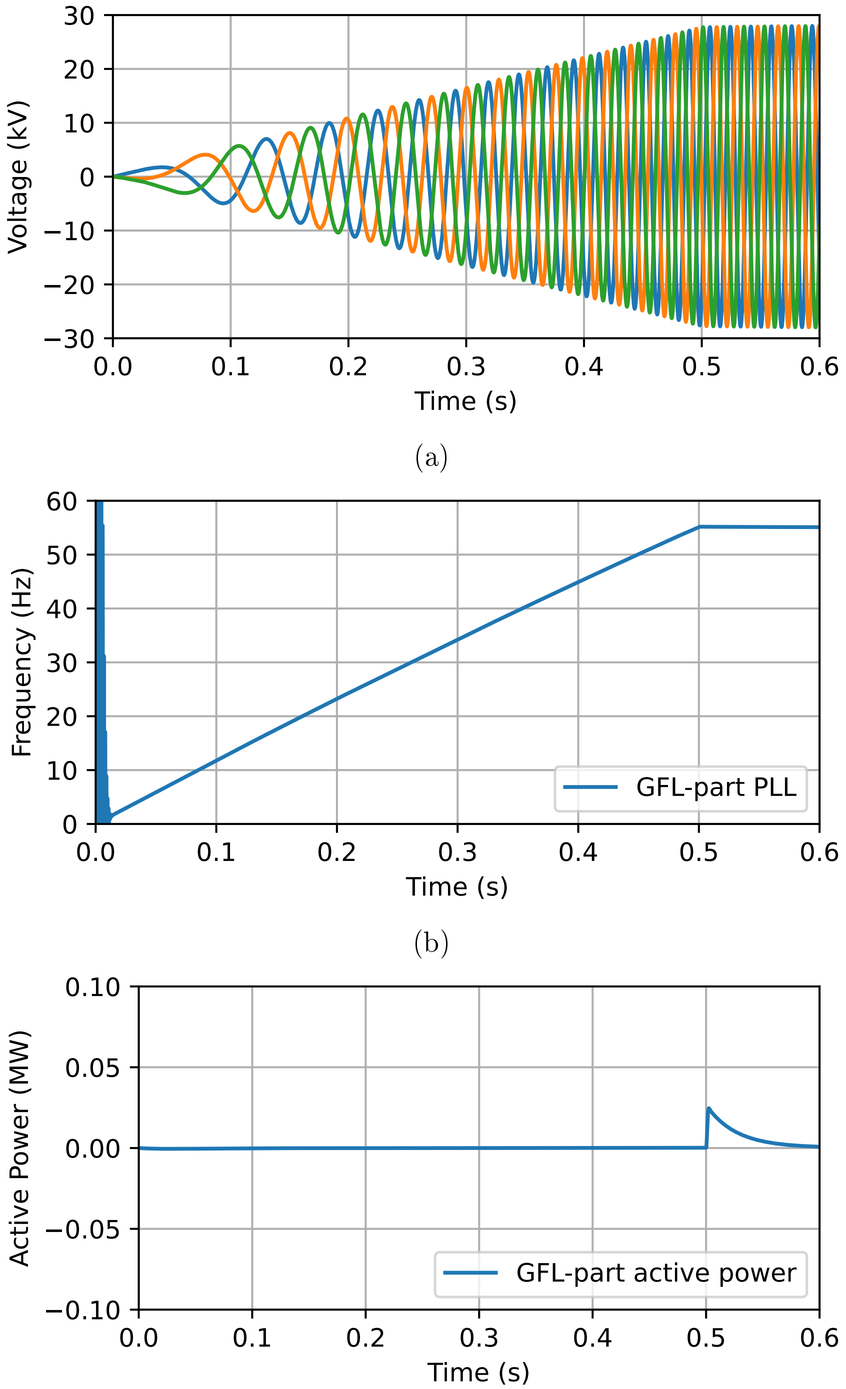

(a)

(b)

(c)

Figure 3.17: Black-start simulation, showing the (a) output voltage, (b) PLL-calculated frequency and (c) output active power of the GFL-part of the HCC.

the behavior of two individual converters working in parallel. Its control system is a simple combination of the control systems from these two, resulting in one single converter that works as if it were two, having a mix of their operating characteristics.

Simulations confirm that the HCC has similar behavior to an ensemble consisting on a GFL and a GFM. The variations of the grid frequency and RoCoF following

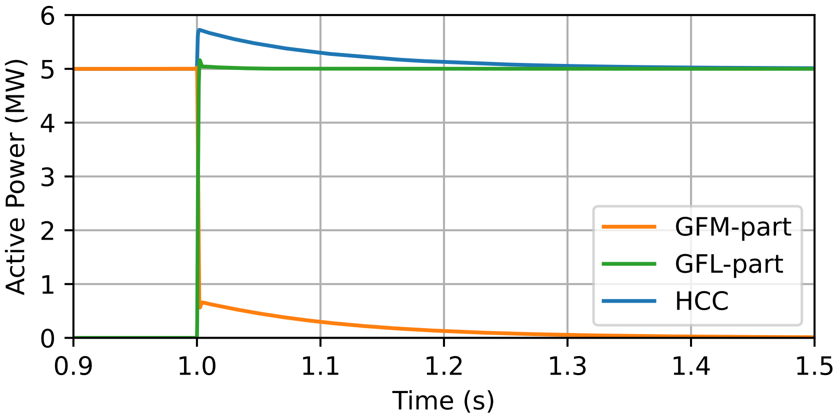

(a)

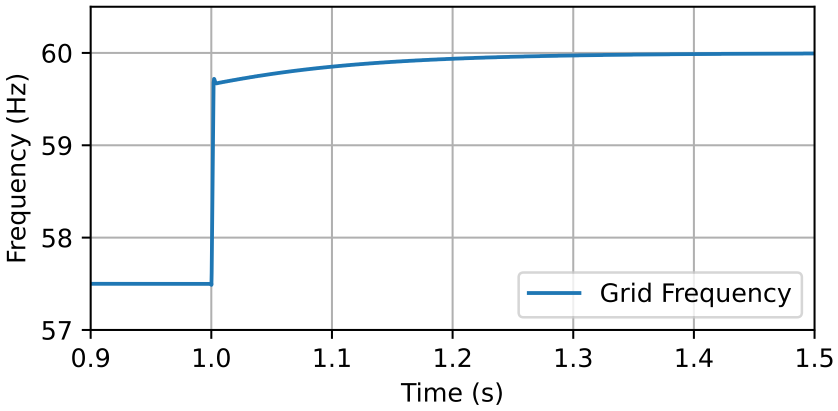

(b)

Figure 3.18: Black-start simulation, showing the (a) active power of the HCC and (b) the grid frequency after a step increase in the GFL-part's active power reference.

changes in generation and load were the same when simulating the GFL+GFM and when simulating the HCC alone. From the grid's point of view, there is no measurable difference between having two converters working in parallel or one single converter mimicking them, because they behave in the same way. This result confirms that it is possible to emulate two converters working in parallel using a single converter, with a control system consisting essentially of two separate, individual control systems, one for each of the converters to be emulated.

It seems possible to emulate any number of converters working together, since the mathematical principles used to arrive at the equivalent voltage and impedance of the HCC could be applied to a larger number of voltage sources in parallel. Nevertheless, since there are two main types of converters, GFL and GFM, it seems redundant to add multiple converters of the same kind in parallel.

The Hybrid Control Converter, which shows characteristic behaviors of both the GFL and the GFM at the same time, could enable different applications and overcome individual limitations of these types of converters. It shows the fast and

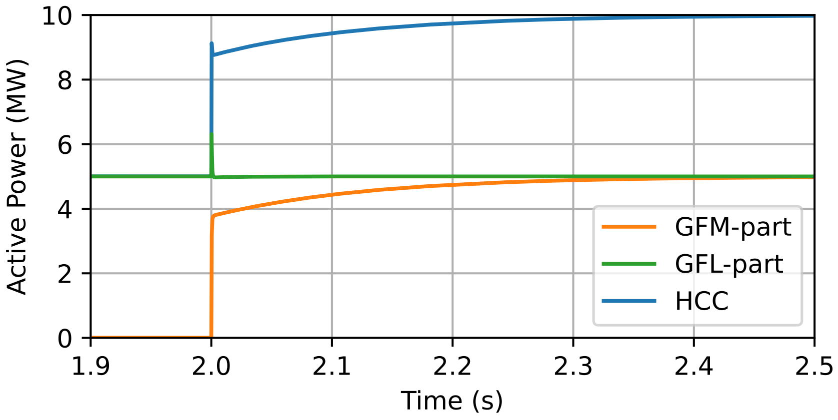

(a)

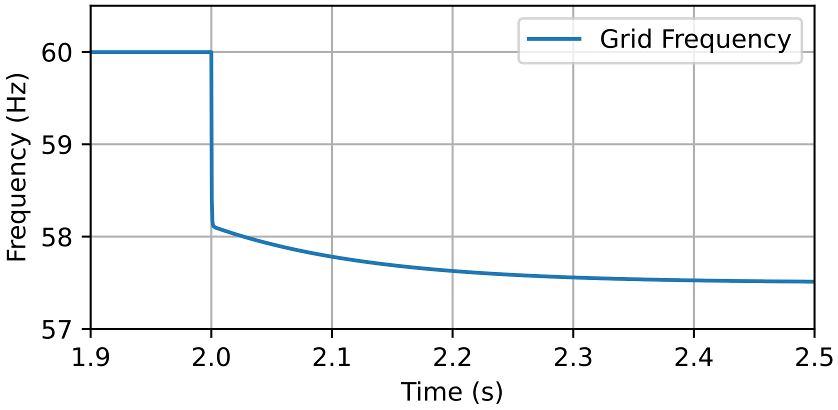

(b)

Figure 3.19: Black-start simulation, showing the (a) active power of the HCC and (b) the grid frequency after a load increase.

accurate response to changes in reference, which is the advantage of the GFL, and also the automatic, inherent grid support, characteristic of the GFM.

Chapter 4

Stability Analysis

This chapter discusses the stability of the proposed HCC by comparing it to conventional converter control systems (GFL/GFM). First, the system transfer functions including PEC, converter control system and plant are developed. Then, different criteria to evaluate the stability of a control system are presented and applied both to the HCC and to a conventional converter control system.

4.1 Introduction

In the study of control systems, various requirements and performance indicators are usually analyzed. They may include the transient response and its characteristics, such as the rise time and settling time, steady-state error, stability, and more. Among them, the stability analysis is of utmost importance, since an unstable control system may cause damage to the physical equipment it is controlling, and possibly harm people that operate it or count on it for some purpose. An electrical equipment that becomes unstable can lead to short-circuit or overcurrents in the network, damages to itself and to its surroundings, and possibly a blackout depending on the severity of the fault [64].

The Bounded-Input Bounded-Output (BIBO) definition of stability states that "a system is stable if *every* bounded input yields a bounded output". Similarly, an *unstable* system is one where "*any* bounded input yields an unbounded output" [64]. Therefore, regardless of the input (be it constant, sinusoidal, or time-varying with a given shape), a stable system's output will never approach infinity if the input is finite.

Most techniques for assessing the stability of a control system are based on analyzing its transfer function, so the first step in any stability analysis is to model the entire system. As shown in Figure 4.1, the system analyzed in this study comprises a converter, its control system and the plant it acts on.

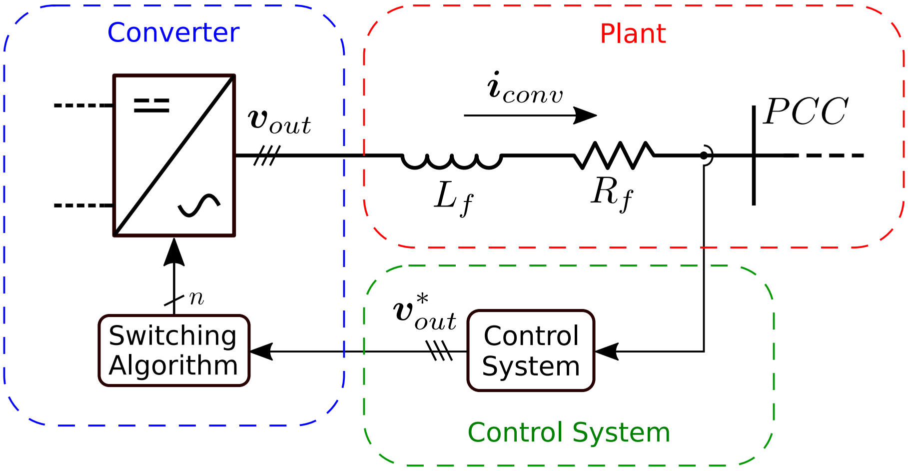

Figure 4.1: Schematic of a general electrical system, comprising a converter and a plant.

4.2 System Transfer Functions

4.2.1 Plant

The plant is defined as the physical system on which the converter output voltage acts, creating the converter current. In this case, it comprises the PEC filter and the PCC.

The output current can be described as a function of the output voltage as:

$$\boldsymbol{v}_{out}(t) - \boldsymbol{v}_{pcc}(t) = R_f \boldsymbol{i}_{conv}(t) + L_f \frac{d\boldsymbol{i}_{conv}(t)}{dt}. \tag{4.1}$$

In the following analysis, the converter voltage is assumed to not affect the voltage of the PCC, which is an usual assumption for some transfer function studies. To model this effect in more detail, especially for systems with low short-circuit ratio, the PCC could be represented as a voltage source behind an equivalent impedance. The main challenge is estimating these equivalent voltage and impedance values, because the grid state keeps changing during operation due to variations in generation and load and to changes in the grid topology. Techniques such as impedance scanning [65, 66] aim at dealing with the challenge of estimating the grid impedance and adapting the control system to it [67, 68]. This detailed representation of the grid could be especially interesting for specific cases, such as studies where there are many converters connected to nearby nodes. The logic that follows is still applicable for such cases, the only difference being that the transfer functions would need an adaptation to the v_{pcc} component.

Representing the direct and inverse Park Transform matrices from (2.1) and (2.2) as $T(t)$ and $T^{-1}(t)$, the voltages and currents from (4.1) can be transformed from the *abc*-frame to the *dq*-frame:

$$\boldsymbol{v}_{out,abc}(t) = T^{-1}(t) \cdot \boldsymbol{v}_{out,dq}(t), \tag{4.2}$$

$$\boldsymbol{v}_{pcc,abc}(t) = T^{-1}(t) \cdot \boldsymbol{v}_{pcc,dq}(t), \tag{4.3}$$

$$\boldsymbol{i}_{conv,abc}(t) = T^{-1}(t) \cdot \boldsymbol{i}_{conv,dq}(t). \tag{4.4}$$

Omitting the time-domain indicator (t) for simplicity, this leads to:

$$T^{-1}\boldsymbol{v}_{out,dq} - T^{-1}\boldsymbol{v}_{pcc,dq} = R_f T^{-1}\boldsymbol{i}_{conv,dq} + L_f \frac{d\left(T^{-1}\boldsymbol{i}_{conv,dq}\right)}{dt}, \tag{4.5}$$

$$T^{-1}\boldsymbol{v}_{out,dq} - T^{-1}\boldsymbol{v}_{pcc,dq} = R_f T^{-1}\boldsymbol{i}_{conv,dq} + L_f T^{-1}\frac{d\boldsymbol{i}_{conv,dq}}{dt} + L_f \frac{dT^{-1}}{dt}\boldsymbol{i}_{conv,dq}. \tag{4.6}$$

Multiplying both sides by T and recognizing that the product of a matrix by its inverse results in the identity matrix, such as in $T \cdot T^{-1} = Id$ (represented as Id to avoid confusing it with uppercase current variables), it results in:

$$\boldsymbol{v}_{out,dq} - \boldsymbol{v}_{pcc,dq} = R_f i_{conv,dq} + L_f \frac{d\boldsymbol{i}_{conv,dq}}{dt} + L_f T \frac{dT^{-1}}{dt}\boldsymbol{i}_{conv,dq}. \tag{4.7}$$

Considering that $\theta = \omega t$, the transformation matrix Ω is calculated as:

$$\Omega = T\frac{dT^{-1}}{dt}, \tag{4.8}$$

$$= \frac{2}{3}\begin{bmatrix} \cos(\theta) & \cos(\theta - \frac{2\pi}{3}) & \cos(\theta + \frac{2\pi}{3}) \\ -\sin(\theta) & -\sin(\theta - \frac{2\pi}{3}) & -\sin(\theta + \frac{2\pi}{3}) \\ \frac{1}{2} & \frac{1}{2} & \frac{1}{2} \end{bmatrix} \cdot \frac{d}{dt}\begin{bmatrix} \cos(\theta) & -\sin(\theta) & 1 \\ \cos(\theta - \frac{2\pi}{3}) & -\sin(\theta - \frac{2\pi}{3}) & 1 \\ \cos(\theta + \frac{2\pi}{3}) & -\sin(\theta + \frac{2\pi}{3}) & 1 \end{bmatrix}, \tag{4.9}$$

$$= \frac{2}{3}\begin{bmatrix} \cos(\theta) & \cos(\theta - \frac{2\pi}{3}) & \cos(\theta + \frac{2\pi}{3}) \\ -\sin(\theta) & -\sin(\theta - \frac{2\pi}{3}) & -\sin(\theta + \frac{2\pi}{3}) \\ \frac{1}{2} & \frac{1}{2} & \frac{1}{2} \end{bmatrix} \cdot \begin{bmatrix} -\omega\sin(\theta) & -\omega\cos(\theta) & 0 \\ -\omega\sin(\theta - \frac{2\pi}{3}) & -\omega\cos(\theta - \frac{2\pi}{3}) & 0 \\ -\omega\sin(\theta + \frac{2\pi}{3}) & -\omega\cos(\theta + \frac{2\pi}{3}) & 0 \end{bmatrix}, \tag{4.10}$$

$$= \frac{2}{3}\begin{bmatrix} e_{1,1} & e_{1,2} & e_{1,3} \\ e_{2,1} & e_{2,2} & e_{2,3} \\ e_{3,1} & e_{3,2} & e_{3,3} \end{bmatrix}. \tag{4.11}$$

The individual elements of Ω are calculated as:

$$e_{1,1} = -\omega \left(\cos(\theta)\sin(\theta) + \cos(\theta - \frac{2\pi}{3})\sin(\theta - \frac{2\pi}{3}) + \cos(\theta + \frac{2\pi}{3})\sin(\theta + \frac{2\pi}{3}) \right), \tag{4.12}$$

$$= -\frac{\omega}{2} \left(\sin(2\theta) + \sin(2\theta - \frac{4\pi}{3}) + \sin(2\theta + \frac{4\pi}{3}) \right), \tag{4.13}$$

$$= 0, \tag{4.14}$$

$$e_{1,2} = -\omega \left(\cos^2(\theta) + \cos^2(\theta - \frac{2\pi}{3}) + \cos^2(\theta + \frac{2\pi}{3}) \right), \tag{4.15}$$

$$= -\frac{\omega}{2} \left(\cos(2\theta) + 1 + \cos(2\theta - \frac{4\pi}{3}) + 1 + \cos(2\theta + \frac{4\pi}{3}) + 1 \right), \tag{4.16}$$

$$= -\frac{3}{2}\omega, \tag{4.17}$$

$$e_{1,3} = 0, \tag{4.18}$$

$$e_{2,1} = \omega \left(\sin^2(\theta) + \sin^2(\theta - \frac{2\pi}{3}) + \sin^2(\theta + \frac{2\pi}{3}) \right), \tag{4.19}$$

$$= \frac{\omega}{2} \left(1 - \cos(2\theta) + 1 - \cos(2\theta - \frac{4\pi}{3}) + 1 - \cos(2\theta + \frac{4\pi}{3}) \right), \tag{4.20}$$

$$= \frac{3}{2}\omega, \tag{4.21}$$

$$e_{2,2} = -e_{1,1} = 0, \tag{4.22}$$

$$e_{2,3} = 0, \tag{4.23}$$

$$e_{3,1} = -\frac{\omega}{2} \left(\sin(\theta) + \sin(\theta - \frac{2\pi}{3}) + \sin(\theta + \frac{2\pi}{3}) \right), \tag{4.24}$$

$$= 0, \tag{4.25}$$

$$e_{3,2} = -\frac{\omega}{2} \left(\cos(\theta) + \cos(\theta - \frac{2\pi}{3}) + \cos(\theta + \frac{2\pi}{3}) \right), \tag{4.26}$$

$$= 0, \tag{4.27}$$

$$e_{3,3} = 0, \tag{4.28}$$

$$\Omega = \begin{bmatrix} 0 & -\omega & 0 \\ \omega & 0 & 0 \\ 0 & 0 & 0 \end{bmatrix}. \tag{4.29}$$

Transforming (4.7) to the frequency domain, and omitting the frequency domain indicator (s) for simplicity, the result is finally:

$$\boldsymbol{V}_{out,dq} - \boldsymbol{V}_{pcc,dq} = R_f \boldsymbol{I}_{conv,dq} + sL_f \boldsymbol{I}_{conv,dq} + L_f \Omega \boldsymbol{I}_{conv,dq}, \tag{4.30}$$

$$\begin{bmatrix} V_{out,d} \\ V_{out,q} \\ V_{out,0} \end{bmatrix} - \begin{bmatrix} V_{pcc,d} \\ V_{pcc,q} \\ V_{pcc,0} \end{bmatrix} = \begin{bmatrix} sL_f + R_f & -\omega L_f & 0 \\ \omega L_f & sL_f + R_f & 0 \\ 0 & 0 & sL_f + R_f \end{bmatrix} \begin{bmatrix} I_{conv,d} \\ I_{conv,q} \\ I_{conv,0} \end{bmatrix}, \tag{4.31}$$

$$I_{conv,d} = \frac{1}{sL_f + R_f} \left(V_{out,d} - V_{pcc,d} + \omega L_f I_{conv,q} \right), \tag{4.32}$$

$$I_{conv,q} = \frac{1}{sL_f + R_f} \left(V_{out,q} - V_{pcc,q} - \omega L_f I_{conv,d} \right). \tag{4.33}$$

The equivalent block diagram representation of the plant is shown in Figure 4.2.

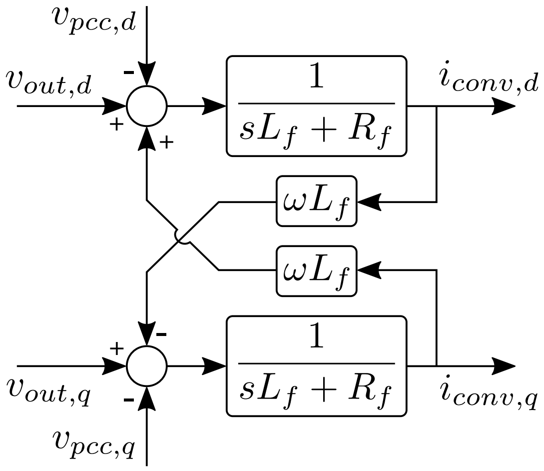

Figure 4.2: Block diagram representation of the plant.

4.2.2 Power Electronics Converter

Since the converter switches turn on and off, following a given switching scheme, the PEC cannot perfectly reproduce the reference output voltage calculated by the control system. This discrepancy can be modeled as a small delay in the system [69]. The output of the control system, $\boldsymbol{v}^*_{out}$, is delivered to the switching algorithm, which makes the necessary calculations and then sends the switching signals to the switches. Due to the sample-and-hold logic of the controller hardware and the delay in the switching algorithm calculations, the actual converter output voltage $\boldsymbol{v}_{out}$ does not instantaneously follow its reference value. This effect can be represented in the frequency domain as a first-order delay transfer function:

$$\boldsymbol{V}_{out,dq} = \frac{1}{sT_\Sigma + 1} \boldsymbol{V}^*_{out,dq}, \tag{4.34}$$

where T_Σ is the converter time delay. This is the effect of the physical converter itself, making the bridge between the control system and the physical plant. It can be represented by the equivalent block diagram shown in Figure 4.3.

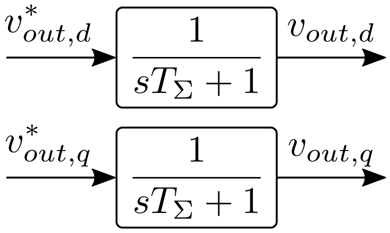

Figure 4.3: Block diagram representation of the converter delay.

4.2.3 Control System

4.2.3.1 Conventional Control System (GFL/GFM)

The block diagram representations of the GFL and GFM control systems were shown before in Figures 2.7 and 2.10. Usually, in GFM control systems, the outer voltage control loop is implemented with a larger time constant than the inner current control loop, consequently having a slower dynamic behavior. Therefore, for the following analysis, the voltage control loop of the GFM can be omitted, with the reference currents for the inner current control loop assumed constant. This way both the GFL and GFM control systems are assumed to be similar, containing only the current control loop. Figure 4.4 shows this equivalent block diagram. The Park transform blocks and the PLL (in the case of the GFL) are omitted from the diagram, which already shows the voltages and currents transformed to the dq-frame.

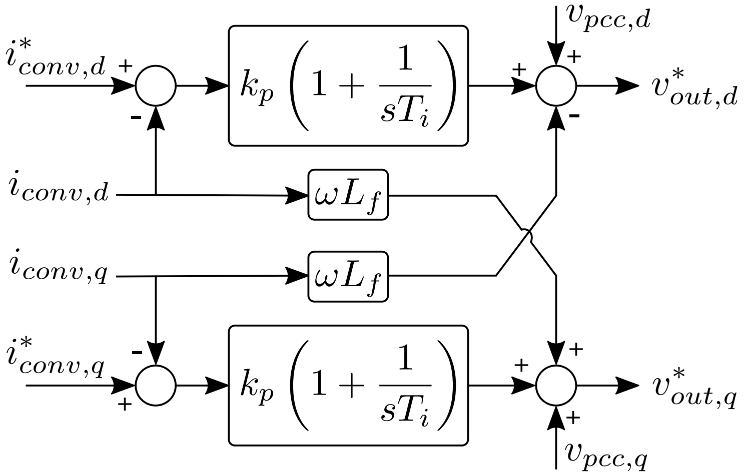

Figure 4.4: Block diagram representation of a conventional control system (GFL or GFM).

4.2.3.2 Hybrid Control System (HCC)

The first step for the analysis of the HCC control system is to convert its transfer functions into the dq-axis. Omitting the time-domain indicator (t) for conciseness, the equivalent instantaneous HCC voltage, as described previously in (3.35), is rewritten as:

$$\boldsymbol{v}_{HCC} = k_2\boldsymbol{v}_1 + k_1\boldsymbol{v}_2, \tag{4.35}$$

$$T\boldsymbol{v}_{HCC} = k_2T\boldsymbol{v}_1 + k_1T\boldsymbol{v}_2, \tag{4.36}$$

$$\boldsymbol{v}_{HCC,dq} = k_2\boldsymbol{v}_{1,dq} + k_1\boldsymbol{v}_{2,dq}, \tag{4.37}$$

$$\begin{bmatrix} v_{HCC,d} \\ v_{HCC,q} \\ v_{HCC,0} \end{bmatrix} = k_2 \begin{bmatrix} v_{1,d} \\ v_{1,q} \\ v_{1,0} \end{bmatrix} + k_1 \begin{bmatrix} v_{2,d} \\ v_{2,q} \\ v_{2,0} \end{bmatrix}. \tag{4.38}$$

The frequency domain representation, omitting the indicator (s), is then simply:

$$\boldsymbol{V}_{HCC,dq} = k_2\boldsymbol{V}_{1,dq} + k_1\boldsymbol{V}_{2,dq} \tag{4.39}$$

The back-calculation of current 1 is needed by the GFL-part of the HCC control system. First, the variables of *total resistance* and *total inductance* are defined just for conciseness in the following equations, as:

$$R_t = R_1 + R_2, \tag{4.40}$$

$$L_t = L_1 + L_2. \tag{4.41}$$

Then, (3.43) becomes, transforming to the dq-axis:

$$R_t\boldsymbol{i}_1 + L_t\frac{d\boldsymbol{i}_1}{dt} = \boldsymbol{v}_1 - \boldsymbol{v}_2 + R_2\boldsymbol{i}_{conv} + L_2\frac{d\boldsymbol{i}_{conv}}{dt}, \tag{4.42}$$

$$\begin{aligned} R_tT^{-1}\boldsymbol{i}_{1,dq} + L_t\frac{dT^{-1}\boldsymbol{i}_{1,dq}}{dt} &= T^{-1}\boldsymbol{v}_{1,dq} - T^{-1}\boldsymbol{v}_{2,dq} + R_2T^{-1}\boldsymbol{i}_{conv,dq} + \\ &+ L_2\frac{dT^{-1}\boldsymbol{i}_{conv,dq}}{dt}. \end{aligned} \tag{4.43}$$

Multiplying both sides by the Park transform matrix $T(t)$ results in:

$$\begin{aligned} R_t\boldsymbol{i}_{1,dq} + L_t\frac{d\boldsymbol{i}_{1,dq}}{dt} + L_tT\frac{dT^{-1}}{dt}\boldsymbol{i}_{1,dq} &= \boldsymbol{v}_{1,dq} - \boldsymbol{v}_{2,dq} + R_2\boldsymbol{i}_{conv,dq} + \\ &+ L_2\frac{d\boldsymbol{i}_{conv,dq}}{dt} + L_2T\frac{dT^{-1}}{dt}\boldsymbol{i}_{conv,dq}, \end{aligned} \tag{4.44}$$

$$R_t\boldsymbol{i}_{1,dq} + L_t\frac{d\boldsymbol{i}_{1,dq}}{dt} + L_t\Omega\boldsymbol{i}_{1,dq} = \boldsymbol{v}_{1,dq} - \boldsymbol{v}_{2,dq} + R_2\boldsymbol{i}_{conv,dq} + L_2\frac{d\boldsymbol{i}_{conv,dq}}{dt} + \\ + L_2\Omega\boldsymbol{i}_{conv,dq}. \tag{4.45}$$

Transforming (4.45) to the frequency domain, it yields:

$$\begin{aligned} R_t\boldsymbol{I}_{1,dq} + sL_t\boldsymbol{I}_{1,dq} + L_t\Omega\boldsymbol{I}_{1,dq} &= \boldsymbol{V}_{1,dq} - \boldsymbol{V}_{2,dq} + R_2\boldsymbol{I}_{conv,dq} + \\ &\quad + sL_2\boldsymbol{I}_{conv,dq} + L_2\Omega\boldsymbol{I}_{conv,dq}, \qquad (4.46) \\ (sL_t + R_t)\boldsymbol{I}_{1,dq} &= \boldsymbol{V}_{1,dq} - \boldsymbol{V}_{2,dq} + (sL_2 + R_2)\boldsymbol{I}_{conv,dq} + \\ &\quad + L_t\Omega(k_2\boldsymbol{I}_{conv,dq} - \boldsymbol{I}_{1,dq}). \qquad (4.47) \end{aligned}$$

Since the HCC filter inductance value is chosen by the system designer according to the converter's switching characteristics, it makes sense to express the equations in terms of R_f instead of R_1, R_2 (similarly for the inductances). From (3.37) and (4.40):

$$\begin{aligned} R_t &= R_1 + R_2, & (4.48) \\ R_t &= \frac{R_f}{k_2} + \frac{R_f}{k_1}, & (4.49) \\ R_t &= \frac{(k_1 + k_2)R_f}{k_1 k_2}, & (4.50) \\ R_t &= \frac{R_f}{k_1 k_2}. & (4.51) \end{aligned}$$

The same logic is applied to the total inductance from (3.38) and (4.41), leading to:

$$L_t = \frac{L_f}{k_1 k_2}. \tag{4.52}$$

Converting (4.47) to matrix notation, the result is:

$$\begin{bmatrix} I_{1,d} \\ I_{1,q} \\ I_{1,0} \end{bmatrix} = \frac{1}{sL_t + R_t}\begin{bmatrix} V_{1,d} - V_{2,d} \\ V_{1,q} - V_{2,q} \\ V_{1,0} - V_{2,0} \end{bmatrix} + k_2\begin{bmatrix} I_{conv,d} \\ I_{conv,q} \\ I_{conv,0} \end{bmatrix} + \\ + \frac{1}{sL_t + R_t}\begin{bmatrix} 0 & -\omega L_t & 0 \\ \omega L_t & 0 & 0 \\ 0 & 0 & 0 \end{bmatrix}\begin{bmatrix} k_2 I_{conv,d} - I_{1,d} \\ k_2 I_{conv,q} - I_{1,q} \\ k_2 I_{conv,0} - I_{1,0} \end{bmatrix}, \tag{4.53}$$

$$I_{1,d} = \frac{k_1 k_2}{sL_f + R_f}(V_{1,d} - V_{2,d}) + k_2 I_{conv,d} - \frac{\omega L_f}{sL_f + R_f}(k_2 I_{conv,q} - I_{1,q}), \tag{4.54}$$

$$I_{1,q} = \frac{k_1 k_2}{sL_f + R_f}(V_{1,q} - V_{2,q}) + k_2 I_{conv,q} + \frac{\omega L_f}{sL_f + R_f}(k_2 I_{conv,d} - I_{1,d}). \tag{4.55}$$

Then, the same calculations must be done for the GFM-part of the HCC control system and current 2. From (3.41), transforming to dq-coordinates, it yields:

$$\boldsymbol{I}_2 = \boldsymbol{I}_{conv} - \boldsymbol{I}_1, \tag{4.56}$$

$$\boldsymbol{I}_{2,dq} = \boldsymbol{I}_{conv,dq} - \boldsymbol{I}_{1,dq}. \tag{4.57}$$

It is possible to rewrite (4.47) as:

$$(sL_t + R_t)\boldsymbol{I}_{1,dq} + \Omega L_t \boldsymbol{I}_{1,dq} = \boldsymbol{V}_{1,dq} - \boldsymbol{V}_{2,dq} + (sL_2 + R_2)\boldsymbol{I}_{conv,dq} + L_t \Omega k_2 \boldsymbol{I}_{conv,dq}. \tag{4.58}$$

Applying (4.57) in (4.58), it yields:

$$\begin{aligned}(sL_t + R_t)\boldsymbol{I}_{conv,dq} + \Omega L_t \boldsymbol{I}_{conv,dq} - (sL_t + R_t)\boldsymbol{I}_{2,dq} - \Omega L_t \boldsymbol{I}_{2,dq} = \\ = \boldsymbol{V}_{1,dq} - \boldsymbol{V}_{2,dq} + (sL_2 + R_2)\boldsymbol{I}_{conv,dq} + L_t \Omega k_2 \boldsymbol{I}_{conv,dq},\end{aligned} \tag{4.59}$$

$$\begin{aligned}(sL_t + R_t)\boldsymbol{I}_{2,dq} + \Omega L_t \boldsymbol{I}_{2,dq} = \boldsymbol{V}_{2,dq} - \boldsymbol{V}_{1,dq} + (sL_1 + R_1)\boldsymbol{I}_{conv,dq} + \\ + L_t \Omega k_1 \boldsymbol{I}_{conv,dq}\end{aligned} \tag{4.60}$$

In matrix representation, the result is:

$$\begin{aligned}\begin{bmatrix} I_{2,d} \\ I_{2,q} \\ I_{2,0} \end{bmatrix} = \frac{1}{sL_t + R_t}\begin{bmatrix} V_{2,d} - V_{1,d} \\ V_{2,q} - V_{1,q} \\ V_{2,0} - V_{1,0} \end{bmatrix} + k_1 \begin{bmatrix} I_{conv,d} \\ I_{conv,q} \\ I_{conv,0} \end{bmatrix} + \\ + \frac{1}{sL_t + R_t}\begin{bmatrix} 0 & -\omega L_t & 0 \\ \omega L_t & 0 & 0 \\ 0 & 0 & 0 \end{bmatrix}\begin{bmatrix} k_1 I_{conv,d} - I_{2,d} \\ k_2 I_{conv,q} - I_{2,q} \\ k_2 I_{conv,0} - I_{2,0} \end{bmatrix},\end{aligned} \tag{4.61}$$

$$I_{2,d} = \frac{k_1 k_2}{sL_f + R_f}(V_{2,d} - V_{1,d}) + k_1 I_{conv,d} - \frac{\omega L_f}{sL_f + R_f}(k_1 I_{conv,q} - I_{2,q}), \tag{4.62}$$

$$I_{2,q} = \frac{k_1 k_2}{sL_f + R_f}(V_{2,q} - V_{1,q}) + k_1 I_{conv,q} + \frac{\omega L_f}{sL_f + R_f}(k_1 I_{conv,d} - I_{2,d}). \tag{4.63}$$

The current loop of the GFL-part of the HCC control system is similar to a conventional control system, as shown in Figure 4.4. As mentioned before, the voltage loop of the GFM-part is neglected due to its slower dynamics, and therefore it can also be represented in a similar fashion. Aggregating the developed transfer functions, the equivalent block diagram of the HCC control system is shown in Figure 4.5.

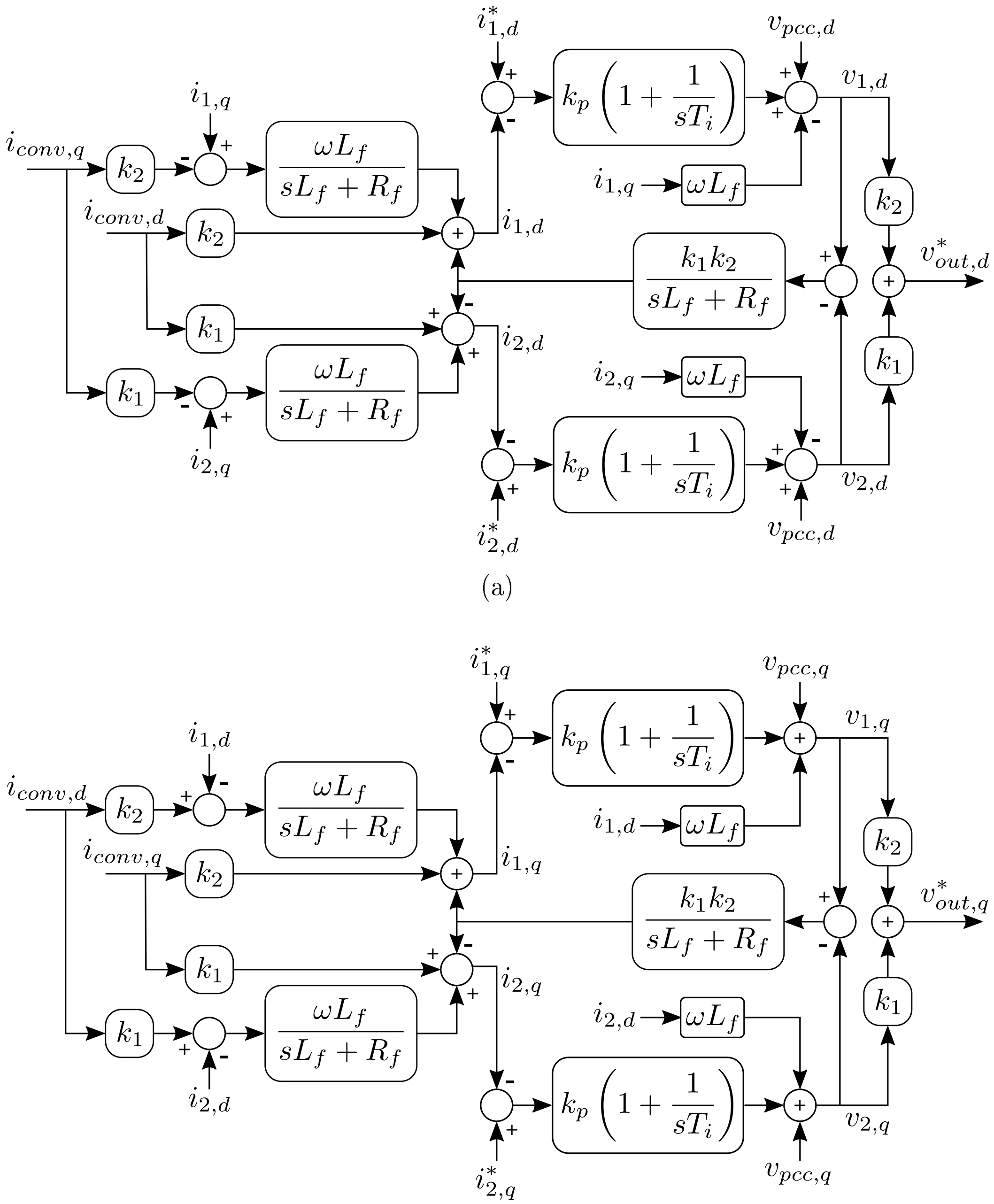

Figure 4.5: Block diagram representation of the HCC control system for the d- and q-axes.

4.2.4 Aggregation and Simplification of the Transfer Functions

The transfer functions for the plant, the converter and the two different control systems were developed. The next step is to aggregate and simplify them, in order to reach the equivalent open-loop transfer function TF_{open}, that is used in the stability analysis itself.

4.2.4.1 Conventional Control System (GFL/GFM)

Figure 4.6 shows the complete block diagram for a system comprising the plant, the converter and a conventional control system (which can be either a GFL or GFM). The Park transform blocks and the PLL (in the case of the GFL) are omitted from the diagram, as it already shows the voltages and currents transformed to the dq-frame.

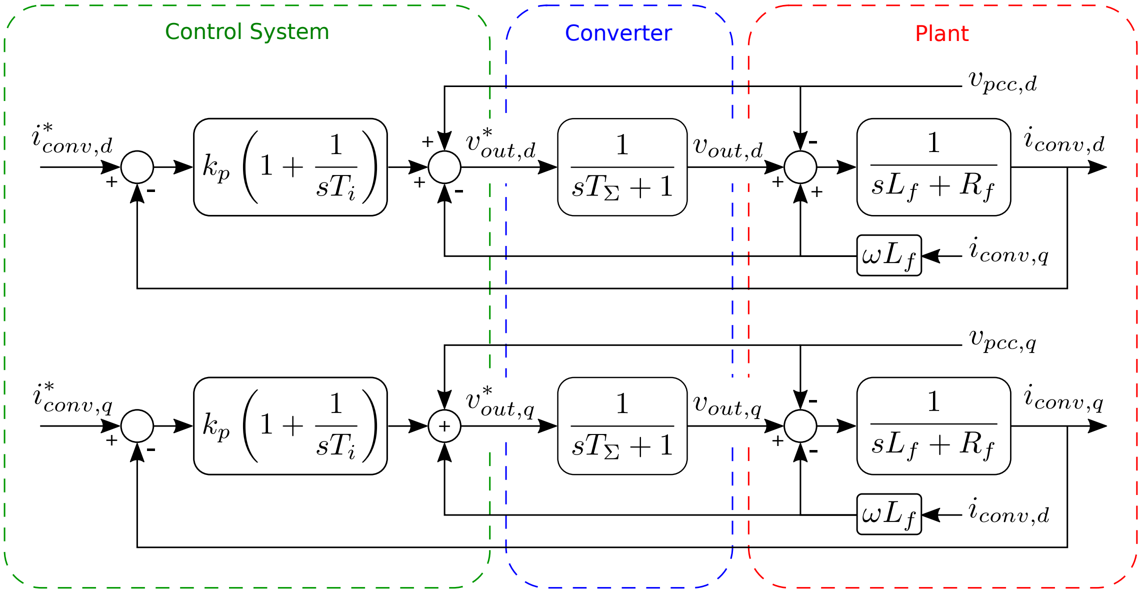

Figure 4.6: Block diagram representation of a system including the plant, a converter and a conventional control system (GFL or GFM).

It is possible to simplify the block diagram in Figure 4.6, making the calculations that follow easier. First, based on the superposition principle, it is a common practice to ignore external inputs when analyzing the stability of a system, treating them as disturbances that can be neglected. This means, for example, neglecting the inputs of v_d and i_q when analyzing the stability of the $i^*_{conv,d}$ loop, and vice-versa for the q-axis system components [69].

Besides that, the equations get further simplified by designing the appropriate gains for the PI controller. Its transfer function is described in (2.5), and it has two parameters: the proportional gain and the integral time constant. If the integral time constant is chosen appropriately to match the plant's resistance (R_f) and inductance (L_f), it leads to one pole of the equivalent transfer function getting canceled. For this end, the integral time constant is designed as:

$$T_i = \frac{L_f}{R_f}, \tag{4.64}$$

$$PI(s) = k_p \frac{sL_f + R_f}{L_f}. \tag{4.65}$$

With these approaches, the transfer functions showed in Figure 4.6 can be aggregated as:

$$TF_{open}(s) = k_p \frac{sL_f + R_f}{sL_f} \cdot \frac{1}{sT_\Sigma + 1} \cdot \frac{1}{sL_f + R_f}, \tag{4.66}$$

$$= \frac{k_p}{s^2 L_f T_\Sigma + sL_f}. \tag{4.67}$$

The simplified block diagram of the entire system, showing the equivalent open-loop transfer function, is shown in Figure 4.7.

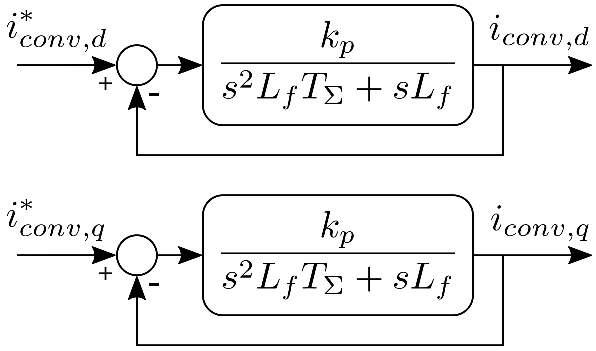

Figure 4.7: Equivalent open-loop representation of the system with a conventional control system (GFL or GFM).

4.2.4.2 Hybrid Control Converter

The complete block diagram for a system comprising the plant, the converter and the HCC control system is shown in Figure 4.8 (only the d-axis is shown, for conciseness). The Park transform blocks and the PLL (in the case of the GFL-part of the HCC) are once again omitted from the diagram, as it already shows the voltages and currents transformed to the *dq*-frame.

Similarly to the previous case, external inputs are neglected in the following analysis. Applying the same procedure to design the PI controllers, for both the

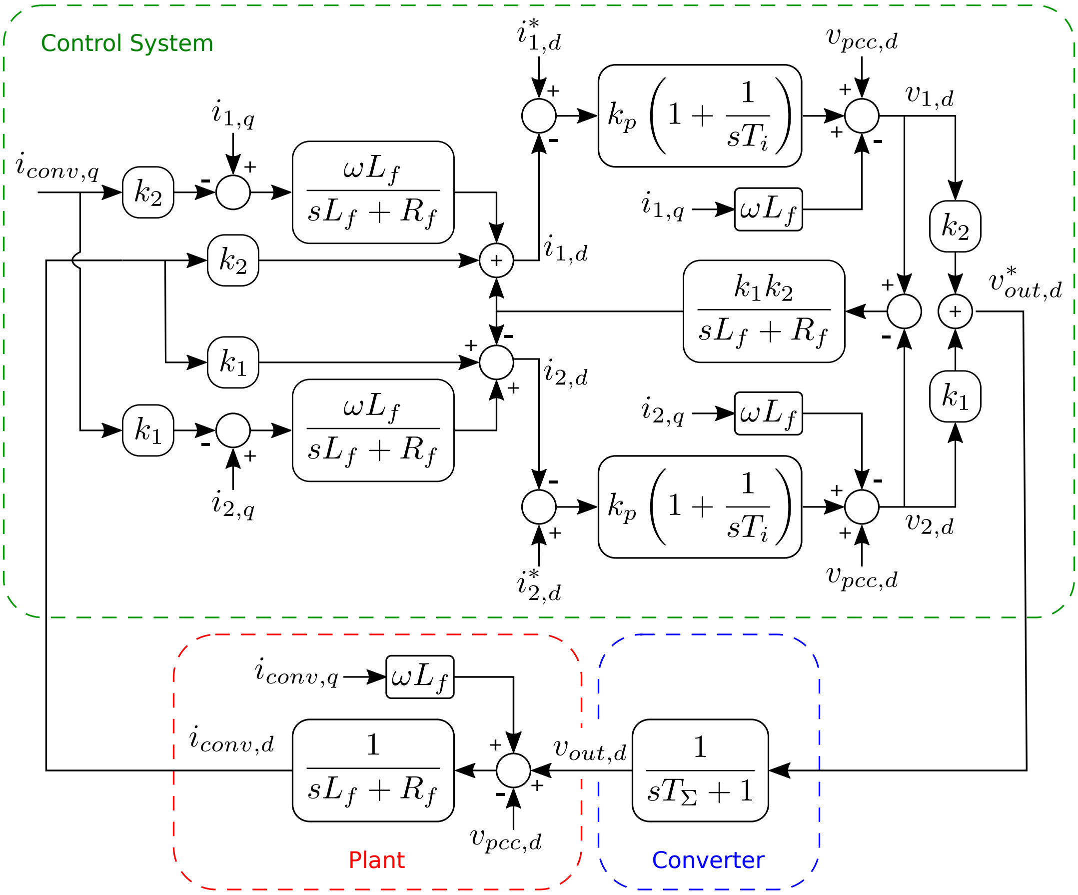

Figure 4.8: Block diagram representation of a system including the plant, a converter and an HCC control system (showing only the d-axis for conciseness).

GFL-part and the GFM-part of the HCC control system, it results in:

$$T_{i,1} = \frac{L_1}{R_1} = \frac{L_f}{R_f}, \tag{4.68}$$

$$T_{i,2} = \frac{L_2}{R_2} = \frac{L_f}{R_f}, \tag{4.69}$$

$$PI_1(s) = k_{p,1}\frac{sL_f + R_f}{sL_f}, \tag{4.70}$$

$$PI_2(s) = k_{p,2}\frac{sL_f + R_f}{sL_f}. \tag{4.71}$$

With these factors, the block diagrams for both the d- and q-axes become similar, therefore the equations that follow represent both axes. Since it is a more complex block diagram than with the conventional control system, techniques to reduce it must be applied sequentially. First, considering the loop related to $i^*_{1,d}$, the four major steps in the block diagram simplification are shown in Figure 4.9.

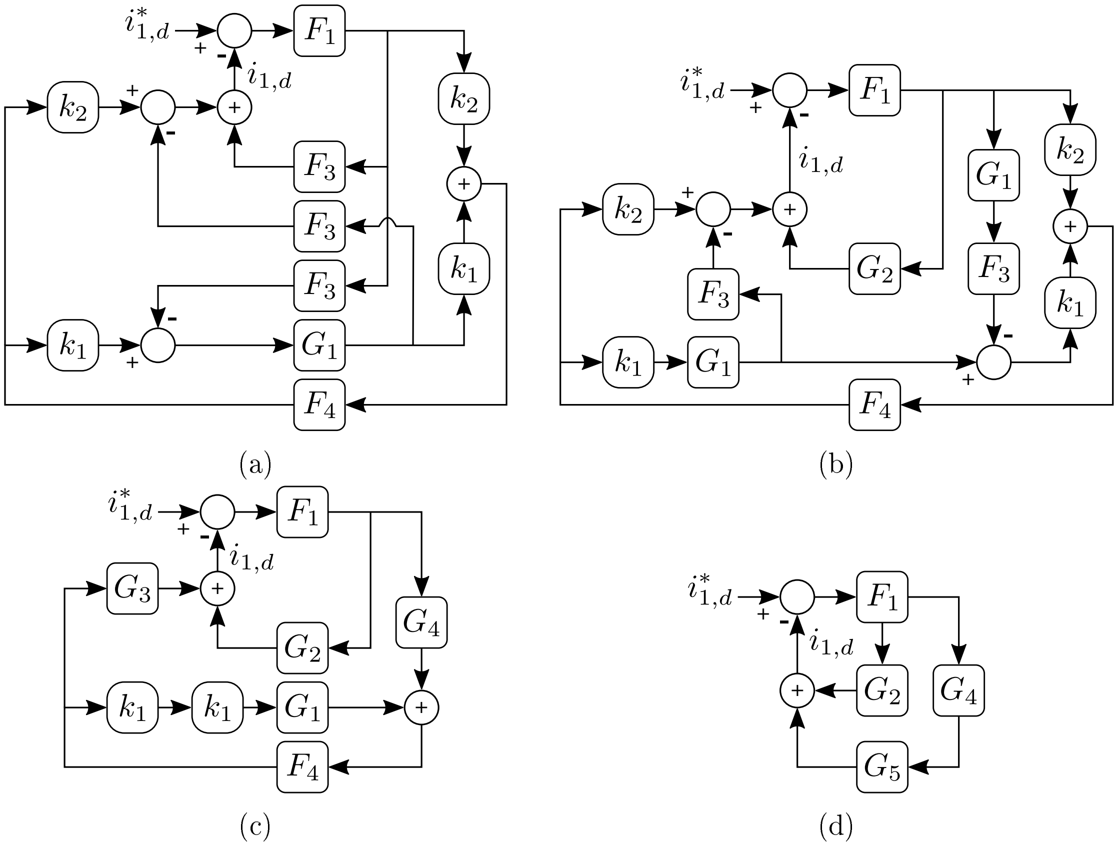

Figure 4.9: The major steps taken in the simplification of the block diagram, considering the system with the HCC control system (showing only the d-axis for conciseness).

For simplicity, the transfer functions shown in Figure 4.8 are represented as:

$$F_1 = k_{p,1}\frac{sL_f + R_f}{L_f}, \tag{4.72}$$

$$F_2 = k_{p,2}\frac{sL_f + R_f}{L_f}, \tag{4.73}$$

$$F_3 = \frac{k_1 k_2}{sL_f + R_f}, \tag{4.74}$$

$$F_4 = \frac{1}{sL_f + R_f} \cdot \frac{1}{sT_\Sigma + 1}. \tag{4.75}$$

The intermediate transfer functions that appear during the simplification process of the block diagram, as shown in Figure 4.9, are:

$$G_1 = -\frac{F_2}{1 + F_2 F_3} = -k_{p,2}\frac{sL_f + R_f}{sL_f + k_{p,2}k_1k_2}, \tag{4.76}$$

$$G_2 = F_3 + G_1 F_3^2 = \frac{sL_f k_1 k_2}{(sL_f + R_f)(sL_f + k_{p,2}k_1k_2)}, \tag{4.77}$$

$$G_3 = G_4 = k_2 - k_1 F_3 G_1 = \frac{sL_f k_2 + k_{p,2} k_1 k_2}{sL_f + k_{p,2} k_1 k_2}, \tag{4.78}$$

$$G_5 = \frac{G_3 F_4}{1 - k_1^2 G_1 F_4} = \frac{1}{sL_f + R_f} \cdot \frac{sL_f k_2 + k_{p,2} k_1 k_2}{(sL_f + k_{p,2} k_1 k_2)(sT_\Sigma + 1) + k_{p,2} k_1^2}. \tag{4.79}$$

In the end, the equivalent open-loop transfer function for the HCC control system, considering the d-axis current of the GFL-part as reference, is described as:

$$TF_{open,hcc} = F_1 \left(G_2 + G_4 \cdot G_5 \right), \tag{4.80}$$

$$TF_{open,hcc} = \frac{k_{p,1} k_2}{sL_f} \cdot \frac{s^2 L_f T_\Sigma k_1 + sL_f + k_{p,2} k_1}{s^2 L_f T_\Sigma + s(L_f + T_\Sigma k_{p,2} k_1 k_2) + k_{p,2} k_1}. \tag{4.81}$$

Results for the q-axis are similar, since they derive from a similar block diagram. For the reference currents of the GFM-part, results are the same but exchanging subscripts 1 and 2 in the variables. Figure 4.10 shows the equivalent open-loop transfer functions of the system.

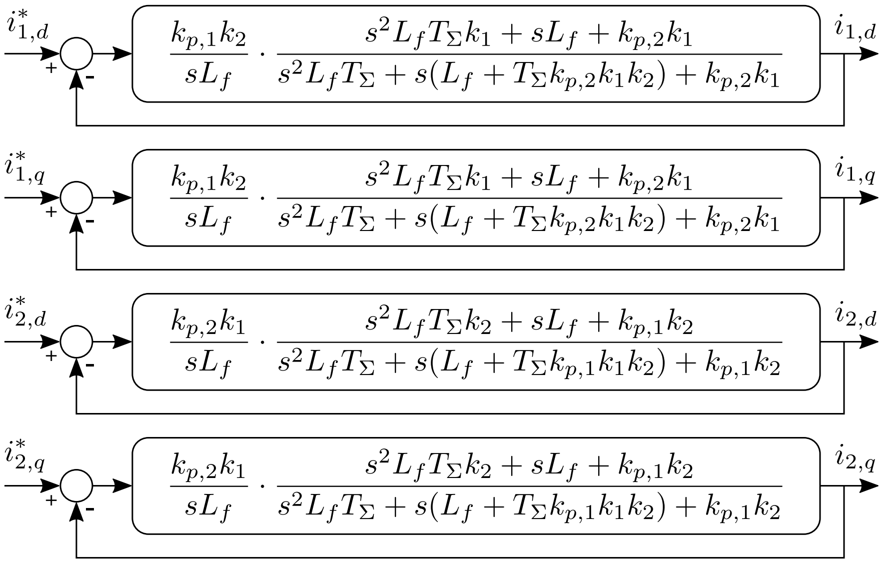

Figure 4.10: Equivalent open-loop representation of the system with an HCC control system.

4.2.5 Validity Check

A validity check can be performed with the equations developed thus far. An analysis similar to the one presented in section 3.5.1 is done, considering that one of the two converters that the HCC is emulating, converter 2, is not connected to the PCC, so $R_2 \rightarrow \infty$ and $L_2 \rightarrow \infty$. As demonstrated in section 3.5.1, this scenario results in:

$$\lim_{R_2 \to \infty} k_2 = 1, \tag{4.82}$$

$$\lim_{R_2 \to \infty} k_1 = 0, \tag{4.83}$$

$$\lim_{R_2 \to \infty} R_1 = R_f, \tag{4.84}$$

$$\lim_{R_2 \to \infty} L_1 = L_f, \tag{4.85}$$

$$\lim_{R_2 \to \infty} \boldsymbol{V}_{HCC} = \boldsymbol{V}_1, \tag{4.86}$$

$$\lim_{R_2 \to \infty} \boldsymbol{I}_1 = \boldsymbol{I}_{conv}, \tag{4.87}$$

$$\lim_{R_2 \to \infty} \boldsymbol{I}_2 = 0. \tag{4.88}$$

Considering these values, the open-loop transfer function for the system with the HCC control system, described in (4.81), becomes:

$$\lim_{R_2 \to \infty} TF_{HCC,open}(s) = \frac{k_{p,1}}{s^2 L_f T_\Sigma + s L_f}. \tag{4.89}$$

Comparing (4.89) with (4.67), the equivalent counterpart from the system with the conventional control system, it can be seen that they are perfect equivalents. Similarly to what was concluded in section 3.5.1, this means that, if the HCC is emulating a system where only one converter is connected to the grid, it presents the exact behavior of a simple system consisting of a single converter with a conventional control system, confirming the validity of the developed transfer functions.

The transfer functions can also be validated by simulation. To do this, two simulations are set up, as shown in Figure 4.11. The first is similar to the ones described in previous chapters. It is a transient time-domain electrical simulation, consisting on electrical components (such as voltage sources, resistances, inductances) and on the HCC control system. The second one is a direct simulation of the analytical model based on the developed transfer functions, that were shown in Figure 4.8. It contains no electrical components, only mathematical ones. Both cases, ultimately, simulate the same system, which consists of a converter (the HCC) connected to an ideal voltage source.

The simulation starts with the converter having zero active and reactive power. At simulation time $t = 0.3s$, the GFL-part of the HCC control system receives a step in its reference active power, going from 0 to 5.0 MW. Its reference current $i^*_{1,dq}$ is calculated from the value of the reference active power, as shown before in Figure 2.7. Then, at simulation time $t = 0.4s$, the GFM-part of the HCC control system receives a step in its reference active power, going from 0 to 5.0 MW. Its reference

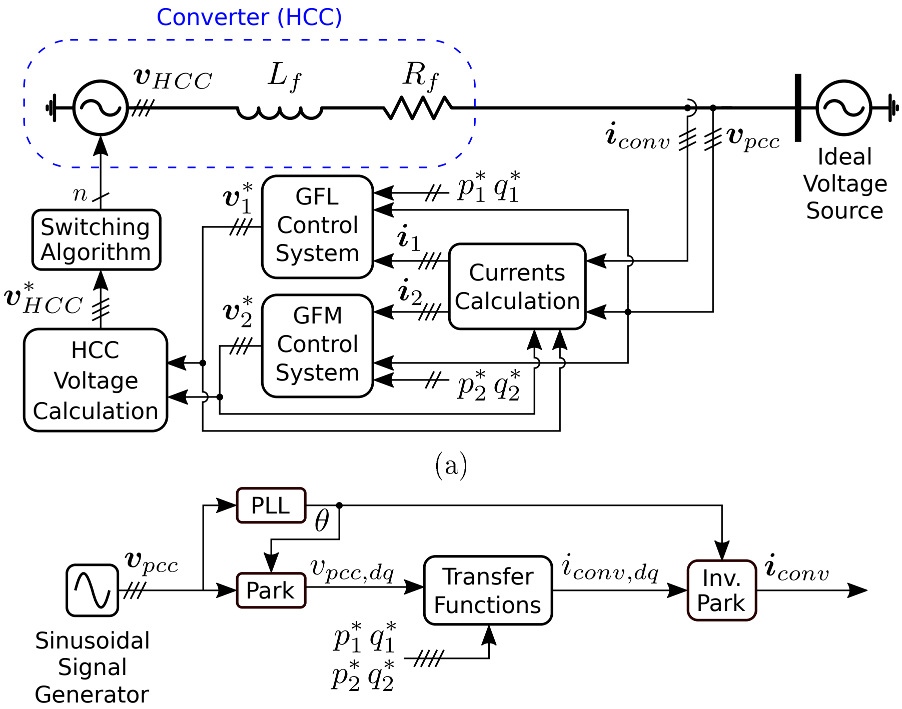

(a)

(b)

Figure 4.11: Simulation systems set up to validate the developed transfer functions: (a) electrical time-domain simulation and (b) analytical model-based simulation.

current is calculated similarly. In the end, the converter provides a total of 10.0 MW to the ideal voltage source. This behavior is shown in Figure 4.12.

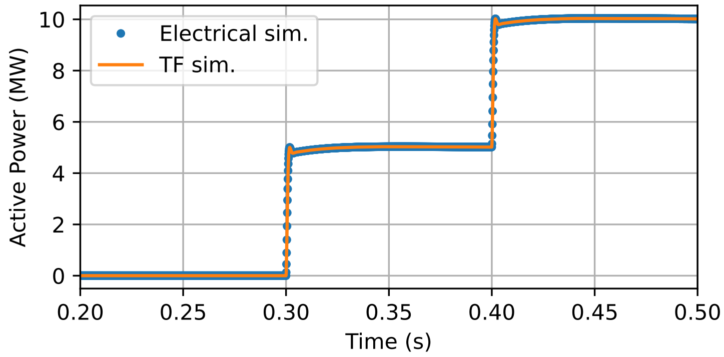

Figure 4.12: Converter output power, for both simulations performed to assess the validation of the developed transfer functions.

It can be seen that the output power of both simulations match. This means that the developed transfer functions can accurately describe the behavior of the HCC, considering the assumptions described in the beginning of this chapter.

4.3 Root Locus

One of the ways to evaluate the stability of a system is with the Root Locus technique. It is a graphical representation of a closed-loop system in the real-imaginary plane, showing the different locations of the poles when a given parameter (such as a controller gain) is varied [64, 70]. Regarding the stability criterion, poles located in the left half-plane are equivalent to time-domain components (of the closed-loop transfer function) with an exponential decay, and are therefore stable. On the other hand, poles on the right half-plane lead to an exponential increase with time, being unstable. The root locus plot allows for a visual inspection of the poles location and trajectories; if they are always on the left half-plane, the analyzed system is stable. The trajectory of the closed-loop system's poles, in the root locus plot, starts at the location of the open-loop system's poles, and migrates towards the location of the open-loop system's zeros. The root locus plot is a valuable technique, especially for systems of higher polynomial orders, that can be used both to assess the system stability or to design the control system gains to yield a desired performance criteria.

The impedance values used in the following analysis are the same ones used in previous simulations, described in Table 2.1. For the HCC control system, it is assumed that $k_{p,1} = k_{p,2} = k_p$.

The root locus plots for the systems with the conventional and with the HCC control systems are shown in Figures 4.13 and 4.14. For the case with the conventional control system, the pole trajectories meet in the real axis, and move vertically towards infinity. For the case with the HCC, there are two zeros and three poles, leading to a root locus plot with a different shape. One of the poles is very close to one of the zeros, almost canceling it. This way, the shape of the root locus resembles that of a second-order system with a single zero.

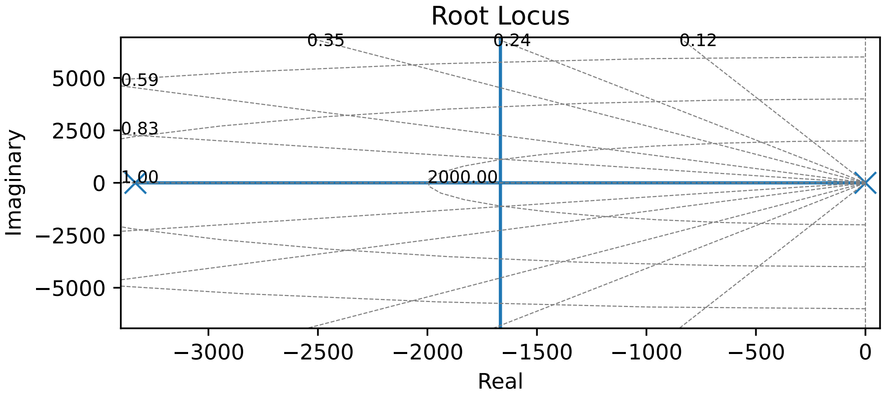

Figure 4.13: Root locus plot for the system with a conventional converter (GFL/GFM).

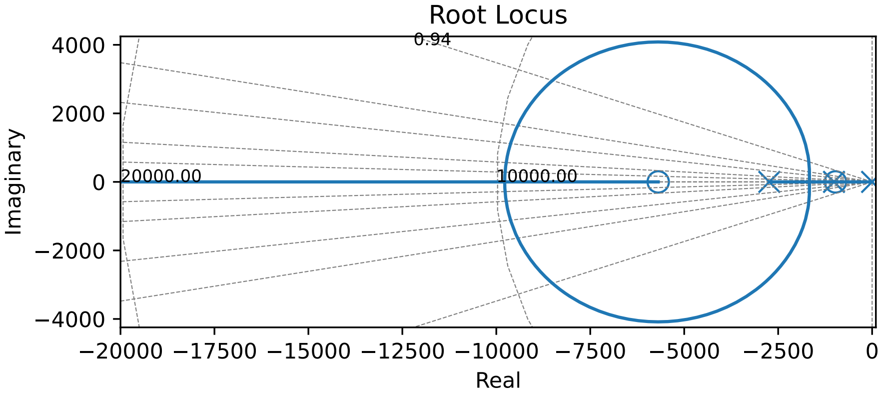

Figure 4.14: Root locus plot for the system with an HCC.

Both cases do not contain any poles in the right half-plane and the pole trajectories never cross the imaginary axis, even when any of the parameters (such as L_f, R_f, T_Σ...) are varied. This means that both control systems are stable for any value of the PI controller proportional gain k_p, or $k_{p,1}$ and $k_{p,2}$, for the HCC control system.

Since the transfer functions are different between the case with a conventional control system and the case with the HCC, the system may present different transient behavior in terms of overshoot, rise time, settling time, or any other performance index. The gain should be appropriately designed and analyzed in both cases to achieve the desired transient behavior. Most importantly, this analysis shows that the HCC control system is stable, similarly to conventional converter control systems, according to the root locus criterion.

4.4 Bode Plots

The best way to evaluate a system's frequency response, and also assess its stability margins, is by means of the Bode plots [64, 71]. They consist on two parts: the magnitude and the phase plots, representing the change in magnitude and shift in phase that a given system applies to a sinusoidal input. Since Linear Time-Invariant (LTI) systems do not change the frequency of a given sinusoidal input, they may only apply a gain to the amplitude and/or an offset to the phase of that signal.

The evaluation of stability using Bode plots is based on the open-loop transfer function. The closed loop form of a given open-loop transfer function, such as the ones shown in Figures 4.7 and 4.10, is:

$$TF_{closed}(s) = \frac{TF_{open}(s)}{1 + TF_{open}(s)}. \tag{4.90}$$

The closed-loop system is unstable if the denominator is equal to to zero, as in:

$$1 + TF_{open}(s) = 0, \tag{4.91}$$

$$TF_{open}(s) = -1. \tag{4.92}$$

The open-loop transfer function can be described in phasor representation, being represented by two values: its amplitude and phase. This way, (4.92) can be interpreted as:

$$|TF_{open}(j\omega)| = 1, \tag{4.93}$$

$$\arg\left(TF_{open}(j\omega)\right) = 180^o. \tag{4.94}$$

The system is unstable when the frequency (ω) of the input signal leads to, simultaneously, an amplitude of 1 and a phase of 180^o in the open-loop transfer function. To assess how close a system is from becoming unstable, the concept of Margins of Stability are introduced with the Bode plots. They represent the variations that would need to occur in the magnitude or phase of $TF_{open}(s)$ in order to simultaneously reach the critical values of amplitude and phase. Larger margins of stability mean that the system is less prone to becoming unstable, even if the plant or control system transfer functions change over time due to some physical phenomena, or due to errors in the modeling step. The margins of stability are defined as:

- Gain Margin: the amount of gain (represented as a vertical shift in the magnitude plot) needed to make the magnitude plot cross the 0 dB mark at the same frequency where the phase is 180^o; and

- Phase Margin: the amount of phase shift (represented as a vertical shift in the phase plot) needed to make the phase plot cross the 180^o mark at the same frequency where the magnitude is 0 dB.

The same values of impedances and control parameters used in the previous section are employed here. Figures 4.15 and 4.16 show the Bode plots for the system with a conventional and with the HCC control system, for different values of the control parameter k_p. In both cases, the phase curve never reaches 180^o, leading to an infinite gain margin. Nevertheless, Figure 4.15 shows that, for the conventional control system, as k_p increases, the point where the magnitude curve crosses the 0 dB mark is shifted to the right, where the phase curve asymptotically approaches 180^o. This results in a diminishing phase margin (represented as black bold vertical lines in the phase plot), making the system more prone to instability if the gain is very high. For the system with the HCC control system, an increase in gain also leads to right-shift of the point where the magnitude curve crosses the 0 dB mark. Although the phase curve does not asymptotically go towards 180^o, an increase in the gain leads to an oscillation in the curve, reducing the phase margin.

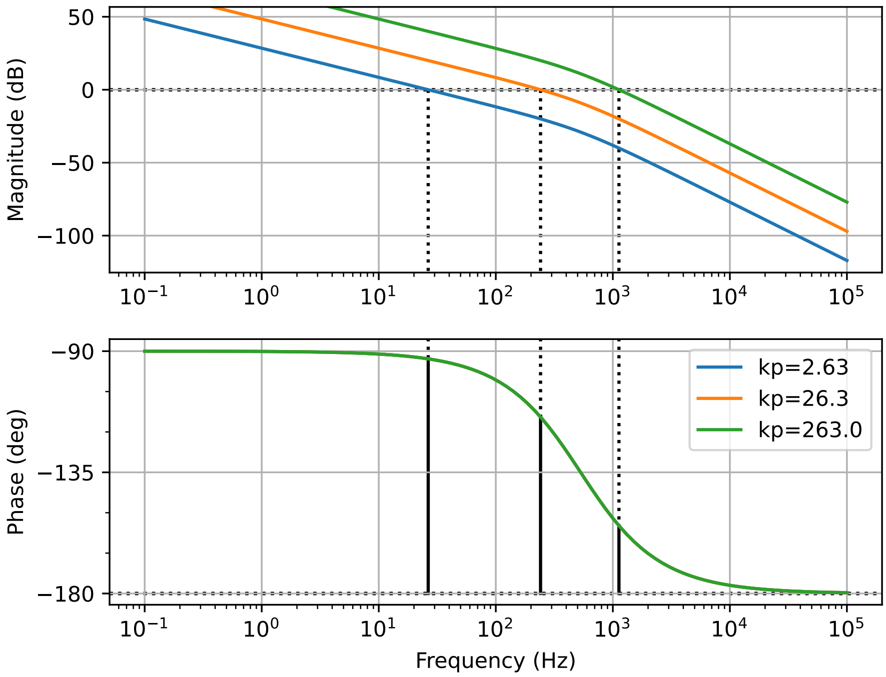

Figure 4.15: Bode plots for the system with a conventional converter (GFL/GFM).

This comparison showed that both cases represent stable systems according to the Bode plots criterion. They have infinite gain margin and a diminishing phase margin as the PI-controller proportional gain increases.

4.5 Partial Conclusion

This chapter discussed the stability of the HCC control system, comparing it with conventional converter control systems such as GFL or GFM. Initially, the control system, converter delay and physical plant were described as transfer functions, considering the conventional and the HCC control systems. The equivalent open-loop transfer functions were calculated. A validity check was performed to prove that the equations developed for the HCC match those developed for the conventional control system in the particular case where the HCC would be mimicking a single

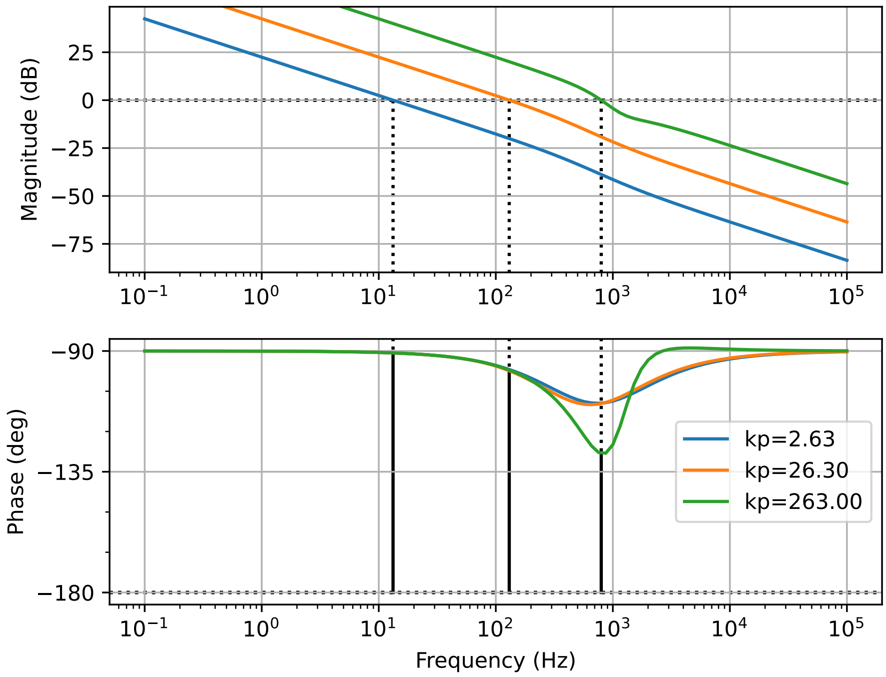

Figure 4.16: Bode plots for the system with an HCC.

converter, increasing the confidence in the developed set of equations.

Two different analyses were done, using Root Locus plots and Bode plots. The Root Locus analysis shows that, similarly to conventional control systems, the HCC does not present any poles in the right half of the real-imaginary plane. Moreover, the pole trajectories never cross the imaginary axis for any value of the PI-controller proportional gain k_p. The poles also do not cross to the right half-plane with variations of the other system parameters. The Bode plots analysis showed that both the conventional control system and the HCC have an infinite gain margin, and a diminishing phase margin as the proportional gain increases, but are stable nonetheless.

These results show that the HCC is a stable control system for the analyzed cases, similarly to a conventional GFL/GFM control system. The extra transfer functions present in the HCC mathematical model do not bring instability to the control system, making it a viable option for converter control.

Chapter 5

Robustness Analysis

This chapter presents the concept of robustness, discussing common simplifications of the physical system employed when designing a converter control system. Different factors that increase model uncertainty are presented and analyzed, both from the point of view of a conventional converter and from that of the HCC.

5.1 Definition

In any kind of control analysis, it is necessary to model the control system itself and the physical system upon which the controller acts. The mathematical model is essentially a set of transfer functions that map inputs to outputs, describing the behavior of the real system it represents. If the mathematical models are a good enough representation of the real system, it is expected that the controller will work, fulfilling its intended purpose.

Nevertheless, mathematical models are always imperfect. It is impossible to represent mathematically, with perfect accuracy, the complete behavior of a system. For example, mechanical systems may have different, unknown behaviors for different ranges of mechanical frequency caused by rotating or vibration. They may also be affected by the tolerance of manufacturing processes, that always result in some size or weight variation in the equipment itself.

Electrical systems comprised of semiconductors include variations in the material composition, due to the manufacturing process, that are impossible to know and model. The electrical grid is also inherently dynamic and changes over time, as mentioned before [65–68]. During regular operation, some transmission lines may be open due to faults, transformers may be removed from the grid for maintenance, the levels of generation and demand vary constantly, making it essentially impossible to perfectly (and dynamically) model the grid state.

Besides that, usually the mathematical models include some simplifications in the analyzed physical phenomena. They may be employed simply because the way the physical system works is not known with great accuracy, or also to decrease computational complexity and actually enable the design of the control system following a specific technique or ruleset. The system may also undergo stochastic events that change its behavior over time, be them short-term (noise) or long-term (degradation).

All of these aspects can be categorized as model uncertainty. Overall, there are several unknowable factors that may affect the system on which a given control system acts, leading to increased uncertainty and increased deviation between the expected and the actual control system behavior. Considering those aspects in the control design, *a system is defined as robust if it is capable of meeting user-defined stability or performance requirements even in the presence of model and/or disturbance uncertainty* [64, 72]. This means that, even if the physical system (or the environment it works in) is not known perfectly, a robust controller still functions properly, according to some desired criteria.

One way to design such a controller is to not only meet, but exceed the requirements of stability or performance. This can be done by adding some margin so that, even if the performance is degraded due to model uncertainty, it will still meet the initial requirements. In the end, it stems from a cost-benefit analysis. More complex (and robust) control systems take more time and effort to be developed and tested, and may require more computational power or sensors with greater accuracy and less noise, resulting in increased cost. On the other hand, simpler control systems may just not be robust enough and lead to system failure depending on the level of uncertainty that it deals with.

The following sections analyze different ways in which the mathematical model of a converter may differ from the real system, either due to simplifications or to unknown parameters, comparing a conventional converter control system (GFL or GFM) to the proposed HCC.

5.2 Converter Delay

As mentioned in Chapter 4, any converter has an inherent delay between the reference output voltage and the actual voltage that appears at the converter's terminals. This is due mostly to the switching algorithm and to the controller clock rate, but it is also affected by the computational implementation of the controller that includes zero-order hold and other sampling techniques. Since the equivalent switching frequency of modern PECs is usually above 1 kHz, the converter delay tends to be lower than 1 ms in most cases.

Nevertheless, the delay may affect the stability of the converter control system, especially if it is unknown or poorly modeled. To assess the robustness related to variations in the converter delay and check the system stability, the Root Locus method is employed. Similarly to Section 4.3, both the conventional control system and the HCC are analyzed. The controller gains are designed according to the Technical Optimum technique [60], assuming a value of $T_\Sigma = 0.3ms$ [69], as:

$$k_p = \frac{L_f}{2T_\Sigma}. \tag{5.1}$$

The analysis that follows considers that the actual value of the converter delay T_Σ for the converter may be different than that. The controller essentially expects a given value of delay which is different than the actual value, leading to a mismatch between the expected and the real behavior of the system. Once gain, the electrical parameters described in Table 2.1 are employed, leading to $k_p = 26.3V/A$.

Figure 5.1 shows the Root Locus plot for the conventional converter control system, for different values of T_Σ. One of the system's poles stays at the origin, so the pole trajectories never cross the imaginary axis. Nevertheless, as the delay increases, the pole trajectories move closer to the imaginary axis, since the second pole of the system also moves this way. This means that the system becomes increasingly underdamped, with higher overshoot and settling times.

This behavior is also reflected in the Bode plots, as shown in Figure 5.2. It can be seen that, as the delay increases, the phase margin, denoted by the bold vertical lines, is reduced. The system appears to have an infinite gain margin because the phase curve only asymptotically tends towards 180^o, but if the phase curve of the actual system, considering some kind of uncertainty or variation, is shifted slightly down, then it would reach the 180^o mark. The curve corresponding to the higher delay would cross that limit at a lower frequency, resulting in a gain margin that is no longer infinite, and smaller than in the cases with a smaller delay.

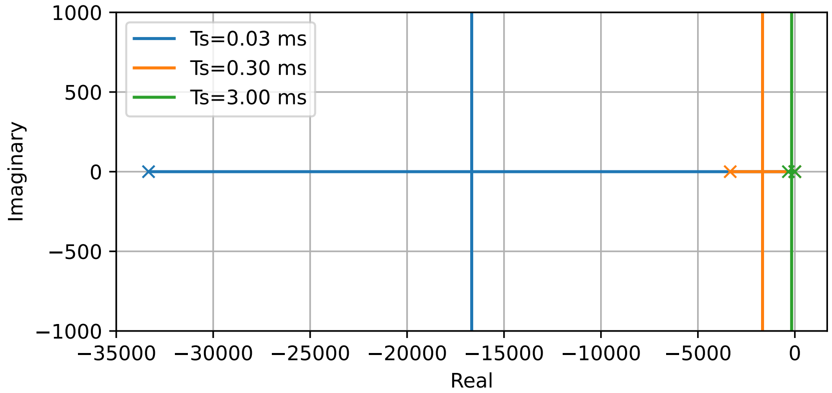

Figure 5.1: Root locus plot for the system with a conventional control system (GFL/GFM), varying the value of the converter delay T_Σ.

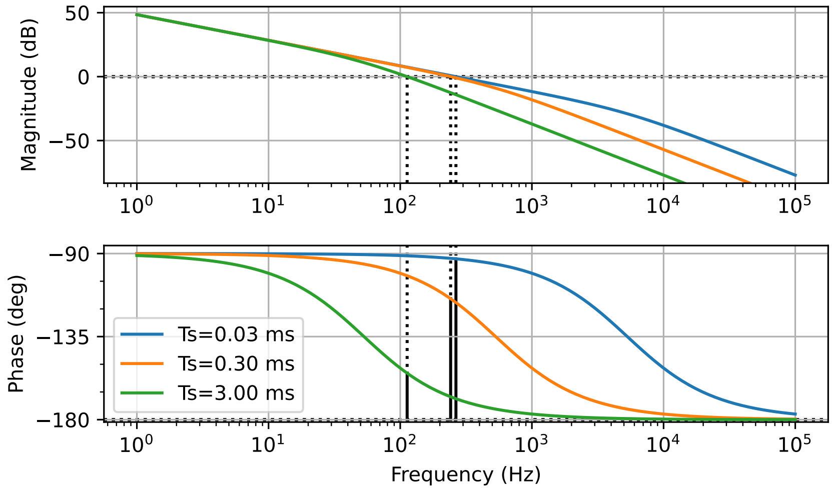

Figure 5.2: Bode plots for the system with a conventional control system (GFL/GFM), varying the value of the converter delay T_Σ.

The results for the HCC are shown in Figures 5.3 and 5.4. For very small values of T_Σ, the shape of the root locus does not change much. But, as the delay increases, it can be seen that the overall curves are drawn closer to the origin. Eventually, as T_Σ becomes even larger, this changes the poles and zeros of the transfer function in a way that they become conjugate pairs, changing the shape of the curves. The Bode plots show that the gain curve does not change much, but the phase curve does. As T_Σ increases, the phase margin decreases.

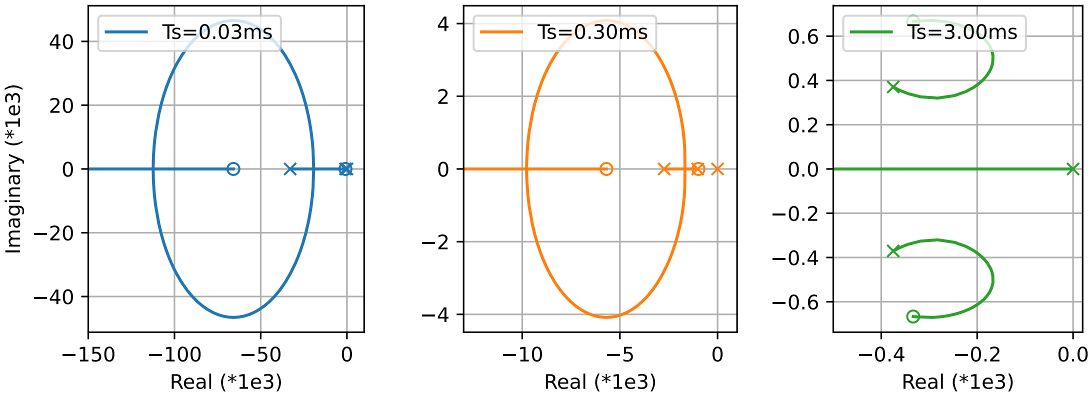

(a) (b) (c)

Figure 5.3: Root locus plot for the system with the HCC, varying the value of the converter delay T_Σ.

The two types of converter control (conventional and HCC) showed similar behavior with variations of the converter delay parameter: higher values of the delay make the system more prone to instability (poles move closer to the imaginary axis)

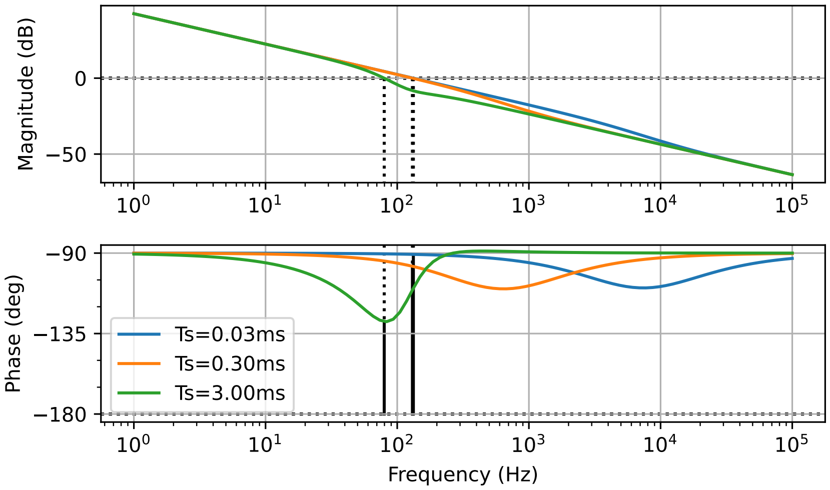

Figure 5.4: Bode plots for the system with the HCC, varying the value of the converter delay T_Σ.

and less robust from modeling uncertainties. Nevertheless, both the conventional and the HCC control system maintain stability with variations in T_Σ.

5.3 Impedance Mismatch

The precision and tolerance of manufacturing processes are important sources of uncertainty for all physical systems. In the analyzed case, this could lead to a discrepancy in the expected value of the filter resistance and inductance (R_f, L_f) and their actual values. Since the PI controller integration time constant is usually tuned according to these parameters, this mismatch between expectation and reality could lead to a different transient response than what is expected.

For this analysis, the time constant of the PI controller is tuned according to the expected values of the converter impedance, which means:

$$T_i = \frac{L_f}{R_f}, \tag{5.2}$$

while the actual values of impedance are defined by *mismatch factors* k_R and k_L, and therefore the plant equivalent transfer function (from Figure 4.2) becomes:

$$R_{actual} = k_R R_f, \tag{5.3}$$

$$L_{actual} = k_L L_f, \tag{5.4}$$

$$TF_{plant}(s) = \frac{1}{sk_L L_f + k_R R_f}. \tag{5.5}$$

The equivalent open-loop transfer functions, both for a conventional and for the HCC control systems, must be recalculated. For the conventional converter, (4.66) becomes:

$$TF_{open,GFL}(s) = k_p \frac{sL_f + R_f}{sL_f} \cdot \frac{1}{sT_\Sigma + 1} \cdot \frac{1}{sk_L L_f + k_R R_f}, \tag{5.6}$$

$$= k_p \frac{sL_f + R_f}{s^3 k_L L_f^2 T_\Sigma + s^2 L_f(k_L L_f + k_R R_f T_\Sigma) + sk_R R_f L_f}. \tag{5.7}$$

For the HCC, the same step-by-step simplifications, as shown in Figure 4.9a, are performed, considering the new plant transfer function. This results in:

$$TF_{open,HCC}(s) = \frac{k_{p,1}k_2}{sL_f} \cdot \frac{a_3 s^3 + a_2 s^2 + a_1 s + a_0}{b_3 s^3 + b_2 s^2 + b_1 s + b_0}, \tag{5.8}$$

$$a_3 = k_L L_f^2 T_\Sigma k_1, \tag{5.9}$$

$$a_2 = L_f \left[L_f(k_L k_1 + k_2) + k_R R_f T_\Sigma k_1 \right], \tag{5.10}$$

$$a_1 = L_f \left[R_f(k_R k_1 + k_2) + k_{p,2} k_1 (k_1^2 + k_1 k_2 + k_2) \right], \tag{5.11}$$

$$a_0 = R_f k_{p,2} k_1, \tag{5.12}$$

$$b_3 = k_L L_f^2 T_\Sigma, \tag{5.13}$$

$$b_2 = L_f(k_L L_f + k_R R_f T_\Sigma + T_\Sigma k_L k_{p,2} k_1 k_2), \tag{5.14}$$

$$b_1 = L_f(k_R R_f + k_{p,2} k_1^2) + k_{p,2} k_1 k_2 (k_L L_f + T_\Sigma k_R R_f), \tag{5.15}$$

$$b_0 = R_f k_{p,2} k_1 (k_1 + k_R k_2). \tag{5.16}$$

There are two main ways in which k_R, k_L can vary, defined as:

- *Symmetrical Mismatch*, when $k_R = k_L = k_{RL}$, which maintains the impedance ratio L_f/R_f, and
- *Asymmetrical Mismatch*, when $k_R \neq k_L$.

Individual analyses are conducted for each of these two cases.

5.3.1 Symmetrical Mismatch

For the case of Symmetrical Mismatch, the conventional control system's equivalent open-loop transfer function from (5.7) can be simplified to:

$$TF_{open}(s) = \frac{k_p}{k_{RL}} \frac{sL_f + R_f}{s^3 L_f^2 T_\Sigma + s^2 L_f (L_f + R_f T_\Sigma) + sR_f L_f}, \tag{5.17}$$

$$= \frac{k_p}{k_{RL}} \frac{sL_f + R_f}{(sL_f)(sT_\Sigma + 1)(sL_f + R_f)}, \tag{5.18}$$

$$= \frac{k_p}{k_{RL}} \frac{1}{s^2 L_f T_\Sigma + sL_f}, \tag{5.19}$$

which is simply the transfer function developed previously, in (4.67), divided by the mismatch factor. In this case, the root locus and Bode plots do not change shape, the only difference being in the resulting performance indexes. Since the transfer function is the same as before but multiplied by a factor $1/k_{RL}$, and k_p was originally designed with the values of R_f, L_f in mind, the controller leads to a different transient response than expected. For example, the overshoot and settling time values change, but otherwise not much discrepancy and possible instability is present.

For the HCC, the equivalent open-loop transfer function from (5.9) can be simplified to:

$$TF_{open,HCC}(s) = \frac{k_{p,1} k_2}{sL_f} \cdot \frac{s^2 k_{RL} L_f T_\Sigma k_1 + sL_f (k_{RL} k_1 + k_2) + k_{p,2} k_1}{s^2 k_{RL} L_f T_\Sigma + s k_{RL} (L_f + T_\Sigma k_{p,2} k_1 k_2) + k_{p,2} k_1 (k_1 + k_{RL} k_2)}. \tag{5.20}$$

It can be seen that, if $k_{RL} = 1$, which means no impedance mismatch, (5.20) becomes equal to the originally developed equation for the HCC open-loop transfer function, (4.81).

The root locus plot for the HCC control system is shown in Figure 5.5. The overall shape of the curves does not change much. The main difference is that, for $k_{RL} < 1$, two poles gain an imaginary component and become complex conjugates. The root locus stays in the left half-plane for any value of k_{RL}, never crossing the imaginary axis.

The Bode plots, shown in Figure 5.6, show only a minor variation in the gain plot. The phase curve shows an increased bulge when $k_{RL} < 1$, going closer to the 180^o. Nevertheless, since this does not happen in the vicinity of the frequencies where the gain curve crosses the 0 dB mark, the phase margin is almost unaffected. A large shift would be required to make the curves cross these critical points simultaneously, therefore it can be concluded that the HCC has a good safety margin against symmetrical impedance mismatches.

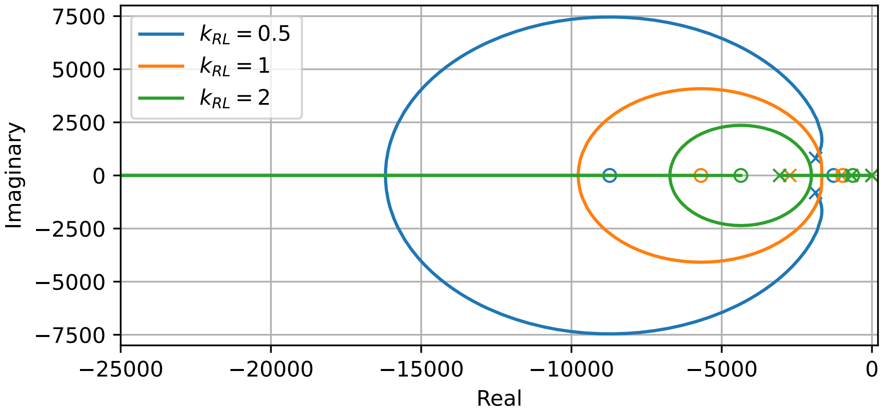

Figure 5.5: Root locus plot for the HCC control system, considering a symmetrical mismatch, varying the value of the mismatch factor k_{RL}.

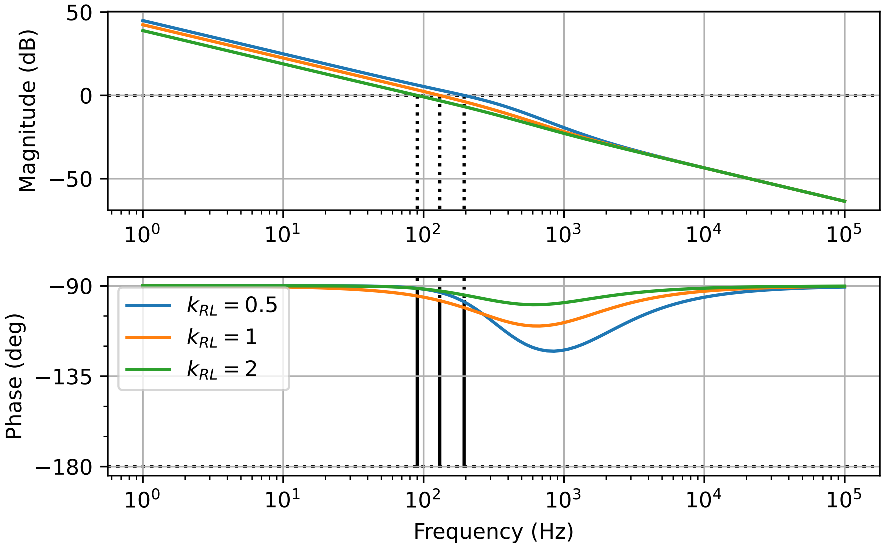

Figure 5.6: Bode plots for the HCC control system, considering a symmetrical mismatch, varying the value of the mismatch factor k_{RL}.

5.3.2 Asymmetrical Mismatch

Unlike in the case of Symmetrical Mismatch, here the conventional control system's transfer function, described in (5.7), suffers a change to its poles and zeros. This affects the curves' shape, as shown in Figure 5.7 (considering $k_L = 1$). Depending on the value of k_R being smaller or larger than k_L, one pole migrates from the left- to the right-side of the zero, changing the shape of the pole trajectories. Even so, they stay in the left half-plane, never crossing the imaginary axis. The main point of interest when comparing with the previous case (where $k_R = k_L$) is the zero that appears in the transfer function, which keeps the trajectory of one of the poles somewhat close to the imaginary axis, closer to the instability region. Aside from the different shape near the zero, the pole trajectories for k_R smaller or larger than k_L both follow a similar path, meeting further away in the negative region of the real axis and moving vertically afterwards, even though this trajectory for the case where $k_R < k_L$ is slightly closer to the imaginary axis. The Bode plots in Figure 5.8 confirm this analysis, where the curve shapes do not differ much, just leading to a slightly lower phase margin for the case where $k_R < k_L$.

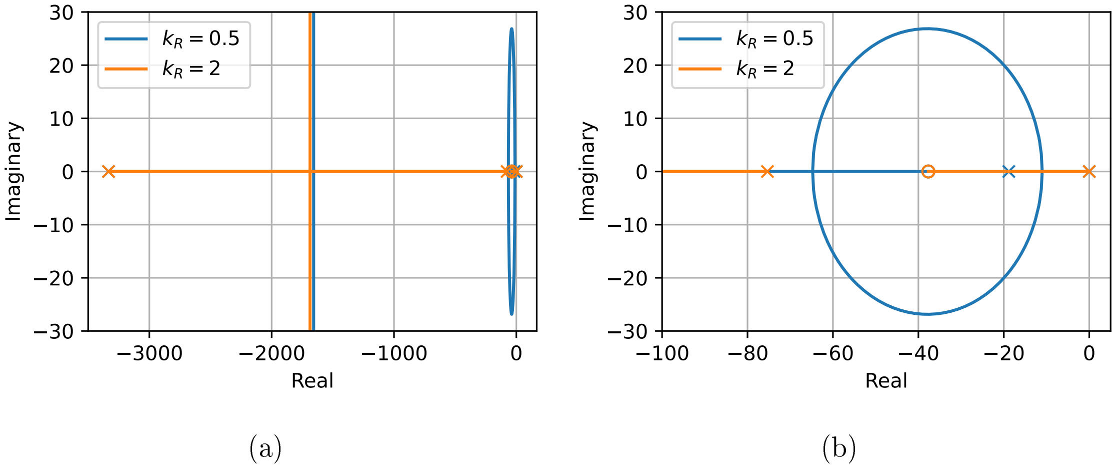

Figure 5.7: Root locus plot for the system with a conventional control system (GFL/GFM), considering an asymmetrical mismatch, varying the value of the resistance mismatch factor k_R; (a) full root locus, and (b) zoom of the right-most part.

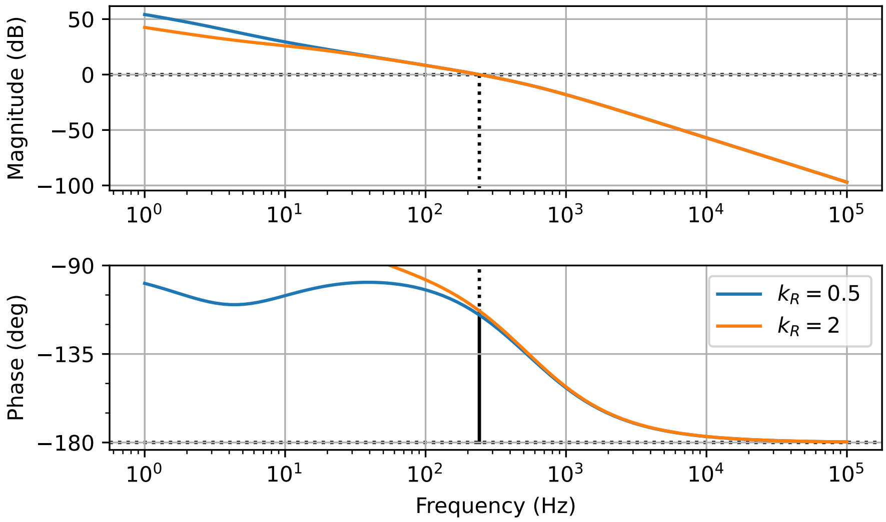

Figure 5.8: Bode plots for the system with a conventional converter (GFL/GFM), considering an asymmetrical mismatch, varying the value of the resistance mismatch factor k_R.

As for the HCC, using the equivalent transfer function described in (5.9), both the root locus and the Bode plots in Figures 5.9 and 5.10 show only a very small effect in the curves shape. The phase plot shows a slight change to the curvature, but the phase margin is almost unchanged.

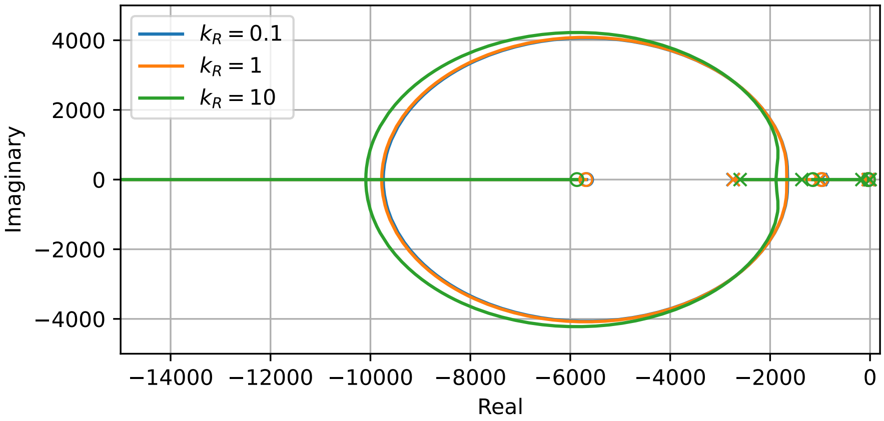

Figure 5.9: Root locus plot for the HCC control system, considering an asymmetrical mismatch, varying the value of the resistance mismatch factor k_R.

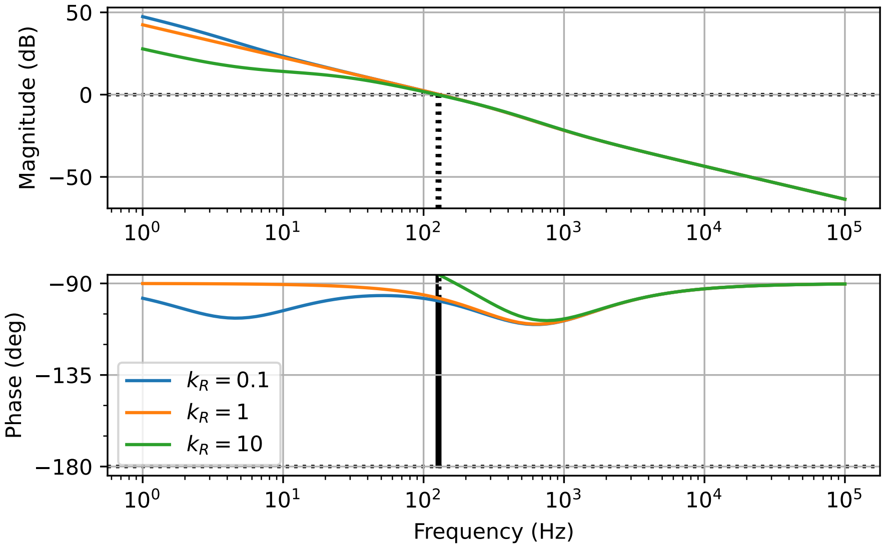

Figure 5.10: Bode plots for the HCC control system, considering an asymmetrical mismatch, varying the value of the resistance mismatch factor k_R.

The analyzed cases showed that impedance mismatches are not critical factors neither for a system with a conventional control system nor for the HCC control system. Depending on the impedance mismatch, the pole trajectories in the root locus plots may move closer to the imaginary axis, but they do not cross to the right half-plane. The Bode plots show large values of gain and phase margins. Therefore, the HCC is able to operate under impedance mismatches maintaining its stability, displaying high robustness to impedance variations.

5.4 Switching Effect and Converter Filter

As mentioned in previous chapters, the reference output voltage generated by the converter's control system goes through a switching algorithm, which sends the appropriate signals to activate the semiconductor switches in a controlled manner. Therefore, the actual output voltage that appears at the converter terminals is different from the reference value, since it includes components introduced in the switching action of the converter.

Generally, switching algorithms such as Pulse-Width Modulation (PWM) generate pulse trains, where the switching signal's average value, in a given switching period, is equal to the average value of the reference signal. This way, even though the output waveform is shaped like a pulse train, the average value over consecutive switching periods matches that of the original sinusoidal reference signal. This assumption holds true when the switching frequency is high enough so that the reference signal may be assumed linear during one switching period. Figure 5.11 illustrates this behavior, where the switching periods are delimited by vertical dashed lines. The switching periods are purposely large in this example to facilitate the visual interpretation.

As the output voltage is generated using a switching algorithm that results in small, discrete periods of time where the voltage is constant, a delay appears between the output voltage and the reference signal's fundamental harmonic component. This is due to the fact that, as opposed to this discrete behavior of the output voltage, the reference signal, which is sinusoidal, is varying over time. This behavior is one of the main causes of delay in the converter, represented by the parameter T_Σ that was mentioned in previous sections.

The converter is connected to the PCC through a filter (usually LCL), with the specific purpose of mitigating the voltage harmonics generated by the switching algorithm. This means that, even though the voltage at the converter terminals may have a high harmonic content, it is lower for the PCC voltage and for the output current.

The voltage and current measurements are taken at the LCL filter capacitor and at the PCC, respectively, and sent to the control system. This means that, if the measured signals have harmonic content, they may affect the dynamic behavior of the converter since, usually, the control system is designed (for example, when choosing the gains of the PI controller) considering an ideal situation with no harmonics. Nonetheless, extra control system loops or components may be added to mitigate and deal with specific harmonic components. It is common to employ, in the control system, a low-pass filter to the measured values, further reducing the amount of signal noise.

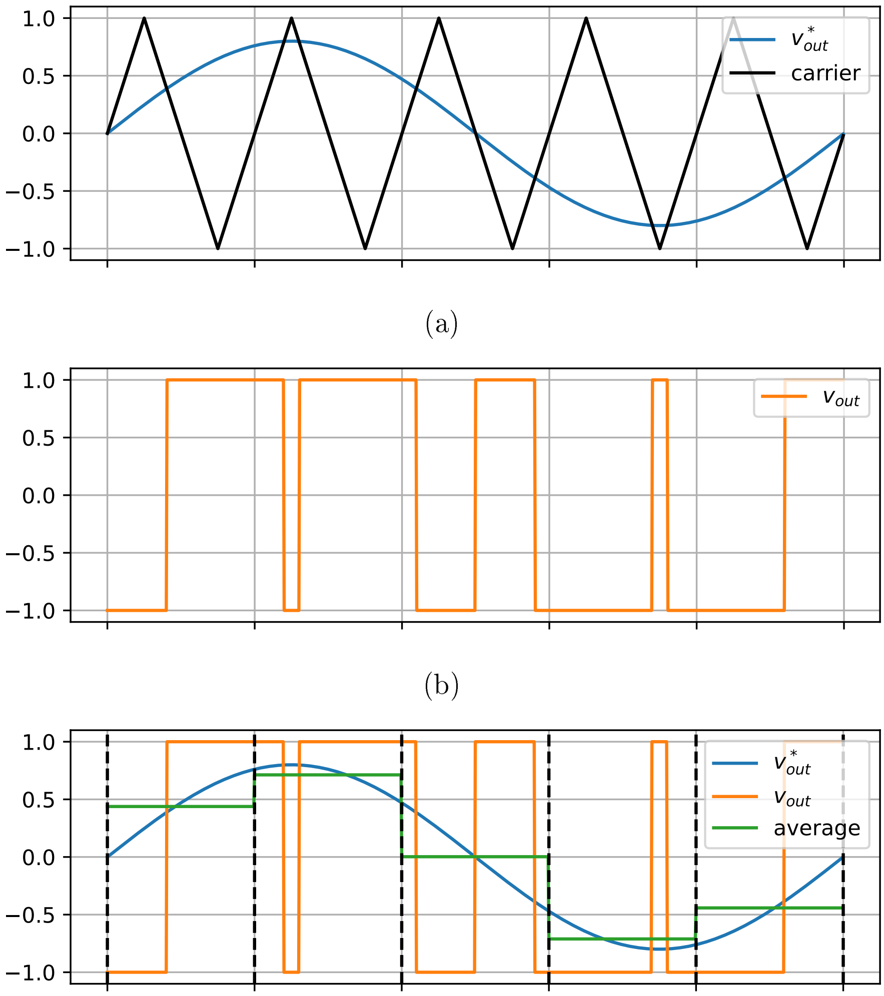

(a)

(b)

(c)

Figure 5.11: Detail of the PWM switching scheme; (a) reference voltage and PWM carrier-wave, (b) resulting output voltage, shaped like a pulse-train, and (c) switching periods, where the average values of the reference and output voltages are equal.

There are two factors that may affect converter performance related to the switching effect. The first one is that the delay is usually represented in the equivalent transfer function as a simple first-order component, which is a great simplification of the actual switching process. The second one is that the output harmonics may affect the behavior of the control system. Any power electronics converter suffers from these two factors, and the HCC is no exception to the rule.

Besides that, the converter output filter also requires a closer inspection. Usually, this filter includes series-connected inductors and/or parallel-connected capacitors, with values chosen based on the electrical system parameters and desired harmonic content mitigation characteristics. One of the most common topologies is the LCL filter, as shown previously in Figure 2.3, which includes a series-connected inductor, a parallel-connected capacitor (with a series damping resistor), and a second series-connected inductor. Since the filter capacitance is chosen to represent a high impedance for harmonic components near the nominal frequency and low impedance for components of higher frequency, in most control system analyses and calculations it is simply disregarded, and the filter is assumed to be comprised of a single series-connected inductor.

Since the control system is usually designed considering the filter as a simple RL component but the actual filter is an LCL component, this simplification leads to some discrepancy between the calculated and the actual dynamic behavior of the converter.

A simulation is set up, considering the same system and control system parameters as described in Section 3.5.2. This time, a simple PWM switching algorithm is included, to evaluate the performance of the HCC including the switching effect. The converter filter is also represented as a LCL component instead of RL. The dc link is assumed to have constant voltage V_{dc} (thus neglecting voltage ripples), and the PWM carrier wave amplitude is set at the value of V_{dc}. The filter components and the switching frequency were designed according to the methodology proposed by Liserre et al. [73]. It is important to note that the test system shown in that study results in a lower harmonic content in the output voltages and currents because it is connected directly to an ideal voltage source. The cut-off frequency for the measurement low-pass filters is chosen to be ten times the nominal frequency. The extra parameters used in this simulation are summarized in Table 5.1.

Table 5.1: Extra parameters used in the simulation of the HCC including the switching effect.

Parameter	Symbol	Value
dc-Link Voltage	V_{dc}	±31.8 kV
PWM Carrier Wave Frequency (Switching Frequency)	f_{PWM}	6.0 kHz
Filter Parallel Branch	$R_{f,C}$	23.0 Ω
	C_f	1.1 μF
Filter Branch (Converter-Side)	$R_{f,cs}$	320.4 mΩ
	$L_{f,cs}$	8.5 mH
Filter Branch (Grid-Side)	$R_{f,gs}$	535.3 mΩ
	$L_{f,gs}$	14.2 mH
Low-Pass Filter Cut-Off Frequency	ω_{LPF}	3769.9 rad/s

The simulation is similar to the one described in Section 3.5.2, where the HCC undergoes a step increase in its GFL-part reference active power, and then the load connected to the grid increases, prompting an automatic increase in the GFM-part delivered power due the grid frequency drop.

Figure 5.12a shows the HCC output voltage reference (v^*_{out}) and the actual voltage that appears at the HCC terminals (v_{out}), highlighting the switching effect. Due to the presence of the filter, the voltage at the PCC has a reduced harmonic content when compared to the HCC terminals voltage, as shown in Figure 5.12b.

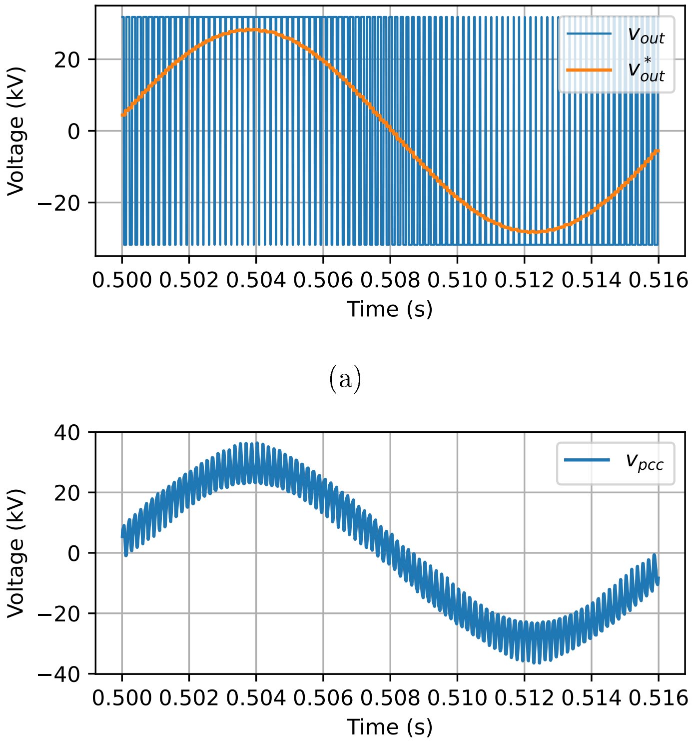

(a)

(b)

Figure 5.12: Voltages of the simulation including the switching effect: (a) HCC output voltage and (b) PCC voltage.

Figure 5.13 shows the HCC output active power. It can be seen that, as expected, the HCC output power increases at $t = 0.75s$ following the reference step increase, and it also increases at $t = 1.0s$ as it provides automatic grid support when the frequency drops.

This simulation shows that, similarly to any other type of converter control, the HCC works well even though the switching effect was disregarded and the filter was simplified during the design of the control system. These common adaptations are valid for the HCC just as they are for other types of control systems, bringing no extra instability nor hindering the behavior of the HCC.

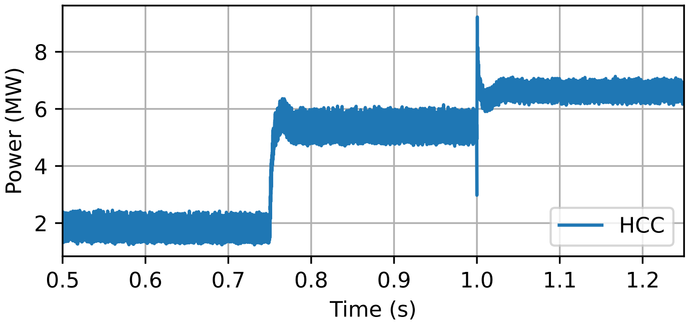

Figure 5.13: HCC output active power, including the switching effect and LCL filter in the simulation.

5.5 Partial Conclusion

The design and tuning of control systems usually rely on neglecting or simplifying some characteristics of the actual physical system upon which the control system acts. Even though such simplifications increase the modeling uncertainty, without them it would be very difficult, time-consuming and possibly costly to achieve a good mathematical representation of the system and to design the control system itself.

This chapter presented and discussed some important factors that are usually simplified and increase the model uncertainty when designing control systems for power electronics converters. They are: the converter delay parameter, the possible impedance mismatch, the switching effect and the filter topology. The discussion included comparisons between conventional converter control systems (such as GFL and GFM) and the HCC.

Results showed that, both for a conventional control system and for the HCC, these factors may move the control system closer to the instability region, although none of them would directly lead to instability. A time-domain simulation also showed that the HCC properly works when the switching effect and a detailed model of the LCL filter are included. These results confirm that, even though some usual simplifications and assumptions were made in the development of the HCC control system, they do not lead to instability, reduced robustness or increased sensitivity to parameter mismatch.

It is important to note that there are other situations, not discussed in this chapter, that could also be analyzed to assess the robustness of a control system. For example, situations with unbalanced grid voltage or impedance, unbalanced filter impedance, short-circuit and/or low-voltage ride through, presence of multiple converters connected to nearby nodes, etc. These are specific studies used to assess the stability and robustness of any control system, be it a conventional or a new one, and should be performed on a case-by-case basis. The main conclusion of this chapter is that, for the analyzed cases, results indicate that the HCC is as robust as conventional converter control schemes such as GFL and GFM.

Chapter 6

Applying the Hybrid Control Converter to Wind Turbines

This chapter presents the basic components of a wind turbine, discussing the role of the power electronics converter in the energy conversion process. A major limitation of wind turbines is discussed, highlighting that the issue mainly comes from the behavior of the converters.

An application of the HCC with wind turbines is proposed, aimed at improving the WT's frequency support capability. Simulation results show the advantage it brings to the turbine when compared with the traditional GFL, by improving the turbine's frequency support capability.

6.1 Wind Energy Principles

Wind energy has been employed by mankind since early history, in different forms. Two familiar examples are sailing, which was the main way to travel through sea until the industrial revolution, and grinding grains in wind-powered mills. Nowadays wind is mostly used to generate electricity, and it has received massive amounts of attention and investment in recent years due to being a clean, infinite and renewable source of energy.

The kinetic energy is extracted from the wind and transformed into electrical energy using Wind Turbines (WT). There are different ways to build a WT, but currently the Horizontal-Axis Wind Turbine (HAWT) is the one that dominates the market, due to its advantageous cost and efficiency. It is comprised of several components that work together to generate energy, as shown in Figure 6.1. The hub, also known as nose, is where the blades are connected, and rotates according to the incoming wind. It is essentially the front of the turbine, and the endpoint of the low-speed shaft. The blades can rotate along their own axis controlled by pitch motors, driven by a hydraulics system. The pitch motors adjust the angle in which the blades face the wind (also known as angle of attack), which changes the energy conversion characteristics of the turbines depending on the wind conditions. The hub is connected to the nacelle, where the other components are located. The WT may contain a gearbox, coupling the low-speed shaft to a high-speed shaft, connected to the electrical generator. The power electronics converter and its control system control the generator and the turbine rotating speed, ensuring it extracts the maximum possible energy from the wind, while maintaining the system under safety limits of speed, torque and current. There is a mechanical braking system for emergency situations, wind speed and direction sensors, and yaw motors that rotate the entire nacelle, ensuring it is always properly facing the incoming wind even when it changes direction. The only component located on the bottom of the tower is usually the transformer, that raises the voltage level to reduce electrical losses in the Medium-Voltage Distribution Network (MVDN).

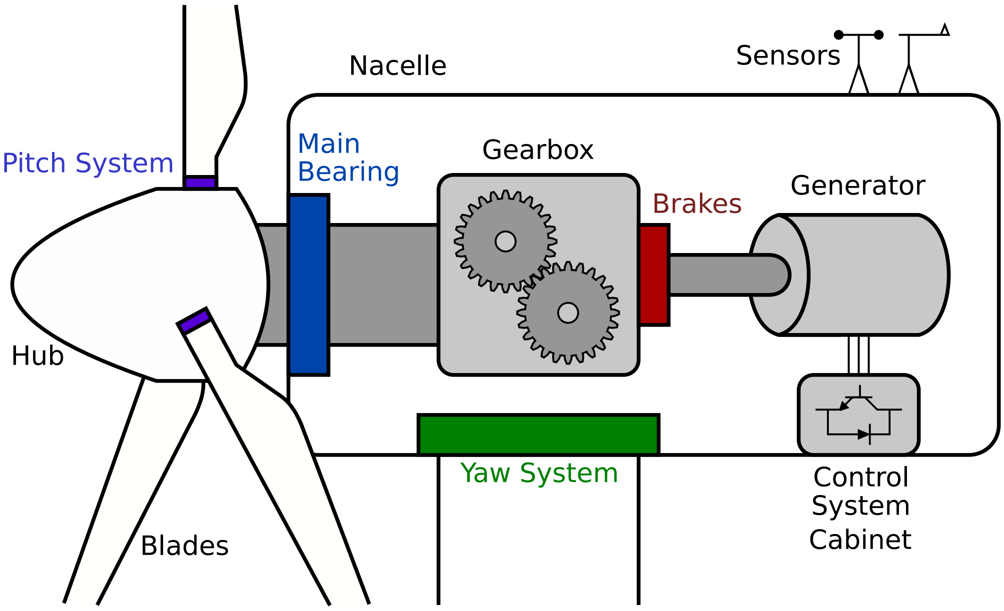

Figure 6.1: Main components of a wind turbine.

Even though those are the main components, there are different ways to build and operate a wind turbine, leading to different operational characteristics. The four main types of wind turbines, described in the following sections, are:

- Type I: fixed-speed with squirrel-cage induction motor,
- Type II: variable-speed with wound-rotor induction generator,
- Type III: variable-speed with a doubly-fed generator, and
- Type IV: variable-speed with a full-converter.

6.1.1 Wind Turbine Types

Type I wind turbines have the simplest build. They were the first implementation of the HAWT, introduced in the 1980s, and have as main advantages their simplicity, robustness and initial cost. They employ a squirrel-cage induction generator, directly connected to the grid via a transformer, and do not employ a PEC nor a control system. Since it does not have brushes or a slip ring, it has increased robustness and less components that degrade over time. Because of this topology, the rotor speed does not vary much around the nominal value (around ±1%), according to the slip that comes with the generated power. A schematic of the main components is shown in Figure 6.2.

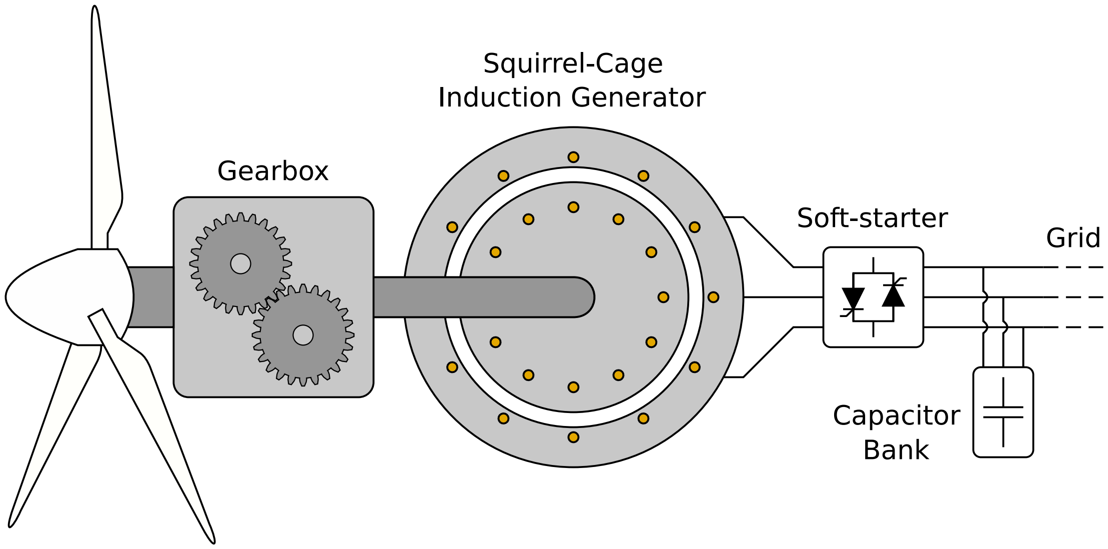

Figure 6.2: Components of a Type I wind turbine.

Since its rotating speed is not controllable and varies very little, this kind of turbine cannot provide optimal energy extraction from the wind for most wind conditions in the operating range. This may lead to increased fatigue since fluctuations in wind speed lead directly to mechanical stress and electrical oscillations. Capacitor banks are also needed, to compensate for the generator reactive power demand.

Technological developments led to fixed-speed simply being replaced by variable-speed turbines, which are able to generate more energy in the same wind conditions.

Type II wind turbines employ wounded rotors connected to a resistance through a chopper converter. By changing the equivalent rotor resistance, it is possible to change the slip (and the turbine torque/speed characteristics) and expand the operating range of the rotor speed to around ±10% of the nominal value. This, in turn, enables optimal energy generation on a wider range of wind conditions. This turbine topology is shown in Figure 6.3.

This kind of turbine employs a power converter to control the operation of the rotor chopper. Apart from the increased heat from energy dissipation in the rotor

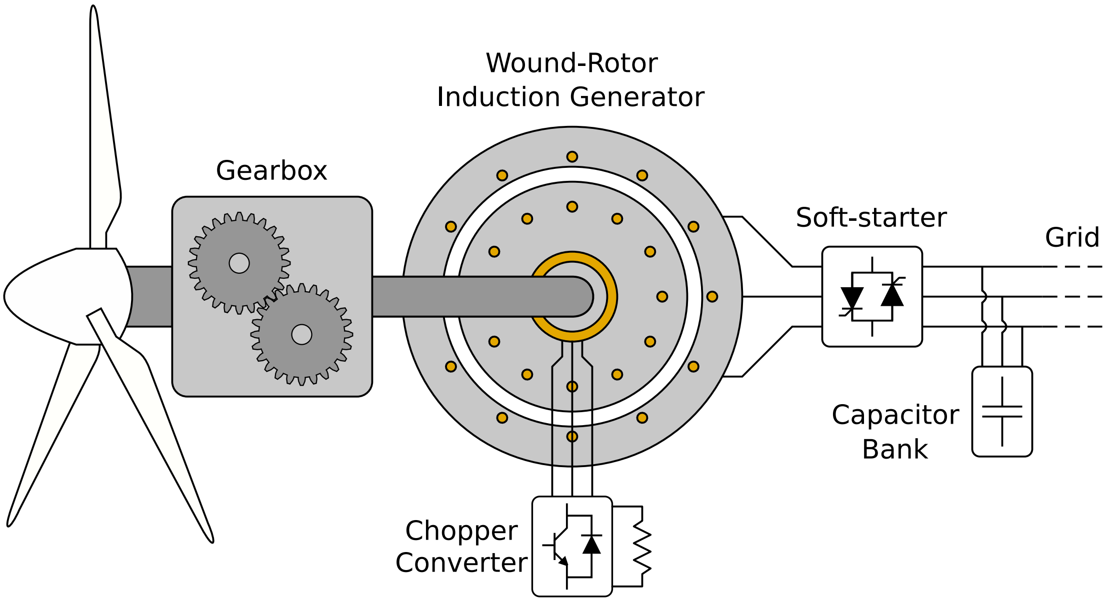

Figure 6.3: Components of a Type II wind turbine.

resistance, Type II turbines still present some of the drawbacks of Type I, such as the need for capacitor banks. They have mostly fallen out of use, being heavily outclassed by Type-III and -IV turbines in terms of generation capacity and efficiency.

Type III wind turbines, also called Doubly-Fed Induction Generators (DFIG), employ a wounded rotor which is connected to the grid by means of a back-to-back power electronics converter, as shown in Figure 6.4. The back-to-back unit is comprised of a Rotor-Side Converter (RSC) and a Grid-Side Converter (GSC). This allows for bidirectional power flow in the rotor circuit, enabling a much greater operating range in terms of rotating speed (around ±30% of the nominal speed) and improving the WT's overall power conversion efficiency. As the converter controls the rotor current, rotor losses are also much lower when compared with Type II turbines.

Since most of the power flows through the stator circuit, the back-to-back converter has a rated power of about 30% of the WT's nominal power. The grid-side converter performs reactive power compensation, thus dismissing the need for capacitor banks. It can also provide a smooth grid connection and some grid support due to its controllability. Nevertheless, the converter requires the usage of a filter to compensate for its harmonic content. The rotor-side converter controls the rotor speed and the active and reactive power flow through the stator circuit. Currently, most onshore wind farms employ Type III turbines due to their clear advantage and higher power generation when compared to its predecessors.

Finally, **Type IV** wind turbines employ a full-scale back-to-back converter to connect the generator to the grid, as shown in Figure 6.5. In this case, the RSC is called Stator-Side Converter (SSC), due to it being connected to the stator terminals

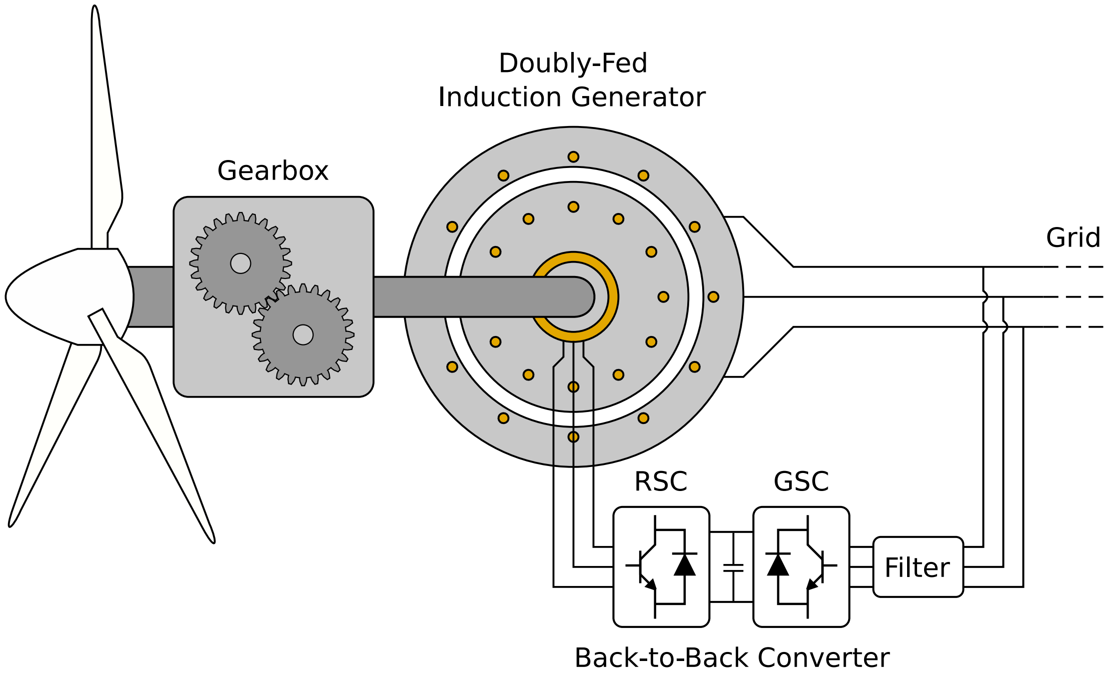

Figure 6.4: Components of a Type III wind turbine.

of the machine. This way, full controllability of the rotor speed is achieved, which enables a direct drive connection that does not employ a gearbox. This kind of converter decouples the generator entirely from the grid, providing good resilience against disturbances. It also enables power factor compensation and some grid support capability.

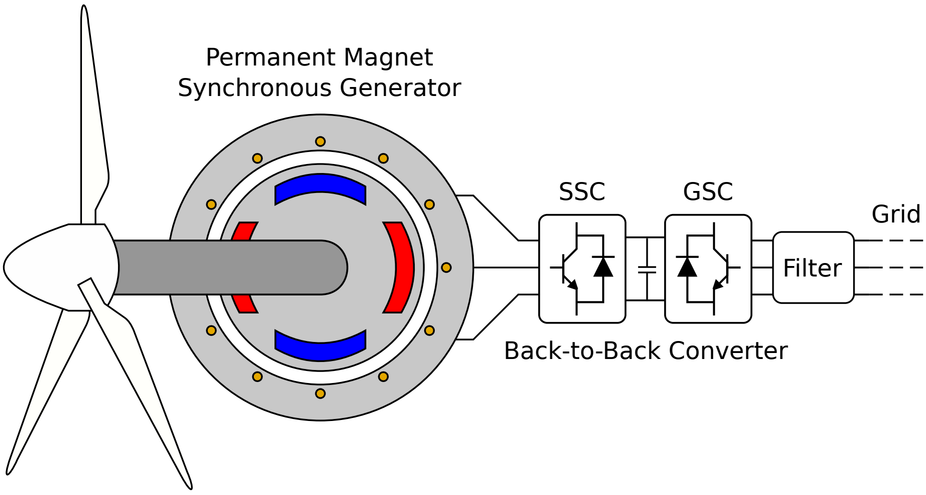

Figure 6.5: Components of a Type IV wind turbine.

Usually, Type IV turbines employ permanent magnet synchronous generators, which have high reliability. The absence of a gearbox, slip rings and brushes also increases the reliability of the system and reduces maintenance costs. On the other hand, the generator is more expensive due to the high cost of permanent magnets and the need to employ a multi-pole design to accommodate the direct drive system, resulting in a machine with a larger diameter and costly manufacturing process. In summary, comparing with the other ones, Type IV turbines are usually the most expensive, but also most reliable and with the highest megawatt rating. They are the prime choice for offshore wind farms, for which reliability plays an especially important role due to the difficulty that maintenance teams face to access them.

6.1.2 Limitations and Problem Statement

Turbines of type III and IV are the ones currently employed for wind generation. Their back-to-back converter provides much needed flexibility and controllability, ensuring optimal power capture for most of the operating range. It is important to understand in more detail how it works on each case.

For a Type III turbine, the power flow is dictated by the rotor slip, which is the difference in rotating speed between the stator and rotor magnetic flux vectors. Since the stator is directly connected to the grid, the grid voltage creates a given magnetic flux in the generator air gap that follows the grid frequency, which usually does not vary much from its nominal value. The only way to control the slip is by controlling the rotor magnetic flux vector through the rotor current.

The rotor-side converter of the back-to-back configuration controls the three-phase current in the rotor circuit. According to measurements of wind speed, rotating speed and operational conditions of the machine, an MPPT algorithm calculates the optimal power flow that can be achieved. Then, it controls the amplitude, frequency and phase angle of the rotor currents, which affect the resulting rotor magnetic flux, the slip, and consequently the power flow in the generator. Depending on the operating point, the rotor currents may have a negative or positive frequency (considering the grid voltage as reference), leading to active power flowing out of or into the stator circuit, from the rotor circuit. This means that the RSC is bidirectional in terms of power flow, and can either supply or consume active power to/from its dc link.

But it is of utmost importance to keep the dc link of the back-to-back converters in a given operational range of dc voltage. If it drops or increases too much, the converters are unable to synthesize the reference output voltages at their terminals. Since the RSC is strictly controlling the rotor currents, the grid-side converter is then tasked with controlling the dc-link voltage. It is a simple control strategy: based on the dc voltage level, the active power delivered to or consumed from the grid is adjusted, to minimize voltage excursions. The GSC can also change its reactive power setpoint depending on specific grid requirements.

The behavior is similar for Type IV turbines. The main difference is that the back-to-back converter is connected to the stator circuit, so there is no direct connection between the generator and the grid. In most cases, the rotor magnetic flux cannot be accessed or controlled (for example, if using permanent magnet machines), so the stator-side converter controls the magnetic flux generated by the stator. The control strategy is based on the wind conditions and an MPPT algorithm to determine the optimal power extraction at a given operating point, and the stator currents are controlled (amplitude, frequency, phase angle) to achieve that maximum power. The GSC retains the task of keeping the dc-link voltage inside the acceptable operating range.

At the end of the day, the amount of power delivered to the grid by a WT is entirely dictated by its controller, which means its behavior is fully decoupled from the grid state on any given time. If the grid voltage or frequency deteriorate too much, leaving the safety operation range of the WT, it usually disconnects to avoid possible damage, following some kind of Fault Ride-Through requirement.

The generated power from traditional sources, such as hydro or thermal synchronous generators, is affected by the grid state. The generated power is not a direct consequence of the controller; it is a consequence of the difference between the grid voltage and the generator voltage, which depends on the mechanical torque of the machine's rotor. If the grid voltage or frequency change, the SG is automatically affected, resulting in changes in load angle and torque. This means that SGs automatically provide grid support, resulting in smoother fluctuations of grid voltage and frequency.

For a WT to provide extra power during a grid fault, the most common way is by implementing a Synthetic Inertia (SI) control loop. When the GSC's PLL detects a drop in grid frequency, a signal is sent to the RSC to activate this control loop. It stops tracking the MPPT, and increases the power flowing from the RSC into the dc link. The mismatch between mechanical torque (coming from the wind) and the electrical torque, that is increased, leads to a slowdown in the turbine's rotating speed, much like a regenerative braking system. Therefore, even though there is an increase in the generated power, it comes at the cost of reducing the WT's speed, so the Synthetic Inertia functionality can only be activated for around 5 to 10s to avoid excessive slowdown.

Both for type III and IV wind turbines, the RSC (or SSC) follows a specific power or current reference, to ensure optimal energy extraction from the wind. The GSC follows an active power reference, calculated from the dc-link voltage, that controls the power delivered or consumed from the grid. This way, both converters of the back-to-back unit usually work as Grid-Following Converters. Unfortunately, this also means that they have limited grid support capabilities, as mentioned previously in Chapter 2. Even if extra control loops such as Synthetic Inertia are added to the control system with the specific purpose of providing grid support, they are inherently slower than a traditional SG or a GFM, leading to higher grid oscillations especially on grids with high penetration of Inverter-Based Resources.

6.2 Proposed Application

The bottleneck for wind turbines and grid support is the fact that the converters are implemented as GFL. Since controlling the dc-link voltage is a fundamental necessity of the back-to-back converter, it cannot be replaced by a GFM, which does not provide power controllability. Therefore, a possible solution to this issue is to employ the HCC. By having GFL characteristics, the HCC enables accurate control of the dc link, while also providing the GFM behavior advantages such as inherent grid support capability.

The active power flow in the back-to-back converter of a Type III WT can be described as

$$p_{GSC} = p_{cap} + p_{RSC}, \tag{6.1}$$

where p_{GSC} is the active power flowing from the dc link to the GSC, p_{cap} is the active power flowing from the dc-link capacitor and p_{RSC} is the active power flowing from the RSC to the dc link, as shown in Figure 6.7. For Type IV turbines the analysis is similar, simply exchanging RSC with SSC.

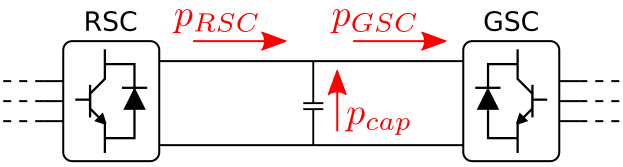

Figure 6.6: Schematic of the active power flow in a back-to-back converter.

During regular operation of the GSC implemented as HCC, its GFM-part reacts automatically to changes in grid frequency, increasing the active power delivered to the grid in case of underfrequency. If an increase in the active power delivered to the grid by the GSC is not accompanied by an increase in the active power delivered from the WT to the dc link by the RSC/SSC, then this extra power must come from the dc-link capacitor. Its voltage reduces, which triggers the dc voltage control loop of the GFL-part of the GSC, increasing the active power consumption from the grid and essentially counteracting the GFM-part behavior. Since the GFM-part is faster, at the very first moments of a fault, it does lead to increased and faster power delivery, but right after that, the GFL-part consumes power back from the grid to restore the dc voltage, which could be detrimental to the grid frequency transient.

To tackle this issue, two adjustments to the HCC control structure presented in Chapter 3 are proposed. First, a droop is added to the dc voltage reference of the GFL-part of the GSC, as shown in Figure 6.7a. Depending on the active power output of the GFM-part, a reduction in the dc reference voltage is applied (with a low-pass filter to avoid noise). This way, when an underfrequency transient happens, the GFM-part automatically provides extra power to the grid, leading to a reduction in the dc-link voltage, but since the dc voltage reference is also reduced, the GFL-part does not instantly try to consume power from the grid to replenish it. Therefore, a better frequency support capability is achieved, so long as the new and reduced dc voltage reference is not detrimental to the converter switching process. A minimum acceptable limit of the dc voltage reference should be set in the droop control to ensure the converter works properly. When the Synthetic Inertia kicks in, increasing the power delivered from the WT to the dc link, the GSC active power also increases, to avoid dc-link overvoltage.

A second adjustment is made to the GFM-part control. In steady-state, the WT should operate following the MPPT and with the nominal value of dc voltage. Therefore, the power delivered to the grid by the GFM-part must return to zero after a while, even if the underfrequency transient is not solved. To this end, the droops of the GFM-part are replaced by PI controllers, as shown in Figure 6.7b. The proportional part results in a behavior simliar to a regular droop, while the integral part of this new controller ensures that the GFM-part's output power goes back to zero after a while. This way, it works just as any GFM would when facing a grid transient, but eventually returns to an operating point where its active and reactive power are zero. At that moment, only the GFL-part of the GSC provides active/reactive power.

In the end, the HCC-based GSC essentially behaves as a GFM during the transient and as a GFL in steady-state. Its GFL-part maintains the dc voltage controlled at all times, while its GFM-part provides grid support when needed.

6.3 Results

To demonstrate the proposed applicability of the HCC with wind turbines, a simulation is set up. The goal is to compare the behavior of a regular wind turbine, with a GFL as the GSC, and a turbine employing the HCC as the GSC. In both cases, Synthetic Inertia control is employed to provide support during a load increase event.

The implemented Synthetic Inertia control follows the requirements described in the Brazilian Grid Code [74], that establishes that all WTs must be equipped with this functionality. It states that they must increase their output power by up to 10% of their nominal value, during at least 5 s, if the grid frequency drops below 59.8 Hz. The extra output power signal rises from zero up to 0.1 p.u., pro-

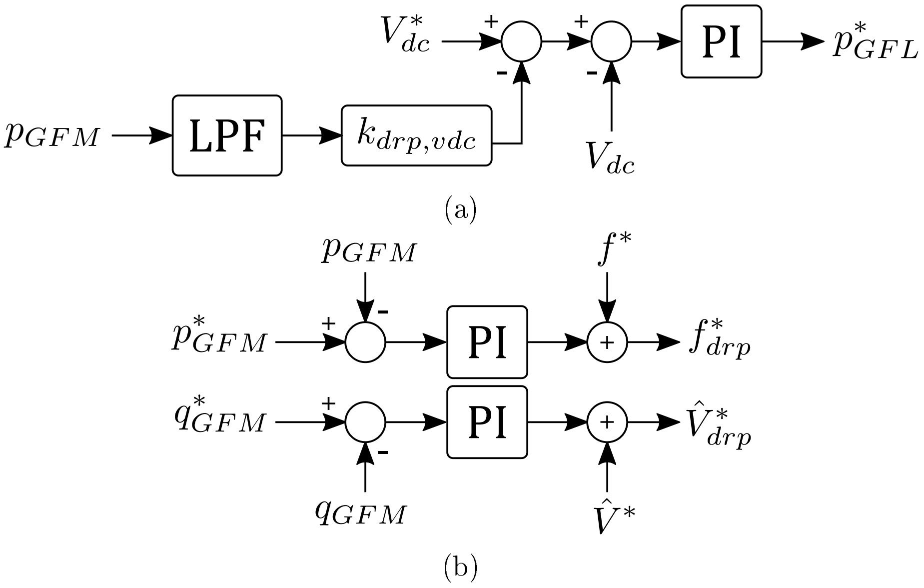

Figure 6.7: Proposed adjustments to the HCC control system for the application on wind turbines: (a) dc voltage control loop, in the GFL-part, and (b) droops, in the GFM-part.

portionally to the difference between the measured grid frequency and the minimum threshold of 59.8 Hz, with a rate of 0.8 p.u./Hz·s. After these 5 s, other generators (hydro/thermal) and energy storage devices should have already started to ramp up enough power to provide the necessary frequency support, and the WTs go back to normal operation. As part of the WT's rotational kinetic energy is used to increase the power delivered to the grid during the SI activation, its output power is reduced when this period is over, and it takes some time to build back up to the optimal rotating speed and output power. This behavior is shown in Figure 6.8.

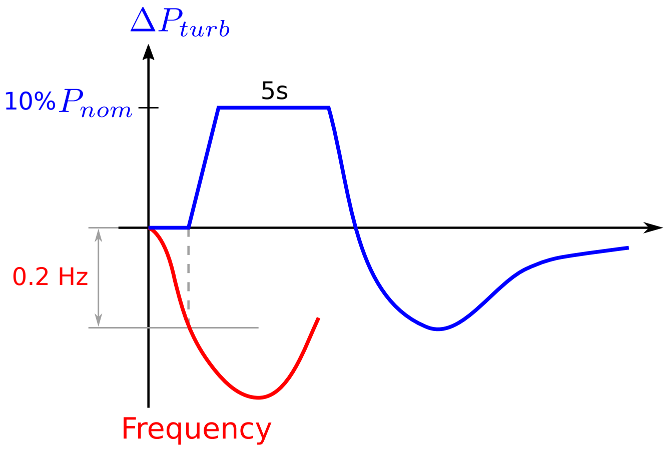

Figure 6.8: Synthetic Inertia control behavior, showing the extra turbine power (blue) and grid frequency (red).

The simulated system is shown in Figure 6.9. It includes a Type IV wind turbine with SI capability, its PEC filter and transformer, the medium-voltage distribution

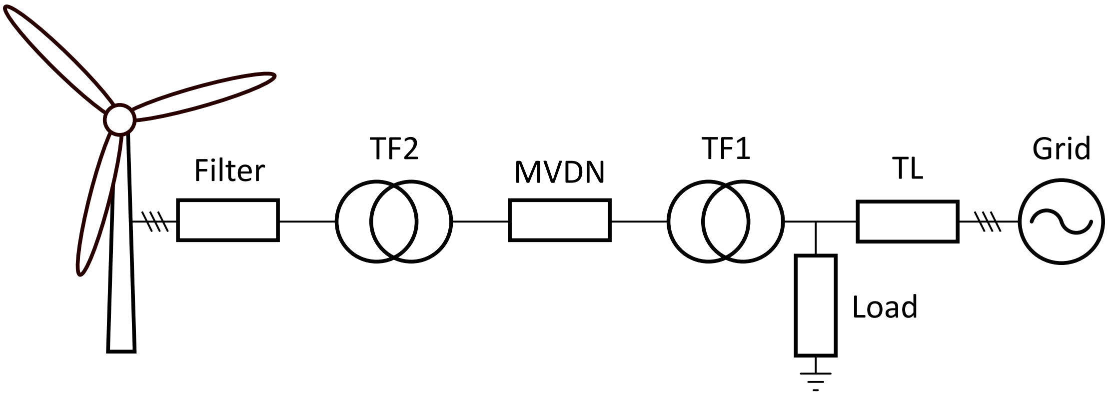

Figure 6.9: Schematic of the electrical system used in the simulation of the HCC applied to a wind turbine.

network, the substation transformer and the Transmission Line. Only one turbine of a wind farm is represented for simplicity. The impedance values of this electrical system are based on a real, operational wind farm in Brazil, and are described in Table 6.1 (transformer parameters are referred to their primary windings). The turbine filter and dc-link capacitance are adapted from [75]. The electrical grid is represented similarly to the simulations done in previous chapters, as a voltage source with inertia and droops (for primary frequency support) [25], to emulate the real behavior of an electrical system facing a frequency transient when there is unbalance between generation and demand. The inertia is small to emulate a critical situation with a weak grid. The load is represented as a resistor, calculated to match the turbine nominal power. Due to the short time span of the simulation, the wind generation is assumed constant. Even though a Type IV turbine is simulated, the discussion is also applicable to Type III turbines, and the same overall behavior is expected.

The parameters of the control system are given in Table 6.2.

A 50% load increase is the event that triggers the simulated transient situation. Since the WT is already generating its rated power and the wind conditions are unchanged, this unbalance leads to a grid frequency drop. As it decreases, the synthetic inertia control detects the frequency reduction below the threshold and activates, increasing the WT's output power. Three different cases are simulated, varying the GSC type and the Synthetic Inertia behavior:

- Case 1: GFL-based GSC; SSC with the described synthetic inertia control;
- Case 2: GFL-based GSC; SSC with a modified synthetic inertia control (output power ramp increased from 0.8 to 8.0 p.u./Hz·s);
- Case 3: HCC-based GSC; SSC with the described synthetic inertia control.

For all cases, the following events happen in quick succession:

Table 6.1: Electrical system parameters for the simulation of the HCC applied to a wind turbine.

Component	Parameter	Value
Transmission Line (TL)	R	3.6 Ω
	L	60.8 mH
Substation Transformer (TF1)	R	0.9 Ω
	L	100.2 mH
	V	230/34.5 kV
Medium-Voltage Distribution Network (MVDN)	R	36.3 mΩ
	L	0.1 mH
Turbine Transformer (TF2)	R	1.9 Ω
	L	46.1 mH
	V	34.5/0.69 kV
WT PEC Filter	R	0.7 $m\Omega$
	L	20.0 μH
Wind Turbine	P_{nom}	5.0 MW
	C_{dc}	250.0 mF
Load	R	10.6 kΩ
Grid	H	0.1 s
	$k_{droop,p}$	2.5 MW/Hz

Table 6.2: Control system parameters for the simulation of the HCC applied to a wind turbine.

Component	Parameter	Value
GFL- and GFM-parts Current Loop	$k_{p,i}$	33.3 mV/A
	$T_{i,i}$	26.6 ms
GFM-part Voltage Loop	$k_{p,v}$	33.3 μA/V
	$T_{i,v}$	0.1 s
GFL-part dc Voltage Loop	$k_{p,vdc}$	0.1 kW/V
	$T_{i,vdc}$	10.0 ms
GFL-part dc Voltage Droop	$k_{drp,vdc}$	5.3 V/kW
	T_{LPF}	0.1 ms
GFM-part Frequency PI controller	$k_{p,f}$	1.0 mHz/MW
	$T_{i,f}$	1.0 s

1. The load increases at simulation time $t = 2.0s$;
2. The WT's generated power is unchanged, since it only depends on the wind conditions;
3. The grid supplies the load, increasing its own output active power, which leads

to a frequency drop.

Results are shown in Figure 6.10. First, a comparison between cases 1 and 2 shows that, even though the synthetic inertia control ramps up more quickly in case 2, the resulting initial frequency drop and RoCoF are essentially equal. This is due to the fact that, for the synthetic inertia to activate and increase the active power delivered to the grid, it relies on a PLL measuring the grid frequency, which adds delay to the converter's response. The synthetic inertia control also only triggers after the grid frequency has already dropped below the activation threshold, which also delays the response time. In summary, when the frequency starts to decrease, what happens (following the initial events) is:

4. A PLL detects the frequency decreasing below the minimum threshold;
5. The RSC starts increasing the power injected in the dc link;
6. The GSC starts increasing the power delivered to the grid to keep the dc link at the nominal voltage;
7. A point of equilibrium is reached when the grid frequency is stable at around 59.2 Hz.

Then, a comparison between cases 1 and 3 shows that the HCC-based GSC from case 3 clearly provides better grid support. The frequency dip and RoCoF are reduced because the GFM-part of the GSC starts delivering power from the dc link to the grid right at the first moments of the fault. The secondary frequency dip in case 3 corresponds to the moment when the GFL-part of the HCC starts consuming power from the grid to restore the dc-link voltage, before the synthetic inertia kicks in. The GFM-part of the GSC supports the grid in the first moments, holding the line while the extra power from the SI control is starting to ramp up. What happens in case 3 when the load increases (following the initial events) is:

4. The GFM-part of the GSC automatically provides support, increasing the power delivered to the grid;
5. With the increase in delivered power, the dc-link voltage decreases;
6. The GFL-part of the GSC detects the decrease in the dc-link voltage and starts consuming power from the grid, leading to a secondary frequency dip;
7. A PLL detects the frequency decreasing below the minimum threshold;
8. The RSC starts increasing the power injected in the dc link;

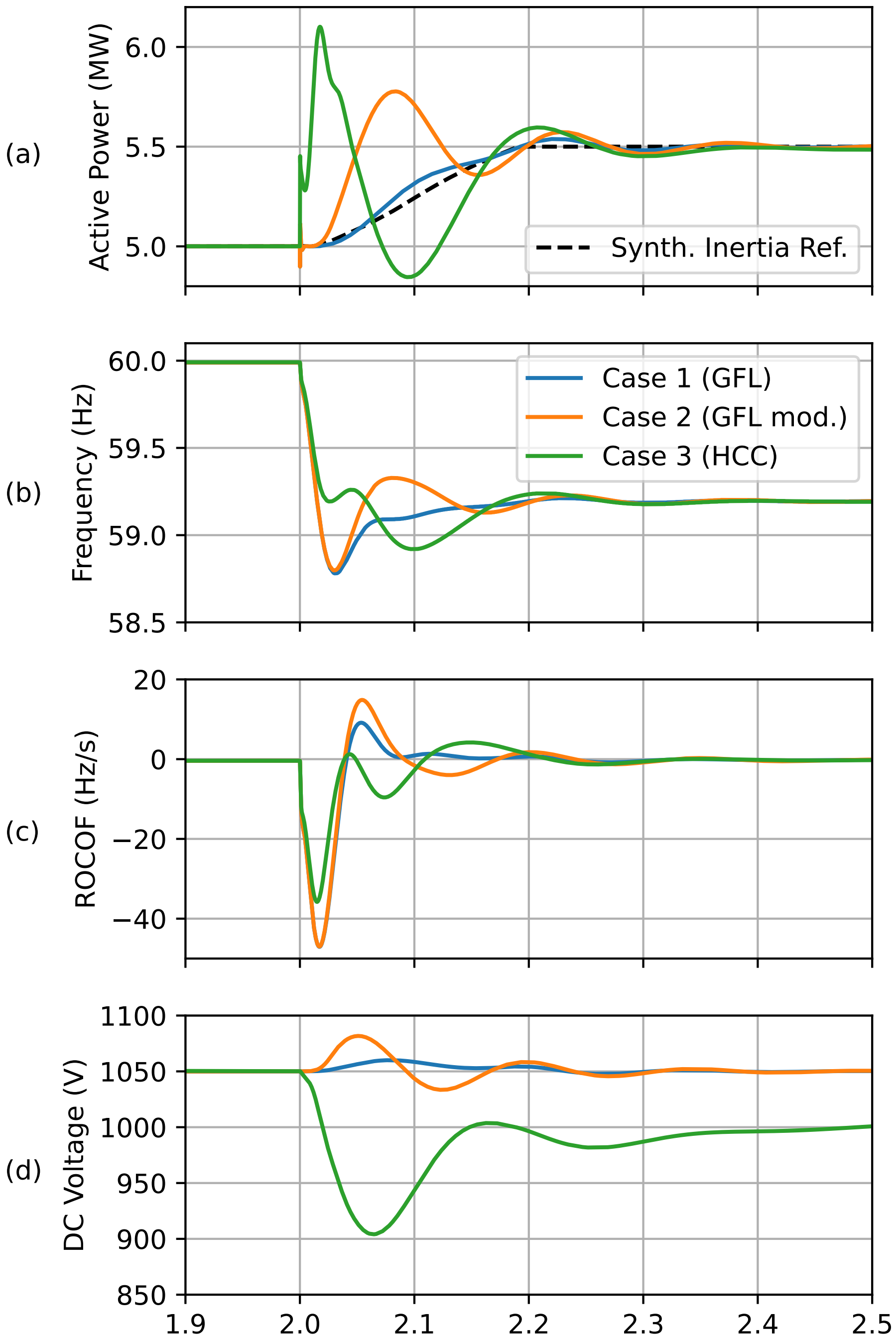

Figure 6.10: Results of the synthetic inertia simulation: (a) WT's GSC output power, (b) grid frequency, (c) RoCoF and (d) dc-link voltage.

9. The GFL-part of the GSC starts increasing the power delivered to the grid to keep the dc link at the reference voltage;
10. The GFM-part of the GSC starts reducing its output power due to the integral action of its droop PI controller;
11. A point of equilibrium is reached where the grid frequency is stable at around 59.2 Hz.

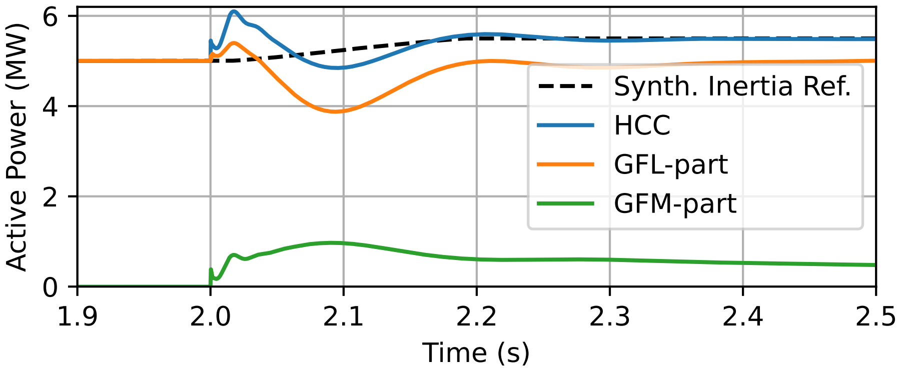

Figure 6.11: Output power of the HCC and its 2 subsystems in the synthetic inertia simulation.

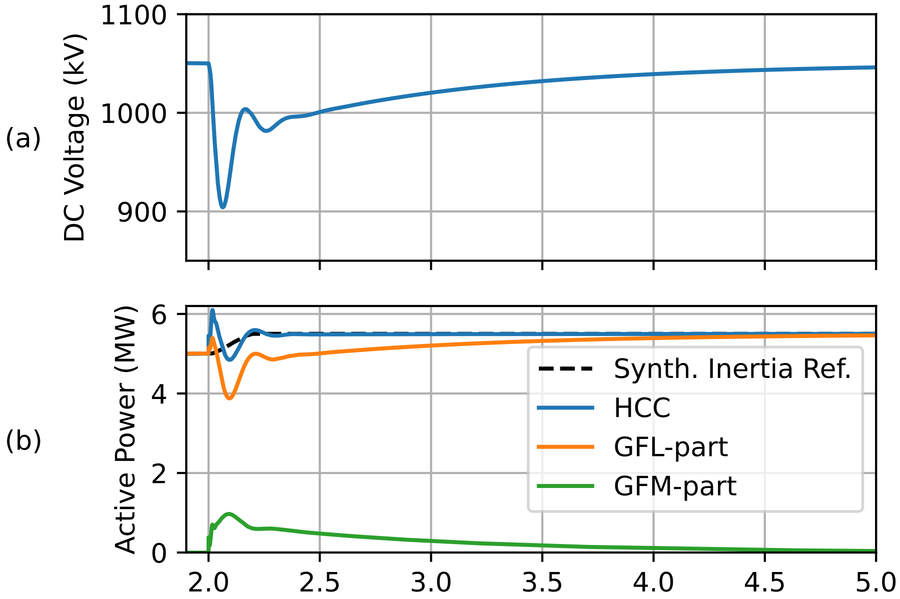

Figure 6.12: Behavior of the HCC-based GSC after the initial transient: (a) output power and (b) dc-link voltage.

Figure 6.11 shows the total HCC output power and the individual power coming from its GFL- and GFM-parts, illustrating these events.

It is worth noting that the active power delivered by the GFM-part returns to zero after a while, due to the modification applied to its droops. This also restores the GFL-part's dc voltage reference to the original nominal value, as shown in Figure 6.12.

The amount of support the GFM-part of the GSC can supply depends on the amount of energy it can deliver to the grid, from the dc link, quickly. Usual dc-link capacitors are not designed for this purpose, meaning they have a very small amount of stored energy. This leads to limited support capability by the HCC-based GSC, since the dc-link voltage is not allowed to drop very much from its nominal value. If there were an energy storage device in the dc link, such as a supercapacitor or a

BESS, it could provide the extra energy required by the HCC-based GSC without excessively reducing the dc-link voltage, resulting in even better performance in terms of frequency nadir and RoCoF.

Another observation is that the HCC could also be applied to the RSC of DFIG turbines (loosely based on Rodriguez-Amenedo et al. [24]), since the RSC is indirectly coupled to the grid because it controls the power in the stator and rotor circuits. If both converters of the DFIG are HCC, it could enable extra power delivery during the first moments of a fault from the rotor and from the stator circuits. This can be relevant since the GSC is rated at around 30% nominal power for DFIGs, limiting its maximum grid support capability. This study is a topic of interest, and is listed as a *Future Work* in Chapter 8.

6.4 Partial Conclusion

This chapter described the main characteristics of a wind turbine. The two main types of wind turbine currently in use, Types III and IV, employ back-to-back converters, where the Rotor-Side Converter (or Stator-Side Converter) controls the generated power according to an MPPT algorithm, and the Grid-Side Converter delivers that power to the grid, keeping the dc-link voltage stable. Both are implemented as GFL in order to accurately control the output power or current in their own way.

Since their output power is controlled by converters and decoupled from the grid conditions, WTs do not provide grid support, which may lead to larger oscillations and lower reliability for grids with high penetration of renewable sources. Extra control loops, such as Synthetic Inertia, can help mitigate this problem. Nevertheless, since WT converters are GFL, the grid stability issue may persist due to their response delay.

To provide WTs with a better grid support capability, the proposal is to change the GSC from GFL to HCC. With minor adjustments to the HCC control system, it can provide accurate power control (as usual), ensuring the turbine generates maximum power in steady-state, and also improve the WT's grid support during transient situations.

Overall, it can be seen that the HCC improves the WT's frequency support capability due to its GFM-part, which presents an almost-instantaneous response to the frequency transient. Even if the RSC/SSC's Synthetic Inertia control is "accelerated", it still provides a slower response than the HCC due to the fact that it is based on a PLL detecting the grid frequency drop. The level of improvement of the frequency nadir depends, to some extent, on the grid characteristics (impedances, inertia, etc.) and on the control system gains. Nevertheless, results show that the main advantage comes from the different behavior of the HCC control system when compared to the regular GFL.

Chapter 7

Applying the Hybrid Control Converter to Multiterminal HVDC Transmission Systems

This chapter presents the main concepts related to High-Voltage Direct Current transmission systems. The usual way in which power converters are employed is presented, along with the limitations that arise from this strategy.

An application of the HCC with HVDC systems is proposed. Simulation results show that the electrical grid benefits from employing HCCs instead of a regular GFL or GFM converter, presenting distributed grid support capability.

7.1 HVDC Transmission Basic Concept

Even though most transmission systems in the world employ the classic ac technology, dc transmission systems have been gaining strength in the past years [76]. Their main advantage is that they are more compact and have lower losses than ac systems [77], which leads to cost reduction. On the other hand, they require expensive converter stations in every point where an interface with an ac grid is required. Combining these two aspects, dc transmission systems tend to be more cost-effective than ac particularly for long distances [77], as the reduced losses become a larger overall cost savings factor.

Renewable generation, such as wind, solar or hydro (especially with run-of-river plants), depend entirely on the availability of natural resources and may also require large amounts of space. Because of these factors, many renewable generation power plants are not installed close to the consumption centers, but elsewhere, where the necessary natural resource is more abundant, requiring extensive transmission networks. HVDC transmission can be the solution for this issue, and current HVDC projects are used either to connect far away generation to the consumption centers or to connect offshore wind generation to the electrical grid via compact submarine cables [37].

Most HVDC transmission systems are implemented as point-to-point. They consist on a dc transmission line, also called dc link or HVDC link, which has a converter on each of its terminals, as shown in Figure 7.1. Usually, one of the terminals is connected to a large generation facility, such as a large hydro power plant or an offshore wind farm, in its own small, islanded ac grid. The other terminal is connected to the main ac grid, closer to the main consumption centers.

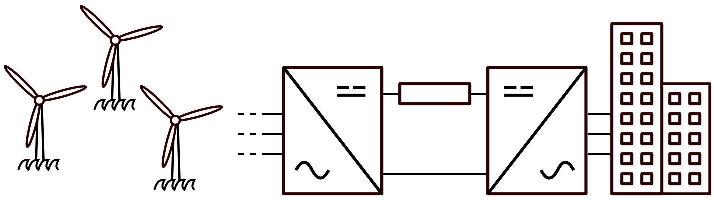

Figure 7.1: Schematic of a basic point-to-point HVDC transmission system.

Historically, the converters used with HVDC systems have been thyristor-based Line Commutated Converters (LCC). Thyristors are robust semiconductor switches that have high voltage and current ratings, which makes them particularly useful for very-high-power applications. In these cases, the converter at the generation-side of the HVDC link is controlled so that the active power flowing into the dc link matches the generated power. Therefore, as the grid operator decides the setpoint of the generation units, the reference power of the converter is adjusted accordingly. The converter at the demand-side is set to control the dc-link voltage, keeping it at the nominal level. Therefore, the amount of power that flows through it is a consequence of the amount of power flowing into the HVDC-link through the generation-side converter.

With improvements in semiconductor materials and manufacturing processes, it became possible to employ VSCs in the terminals of HVDC links. VSCs usually employ IGBTs, which have a lower voltage and current rating than thyristors. To enable a converter with higher total rating, the converter is usually implemented with an MMC topology. VSCs create lower harmonic content than LCCs, requiring smaller filters. They can also be controlled as GFM, to form the ac grid, unlike LCCs. VSC-based HVDC links can be employed, for example, with offshore wind farms. In this case, the offshore-side converter acts as a GFM, creating the ac grid to which the wind turbines are connected. This leads to an automatic power flow from the wind turbines into the HVDC link, as the converter works to maintain nominal values of grid voltage and frequency. The continent-side converter acts as a GFL, controlling the dc voltage around its nominal value. As with the LCC, the power flowing through this converter is a consequence of the power flowing into the dc link through the offshore-side converter.

7.2 Challenges and Limitations

Because of the way they are implemented, HVDC links create a complete severance between the ac systems connected to each of their terminals. The terminal that controls the dc voltage (demand-side converter) is completely insensitive to the state of the ac grid. Since the control target is only the dc voltage, the ac voltage and frequency do not affect the converter output power, which means that the converter does not provide any kind of grid support. The only way in which the converter output power changes is when the power flowing into the HVDC link through the generation-side converter changes. Therefore, some kind of communication between the two terminals of the HVDC transmission line would be required in order to provide grid support capabilities to the converter at the demand-side of the HVDC link.

Any kind of communication system, be it via satellite or optic cables, would introduce delay and reliability issues in the control system. Because of this, the grid supporting capabilities of the HVDC link suffer from the same limitations as those from a generator connected to the grid via a GFL. In fact, the demand-side converter of an HVDC link usually operates as GFL. This means that it would be slow to provide support, since measurements of grid voltage and/or frequency would need to be taken, processed and relayed to the control system for it to take action.

Another issue is that, since the terminals of the HVDC link have different control systems with different targets, HVDC transmission systems are usually unidirectional. They can be bidirectional if one of the terminals is directly controlling the power flowing into/out of the HVDC-link, but this also means that a system operator must change the operational setpoint to define the power flow. Based on electrical studies and expected levels of generation in the different subsystems of the electrical grid, during the day, the operator can define the power setpoint of the HVDC link to control the power flowing into or out of a given subsystem. Since this logic is reliant on electrical studies and on the actual generation and demand levels of the grid compared to the operator's expectation, this makes the system more prone to error, being also more difficult to ensure an optimal operating point of the overall electrical grid.

To make a proper comparison between ac and dc transmission systems, it is important to understand how the electrical power flows through an ac network. Except from generators and loads, ac grids are mainly comprised by passive elements, such as transmission lines and transformers. Controllable elements such as capacitor and inductor banks, On-Load Tap Changer (OLTC) transformers, and STATCOMs, are usually employed mainly to keep the voltage level close to the nominal value along the grid, avoiding large increases or drops on specific regions. They do not affect too much the active power flow in the network. During regular operation, if there is a sudden increase in load on a given node or region "A", its frequency and voltage will drop. As a result, existing sources in other electrical nodes (or regions) connected to A will automatically provide power to it. As the frequency of A decreases, its phase angle starts to lag, and thus active power naturally flows to A from other connected regions due to the difference in phase angle on the TL impedances. This behavior is natural; there is no control or actuator enforcing some command stating "*all regions must increase power flow to A*". Of course there is the frequency response control of some generators that act when transients occur, but the instantaneous redistribution of power inside the grid, from the regions that have more generation to the regions that have less, is autonomous and natural.

As mentioned before, HVDC transmission is more advantageous than classical ac for large amounts of power and longer distances, which could make it the prime choice for expanding the transmission system. Nevertheless, they present limited grid support capabilities, and increase the operational complexity of the electrical grid, especially if there are multiple HVDC-links with setpoints to be defined and monitored by the system operators. ac grids are much easier to operate, since power is naturally and passively redistributed.

7.3 Proposed Application

A solution that imbues an HVDC transmission system with the main advantages of ac transmission could be very useful for the expansion of electrical grids. The lower costs from dc could be achieved while maintaining the automatic power distribution and grid support of ac transmission. The multiterminal dc transmission system would automatically adjust the power flow in the dc lines to supply whichever of its terminals needed it the most, while still controlling the dc voltage around its nominal value. Like ac grids, it would be easily expandable and it would not require complex coordination with the grid operator.

To achieve this goal, all of the HVDC terminals must have the same, independent control logic. Usually, one specific converter must control the dc voltage (much like a swing bar in ac power system studies), which leads to poor grid support capability and possibly the need for an operator to define the power setpoint elsewhere. If all terminals must have the same behavior and control system, this means that they must, simultaneously, deal with the dc voltage balance and adjust the power flow based on the ac grid state. Controlling the dc voltage is achieved by controlling the converter power, which is precisely how a GFL works. Adjusting the behavior according the the ac grid state is the same as providing grid support, which is the strong point of a GFM. By employing an HCC, both of these characteristics can be achieved at once, at all of the HVDC terminals.

To better explain the concept behind the proposed application, a multiterminal HVDC system connecting four ac grids is used as example, as shown in Figure 7.2. In this case, the four HVDC terminals employ the HCC, with the same control system.

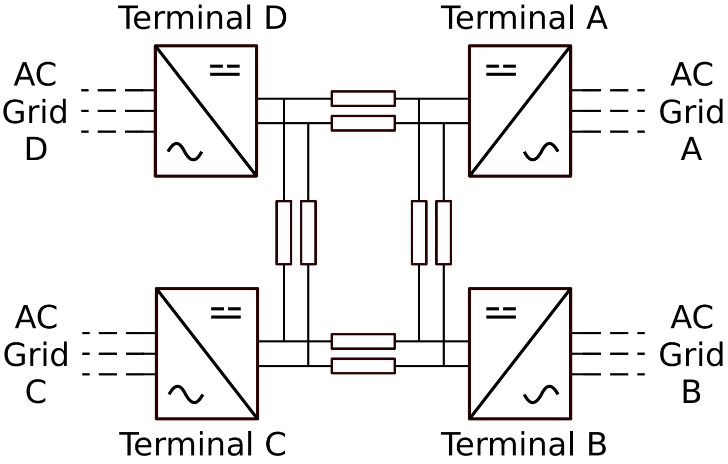

Figure 7.2: Example system including ac systems and a dc transmission system.

The GFM-part of the HCC is employed as described in previous chapters, with reference values of active and reactive power set to zero. When the ac system connected to a given terminal undergoes any oscillation, the GFM-part of the HVDC terminal automatically acts to provide support. If the ac frequency drops, the GFM-part active power increases to help mitigate the transient, and vice-versa, following the usual GFM behavior. Meanwhile, the GFL-part acts to keep the dc voltage close to its reference value.

The GFL-part of the HCC needs one adjustment. If it simply controls the dc voltage to stay at its nominal value, this would mean that all nodes in the dc system would have the same voltage, and therefore no power flow happens. To enable different values of dc voltage at the different dc nodes, a droop is introduced in the GFL-part of each terminal. It adjusts the reference dc voltage value proportionally to the active power of its GFM-part, similarly to the one described in Chapter 6. The idea is: if the ac system connected to a given terminal has a frequency drop, the GFM-part of the HCC increases the active power delivered to it. For this to happen, the dc voltage of this terminal must be lower than the others, so that power can flow from the other nodes of the dc system into it. With the droop that adjusts the dc voltage reference of the GFL-part of the HCC, this behavior is achieved.

Table 7.1: Simulated dc system electrical and control parameters.

Component	Parameter	Value
Rated dc Voltage	$V_{dc,nom}$	± 200.0 kV
Rated Power	$p_{dc,nom}$	100.0 MW
dc lines A-B / B-C / C-D / D-A	R_{TL} L_{TL} C_{TL}	3.0 / 4.4 / 3.7 / 1.5 Ω 34.1 / 51.2 / 42.7 / 17.1 mH 49.2 / 73.9 / 61.7 / 24.7 μF
Converter Capacitance	C_{conv}	40 μF
HVDC Terminals PEC Filter	R_f L_f	4.2 $m\Omega$ 0.1 H
GFL- and GFM-parts Current Loop	$k_{p,i}$ $T_{i,i}$	18.5 V/A 26.5 ms
GFM-part Voltage Loop	$k_{p,v}$ $T_{i,v}$	0.6 A/V 0.1 s
GFL-part dc Voltage Loop	$k_{p,vdc}$ $T_{i,vdc}$	0.6 kW/V 10.0 ms
GFL-part dc Voltage Droop	$k_{drp,vdc}$ T_{LPF}	0.8 V/kW 0.1 ms
GFM-part Frequency Droop	$k_{drp,f}$	50.0 mHz/MW

7.4 Results

A simulation is set up consisting of four separate ac systems (named A, B, C, D), interconnected by a meshed HVDC transmission system, as shown in Figure 7.2. For simplicity, each ac system has the same topology and parameters as shown in Figure 6.9 and described in Table 6.1. An adaptation is that, instead of a single WT, each ac system has a small wind farm with 10 WTs, resulting in a total maximum generation of 50 MW. The load is scaled accordingly. No synthetic inertia control is present in this scenario, and the WTs generated power is again assumed constant. The HVDC system is connected to the individual ac systems at the same node where their load is connected. The HVDC system parameters are adapted from [78] and described in Table 7.1, together with the control system parameters for each of its terminals. The RL filter at each HVDC terminal is adapted from [75].

At the beginning of the simulation, each ac system has generation and load set to their nominal value of 50.0 MW. Then, at simulation time $t = 3s$, a step increase of 10% in the load of ac system A is applied without increase of generation. If the ac systems were connected using ac transmission lines, power would flow from the other regions to system A, and the entire system would have a small frequency decrease. If the ac systems were connected using HVDC transmission lines that follow the usual control strategies, they would be completely decoupled from each other, and only the frequency of system A would suffer a sharper decrease (unless the system operator manually changes the HVDC converter setpoints). Since the HVDC-system terminals employ the HCC, the following events happen sequentially:

1. at the beginning of the simulation, no power flow is present in the dc lines, since each ac system has a generation that matches its own load;
2. the load is increased in ac system A, resulting in a frequency drop;
3. the GFM-part of HVDC system's terminal A provides automatic support, increasing the power delivered from its dc link to ac system A;
4. since there is no power flow in the HVDC network, the extra power provided to ac system A must come from the capacitor of HVDC system's terminal A, reducing its dc voltage;
5. since the GFM-part is delivering power to the ac system, the V_{dc} reference of the GFL-part of terminal A is reduced;
6. in order to follow the reduced V_{dc} reference, the GFL-part of terminal A increases the delivered power from its dc-link to ac system A;
7. the voltage difference inside the HVDC system leads to power flow from terminals B, C, D to terminal A;
8. with power flowing through the HVDC system to terminal A, its dc voltage stabilizes, since the power supplied to ac grid A is no longer coming from its capacitor;
9. this power flow initially reduces the dc voltage of terminals B, C, D, since it comes from their dc-link capacitors stored energy;
10. the GFL-parts of terminals B, C, D sense this voltage drop and consume power from their respective ac systems to maintain their V_{dc} at the reference value;
11. this extra power consumption in ac systems B, C, D leads to a frequency decrease in each one (since their generation is unchanged);
12. the GFM-part of terminals B, C, D tries to provide support, delivering some power from their dc-link to their respective ac systems. This behavior goes against that of the GFL-part, but the net result is power flowing from ac systems B, C, D into their dc links;
13. this leads to a decrease in the V_{dc} reference for the GFL-parts of terminals B, C, D;

14. these interactions go on until a new point of equilibrium is reached;
15. in the end, a new situation of power flow is automatically established in the HVDC system, where power is drawn from the other ac systems, flowing to ac system A through the HVDC transmission lines.

These interactions are illustrated in Figure 7.3. The power delivered to ac system A increases from the moment of the load increase, as shown in Figure 7.3a, which is the expected behavior of the HCC. The resulting power flow in the HVDC transmission lines is shown in Figure 7.3b. The power coming from terminal C splits into the two transmission lines, going from C to B and D; there, it merges with the power coming from these terminals and finally goes to terminal A.

The power each terminal provides to its ac system is shown in Figure 7.3c, where the plot lines for terminals B, C, D are essentially coincident. This confirms that terminal A is the only one effectively delivering power to its ac system to supply the extra load, while terminals B, C, D consume power from their ac systems to provide the necessary support to ac system A. Each one ends up providing around 1.25 MW. Since the four ac grids are represented as equivalent voltage sources with inertia and droops, the extra power to supply the increased load is provided by system A itself.

The frequency of each ac system can be seen in Figure 7.3d, where the lines for ac systems B, C, D are again very close. The figure shows that the frequency of ac systems B, C, D decreases when they start providing power to ac system A, mitigating its frequency drop. In the end, they all reach similar, but lower than nominal, values of frequency. The dc Voltage of each terminal is shown in Figure 7.3e. They are very close to each other, since this level of power transmission leads to minimal voltage drop in the dc lines.

In the end, the system naturally reaches a steady-state situation where the different ac systems operate with similar values of frequency, effectively sharing the load that was increased at ac system A and reducing its burden. Instead of a sharp frequency decrease in ac system A and no change in the others, the result is a small frequency decrease in all ac systems.

The same behavior described in this simulation can be applied for generation increases within a specific ac system connected to the dc grid. If one of them was a large offshore wind farm, for example, instead of a large transient affecting only the offshore system, variations in the wind generation would be felt and properly shared across the different ac systems connected to the dc system. This could be beneficial from a reliability standpoint, since concentrated sharper transients could lead to generator tripping and possibly load shedding.

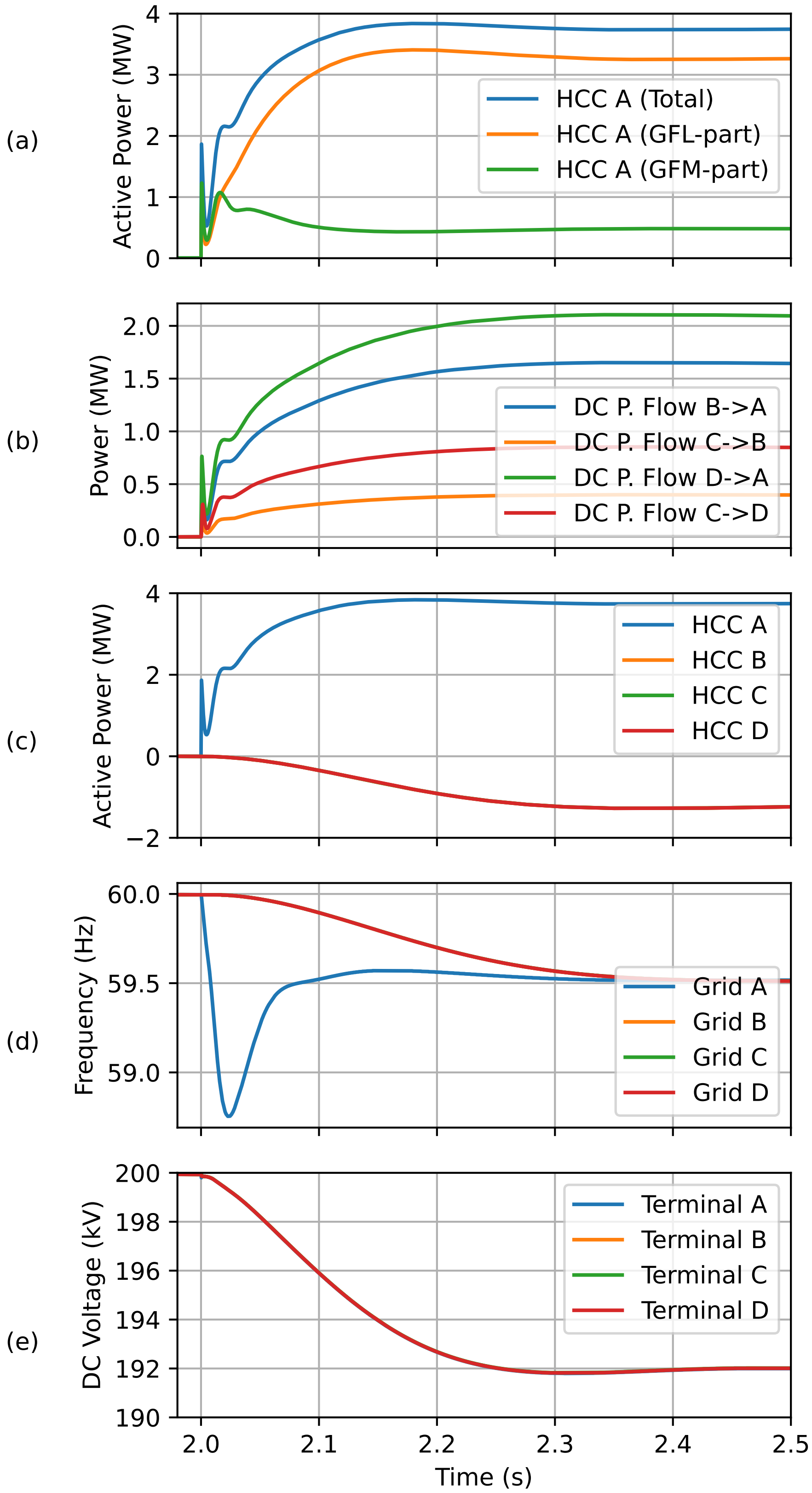

Figure 7.3: Results of the dc system simulation: (a) power delivered to ac system A through the HCC, (b) power flow in the dc lines, (c) power delivered to each individual ac system through their HCCs, (d) frequency of the individual ac systems and (e) dc voltage of each terminal.

7.5 Partial Conclusion

This chapter described the main characteristics of an HVDC transmission system and the usual behavior of its converters. Since HVDC links result in a complete decoupling of the ac systems connected to their terminals, they have limited grid-support capability. If the HCC is employed in the terminals of an HVDC grid, it can enable automatic grid support at all terminals, while also maintaining a distributed control of the dc voltage. A minor adjustment is applied to the GFL-part of the HCC, by introducing a droop in the dc voltage control loop.

Simulation results show that the HVDC grid can provide automatic and immediate grid support to the ac systems connected to its terminals by employing the HCC. When the load increases in one of the ac systems, the power flow through the dc grid automatically increases, going from the other ac systems to the one that needs it the most. No coordination with the grid operator is required, and the fast and inherent grid support capability, characteristic of the GFM, is achieved at all terminals while the GFL-part maintains the dc voltage near its nominal value value.

The fact that all terminals of the dc grid employ HCCs also implies that they all have black-start capability, which could be useful for system restoration and for islanded or off-grid systems. The proposed system is also flexible, in the sense that, if only a momentary support from the other ac systems is required and a steady-state load share is not desirable, the PI-based frequency droop used in the synthetic inertia simulation could also be employed here, to bring the active power delivered by the GFM-part of the HCCs back to zero after the transient has passed. The terminal would work as a usual GFL in steady-state, but as a GFM during transients. The GFL-part could also receive commands from the system operator and follow a given reference active power, if needed, as usual.

A deeper investigation is necessary to understand the behavior of the system in case the different ac systems are also connected with ac transmission lines, in order to avoid possible loop power flow. This is listed in chapter 8, under *Future Work*.

Chapter 8

Conclusion

8.1 Summary

The main goal of this study was to devise a new converter control scheme that could provide better grid support than standard grid-following converters equipped with support capabilities (e.g. SI control), while maintaining an accurate power tracking capability. The need for such a control system arises from the increasing penetration of converter-based renewable energy sources in the electrical grids worldwide. Since wind and solar generation are usually connected to the grid using GFLs working on MPPT mode, they are decoupled from the grid state and do not inherently provide support when a transient of voltage or frequency occurs. Due to this characteristic and to the increasing share of RESs in the power systems, grid transients are becoming more severe. Since the GFL has limited grid support capability, GFMs have been actively investigated due to their inherent grid support, even though they lack the GFL's accurate power control. A new control scheme that includes the best characteristics of both converter types would be a valuable solution.

To this end, the Hybrid Control Converter is proposed. Based on a clever application of basic electric circuit modeling techniques such as *equivalent circuits theory*, the proposed control system includes the full individual GFL and GFM control systems, along with some coupling equations. The HCC is a single converter that can emulate the behavior of two converters, a GFL and a GFM, in parallel. From the point of view of the grid, the behavior of the HCC is indistinguishable from that from a pair of individual converters working in parallel. Its dynamic response has the characteristics of the GFL, such as quick and accurate power control, as well as the ones of the GFM, such as fast and inherent grid support and black-start capabilities.

The HCC has several advantages over regular GFL or GFM converters. First, it does not require any extra hardware components, such as filters or meters, to be implemented. It can be employed with any application that already uses a converter. Since it comprises full GFL and GFM control systems, it is possible to choose their implementation and design their parameters individually, according to usual best practices and already performed studies. It does not require some trigger to change its operating mode from GFL to GFM (or vice-versa), since it is both GFL and GFM at all times, resulting in faster response times and increased reliability. If all energy sources in a grid employ the HCC, they all share the burden of grid support when a transient occurs, while maintaining classic MPPT operation in steady-state. This reduces the need for large facilities aimed at providing inertia or only primary frequency support, such as synchronous machines or energy storage systems with high power and low energy ratings (batteries, flywheels...). Nevertheless, extra dispatchable energy sources must be kept on reserve to provide secondary and tertiary frequency support.

The developed equations could be expanded following the described methodology, to make the HCC emulate any number of converters of any kind in parallel. The chosen scenario was to emulate 2 converters, one GFL and one GFM, for simplicity and to avoid redundancy. But it is possible that emulating a higher number of converters could be useful for some specific scenario.

The stability and robustness of the proposed converter were discussed, developing the system transfer functions. The analysis shows that the HCC is at least as stable and robust as usual GFL/GFM converters for the analyzed cases, which is an important aspect of any control system. Results show that, even though some usual simplifications were employed when devising this new control system, such as neglecting the switching effect, the HCC works as expected and the developed equations are valid.

Finally, two possible applications of the HCC were presented. The first one is to employ the HCC on wind turbines to improve their synthetic inertia capability. The usual implementation is that the SI control is activated when the grid frequency reaches an activation threshold. Since there is a delay in the frequency measurements and it only activates after the frequency has already fallen, this may result in a large frequency excursion in the first moments after a fault, especially in systems with low overall inertia. If the HCC is employed with the WT, simulation results show that its GFM-part is able to provide faster grid support, as expected, by consuming energy from the dc-link capacitor in the first moments of a fault. The GFL-part joins the picture a few moments later, to counteract this behavior and keep the dc voltage level close to its reference value. The result is that the WT is able to deliver increased power more quickly at the first moments after a fault, and then, when the frequency variation is detected and reaches the activation threshold, the SI control ramps up the power delivered to the grid. This leads to a scenario with a smaller RoCoF and frequency nadir when compared with the scenario with usual GFL, which could avoid the triggering of grid protection schemes such as load shedding.

The second application is with HVDC transmission systems. Usually, one of the terminals of the HVDC system is tasked with controlling the dc voltage, while the other(s) control the active power flow. By employing the HCC in the terminals of an HVDC system (point-to-point or meshed), this responsibility becomes distributed. All terminals share the burden of controlling the dc voltage, while providing fast support to the ac grids to which they are connected, much like an ac transmission system itself would. The terminals would not require setpoints definition and close control by the system operator, being fully automatic and enabling an easier expansion of the HVDC transmission system. Simulations were based on a system comprised of four individual ac networks connected by a meshed HVDC transmission system. Results show that, when a fault happens in one of the ac networks, the other ones automatically provide support, increasing the power flow through the HVDC lines. In this situation, as opposed to a large frequency drop in the ac network that suffered the fault (that could lead to instability and load shedding) and no change at the others, the result is a small (and more manageable) frequency decrease in all four ac networks.

In the end, various analyses and simulated scenarios showed that the HCC indeed presents the advantages of both the GFL and GFM at the same time, enabling accurate power control, fast grid support, black-start capability, and whatever characteristics the individual GFL/GFM control systems may present. It could be applied to a wide range of applications, such as wind turbines, solar panels, batteries, other energy storage devices, HVDC transmission systems, and essentially anything that employs a converter. The mass application of the HCC with these devices could result in distributed grid support and voltage control, enabling an electrical network with higher (or even complete) penetration of IBRs.

8.2 Future Work

The field of power electronics and converter control is vast, and many possibilities of investigation are always available. Considering the ideas developed in this work, some points that could be further investigated are listed below.

Unbalanced Conditions In some cases, the grid voltage and current may become unbalanced due to faults, general unbalance of distribution networks, or other generic reasons. It would be interesting to model the behavior of the HCC to ensure its stability under such circumstances, including the positive- and negative-sequence components of voltage and current.

Required Processing Power The HCC encompasses two full individual control systems (GFL and GFM). It could be interesting to evaluate the processing power of regular controller units, to assess if they support the HCC implementation or if a hardware upgrade would be required.

Application in the RSC on DFIG Turbines The application described in chapter 6 employs an HCC as the GSC, to improve the turbine's frequency support capability. Since the converters of the DFIG are usually of around 30% nominal power rating, the HCC is actually a limited improvement to the turbine, since it has a limited maximum capacity. The RSC controls the power in both the stator and rotor circuits of the turbine by controlling the slip and the magnetic flux vector. It can be considered an amplifier, since it controls the stator power (full power rating) even though it has only 30% power rating. Applying the HCC to both the GSC and the RSC could increase the maximum power the turbine can provide during faults, improving its support capability. The interaction of grid transients with the stator and rotor circuits, and with the RSC, could be studied to enable this application.

HVDC and Loop Flow The proposed application with HVDC systems assumed that each terminal is connected to a different ac network, for simplicity. If the terminals were connected to different nodes of the same ac system, there would be ac transmission lines in parallel with the HVDC ones, which could cause loop flow (power flowing in opposite directions in parallel lines), a phenomenon that should be avoided. Studying how to automatically identify this scenario and applying the necessary adjustments to the HCC would be the next step in this proposed application.

Offshore Wind Generation The HCC could be used to improve protection schemes of offshore wind farms. One of the possibilities of implementing an offshore wind farm is with HVDC transmission to the onshore ac grid. Usually, the offshore terminal of the dc link is a GFM, generating the offshore ac grid to which the WTs are connected, and the onshore terminal is a GFL, controlling the dc-link voltage. If a fault occurs in the onshore ac grid, its voltage drops and the power transfer capacity of the VSC is reduced [79]. While the turbines ramp down their generation, excess energy leads to an overvoltage in the dc link, which is usually taken care of by Dynamic Braking Systems (DBS) that dissipate energy. Nevertheless, the turbines need to quickly ramp down their output power. One possibility to implement this feature is by having communications between the converter stations and the turbines, changing their reference power if the onshore VSC detects a fault; this technique is challenging mainly due to the communications time delay and reliability issues. A different possibility is modify the offshore VSC control system, so it modulates the ac voltage and frequency when a dc overvoltage is detected; in this case, the WTs need extra control loops to interpret that as a signal to reduce their power output. If the dc-link is equipped with HCC on both ends, the behavior could be different. Simulation results already showed that this configuration enables the ac grids connected to the dc-link terminals to, in a way, know each other's situation and share the burden of faults. It could be an autonomous way to make the offshore ac grid aware of the problem on the onshore ac grid (since both would have their voltage and frequency affected by the fault), leading to an automatic reduction of the WTs power by means of their usual protection schemes. No communications required means increased reliability, faster response time, smaller dc overvoltage and smaller DBS required.

References

[1] "Energy Statistics Data Browser". `https://www.iea.org/data-and-statistics/data-tools/energy-statistics-data-browser`, IEA, 2022. Accessed: 2022-11-06.

[2] NGUYEN, C.-L., LEE, H.-H. "A Novel Dual-Battery Energy Storage System for Wind Power Applications", *IEEE Transactions on Industrial Electronics*, v. 63, n. 10, pp. 6136–6147, 2016. doi: 10.1109/TIE.2016.2570721.

[3] "Renewables". `https://www.iea.org/fuels-and-technologies/renewables`, IEA, 2022. Accessed: 2022-11-06.

[4] TANG, X., SUN, Y., ZHOU, G., et al. "Coordinated Control of Multi-Type Energy Storage for Wind Power Fluctuation Suppression", *Energies*, v. 10, n. 8, 2017. ISSN: 1996-1073. doi: 10.3390/en10081212.

[5] ZHAO, H., WU, Q., HU, S., et al. "Review of energy storage system for wind power integration support", *Applied Energy*, v. 137, pp. 545–553, 2015. ISSN: 0306-2619. doi: https://doi.org/10.1016/j.apenergy.2014.04.103.

[6] KNAP, V., CHAUDHARY, S. K., STROE, D.-I., et al. "Sizing of an Energy Storage System for Grid Inertial Response and Primary Frequency Reserve", *IEEE Transactions on Power Systems*, v. 31, n. 5, pp. 3447–3456, 2016. doi: 10.1109/TPWRS.2015.2503565.

[7] PENG, J., MENG, J., WANG, Y., et al. "Research on Virtual Synchronous Generator Control Strategy Based on the Battery State of Charge". In: *2019 IEEE Innovative Smart Grid Technologies - Asia (ISGT Asia)*, pp. 2016–2020, 2019. doi: 10.1109/ISGT-Asia.2019.8881139.

[8] LIU, R., WANG, Z., XING, H. "Virtual Inertia Control Strategy for Battery Energy Storage System in Wind Farm". In: *2019 IEEE PES Asia-Pacific Power and Energy Engineering Conference (APPEEC)*, pp. 1–5, 2019. doi: 10.1109/APPEEC45492.2019.8994353.

[9] WANG, B., CAI, G., YANG, D. "Dispatching of a Wind Farm Incorporated With Dual-Battery Energy Storage System Using Model Predictive Control", *IEEE Access*, v. 8, pp. 144442–144452, 2020. doi: 10.1109/ACCESS.2020.3014214.

[10] MATEVOSYAN, J., BADRZADEH, B., PREVOST, T., et al. "Grid-Forming Inverters: Are They the Key for High Renewable Penetration?" *IEEE Power and Energy Magazine*, v. 17, n. 6, pp. 89–98, 2019. doi: 10.1109/MPE.2019.2933072.

[11] SU, Y., LI, H., CUI, Y., et al. "An Adaptive PV Frequency Control Strategy Based on Real-Time Inertia Estimation", *IEEE Transactions on Smart Grid*, v. 12, n. 3, pp. 2355–2364, 2021. doi: 10.1109/TSG.2020.3045626.

[12] GAO, Q., PREECE, R. "Improving frequency stability in low inertia power systems using synthetic inertia from wind turbines". In: *2017 IEEE Manchester PowerTech*, pp. 1–6, 2017. doi: 10.1109/PTC.2017.7980836.

[13] KHATAMIANFAR, A., KHALID, M., SAVKIN, A. V., et al. "Improving Wind Farm Dispatch in the Australian Electricity Market With Battery Energy Storage Using Model Predictive Control", *IEEE Transactions on Sustainable Energy*, v. 4, n. 3, pp. 745–755, 2013. doi: 10.1109/TSTE.2013.2245427.

[14] TAN, J., ZHANG, Y. "Coordinated Control Strategy of a Battery Energy Storage System to Support a Wind Power Plant Providing Multi-Timescale Frequency Ancillary Services", *IEEE Transactions on Sustainable Energy*, v. 8, n. 3, pp. 1140–1153, 2017. doi: 10.1109/TSTE.2017.2663334.

[15] ROCABERT, J., LUNA, A., BLAABJERG, F., et al. "Control of Power Converters in AC Microgrids", *IEEE Transactions on Power Electronics*, v. 27, n. 11, pp. 4734–4749, 2012. doi: 10.1109/TPEL.2012.2199334.

[16] ROSSO, R., WANG, X., LISERRE, M., et al. "Grid-Forming Converters: Control Approaches, Grid-Synchronization, and Future Trends-A Review", *IEEE Open Journal of Industry Applications*, v. 2, pp. 93–109, 2021. doi: 10.1109/OJIA.2021.3074028.

[17] TAUL, M. G., WU, C., CHOU, S.-F., et al. "Optimal Controller Design for Transient Stability Enhancement of Grid-Following Converters Under Weak-Grid Conditions", *IEEE Transactions on Power Electronics*, v. 36, n. 9, pp. 10251–10264, 2021. doi: 10.1109/TPEL.2021.3066205.

[18] HUANG, L., WU, C., ZHOU, D., et al. “A Double-PLLs-Based Impedance Reshaping Method for Extending Stability Range of Grid-Following Inverter Under Weak Grid”, *IEEE Transactions on Power Electronics*, v. 37, n. 4, pp. 4091–4104, 2022. doi: 10.1109/TPEL.2021.3127644.

[19] ZOU, Z., BESHELI, B. D., ROSSO, R., et al. “Interactions Between Two Phase-Locked Loop Synchronized Grid Converters”, *IEEE Transactions on Industry Applications*, v. 57, n. 4, pp. 3935–3947, 2021. doi: 10.1109/TIA.2021.3081611.

[20] LASSETER, R. H., CHEN, Z., PATTABIRAMAN, D. “Grid-Forming Inverters: A Critical Asset for the Power Grid”, *IEEE Journal of Emerging and Selected Topics in Power Electronics*, v. 8, n. 2, pp. 925–935, 2020. doi: 10.1109/JESTPE.2019.2959271.

[21] WU, D., TANG, F., DRAGICEVIC, T., et al. “Autonomous Active Power Control for Islanded AC Microgrids With Photovoltaic Generation and Energy Storage System”, *IEEE Transactions on Energy Conversion*, v. 29, n. 4, pp. 882–892, 2014. doi: 10.1109/TEC.2014.2358612.

[22] MA, Y., CAO, W., YANG, L., et al. “Virtual Synchronous Generator Control of Full Converter Wind Turbines With Short-Term Energy Storage”, *IEEE Transactions on Industrial Electronics*, v. 64, n. 11, pp. 8821–8831, 2017. doi: 10.1109/TIE.2017.2694347.

[23] YU, Y., CHAUDHARY, S. K., GOLESTAN, S., et al. “An Overview of Grid-Forming Control for Wind Turbine Converters”. In: *IECON 2021 – 47th Annual Conference of the IEEE Industrial Electronics Society*, pp. 1–6, 2021. doi: 10.1109/IECON48115.2021.9589838.

[24] RODRÍGUEZ-AMENEDO, J. L., GÓMEZ, S. A., MARTÍNEZ, J. C., et al. “Black-Start Capability of DFIG Wind Turbines Through a Grid-Forming Control Based on the Rotor Flux Orientation”, *IEEE Access*, v. 9, pp. 142910–142924, 2021. doi: 10.1109/ACCESS.2021.3120478.

[25] ALASSI, A., AHMED, K., EGEA-ALVAREZ, A., et al. “Performance Evaluation of Four Grid-Forming Control Techniques with Soft Black-Start Capabilities”. In: *2020 9th International Conference on Renewable Energy Research and Application (ICRERA)*, pp. 221–226, 2020. doi: 10.1109/ICRERA49962.2020.9242758.

[26] ZHAO, Z., SUN, Z., FENG, Y., et al. “High-Performance Resonant Controller Implemented in the Discrete-Time Domain for Voltage Regulation of Grid-

Forming Converters", *IEEE Transactions on Power Electronics*, v. 37, n. 4, pp. 3913–3926, 2022. doi: 10.1109/TPEL.2021.3120426.

[27] TAYYEBI, A., GROSS, D., ANTA, A., et al. "Frequency Stability of Synchronous Machines and Grid-Forming Power Converters", *IEEE Journal of Emerging and Selected Topics in Power Electronics*, v. 8, n. 2, pp. 1004–1018, 2020. doi: 10.1109/JESTPE.2020.2966524.

[28] LIU, T., WANG, X., LIU, F., et al. "A Current Limiting Method for Single-Loop Voltage-Magnitude Controlled Grid-Forming Converters During Symmetrical Faults", *IEEE Transactions on Power Electronics*, v. 37, n. 4, pp. 4751–4763, 2022. doi: 10.1109/TPEL.2021.3122744.

[29] LAI, N. B., BALTAS, G. N., RODRIGUEZ, P. "Multi-Rotor Virtual Machine for Grid-Forming Converter to Damp Sub-Synchronous Resonances", *IEEE Access*, v. 9, pp. 128178–128187, 2021. doi: 10.1109/ACCESS.2021.3112070.

[30] LI, M., WANG, Y., HU, W., et al. "Unified Modeling and Analysis of Dynamic Power Coupling for Grid-Forming Converters", *IEEE Transactions on Power Electronics*, v. 37, n. 2, pp. 2321–2337, 2022. doi: 10.1109/TPEL.2021.3107329.

[31] JIN, Z., WANG, X. "A DQ-Frame Asymmetrical Virtual Impedance Control for Enhancing Transient Stability of Grid-Forming Inverters", *IEEE Transactions on Power Electronics*, v. 37, n. 4, pp. 4535–4544, 2022. doi: 10.1109/TPEL.2021.3124286.

[32] SAMANTA, S., CHAUDHURI, N. R. "Stability Analysis of Grid-Forming Converters under dc-side Current Limitation in Primary Frequency Response Regime", *IEEE Transactions on Power Systems*, pp. 1–1, 2021. doi: 10.1109/TPWRS.2021.3130226.

[33] CAMACHO, A., CASTILLA, M., MIRET, J., et al. "Positive and Negative Sequence Control Strategies to Maximize the Voltage Support in Resistive–Inductive Grids During Grid Faults", *IEEE Transactions on Power Electronics*, v. 33, n. 6, pp. 5362–5373, 2018. doi: 10.1109/TPEL.2017.2732452.

[34] LU, D., ZHU, J., WANG, J., et al. "A Simple Zero-Sequence-Voltage-Based Cluster Voltage Balancing Control and the Negative Sequence Current

Compensation Region Identification for Star-Connected Cascaded H-Bridge STATCOM", *IEEE Transactions on Power Electronics*, v. 33, n. 10, pp. 8376–8387, 2018. doi: 10.1109/TPEL.2017.2785239.

[35] KIM, H., BHATTACHARYA, S. "A Novel Current Control Strategy Based on Harmonic Voltage Injection for Power Losses Reduction of PMSMs with Non-Sinusoidal Back-EMF". In: *2019 IEEE Industry Applications Society Annual Meeting*, pp. 1–6, 2019. doi: 10.1109/IAS.2019.8912372.

[36] CHEN, J., LI, W., HE, J., et al. "Harmonic Suppression Scheme of L-type New Energy Grid-connected Inverter Based on Harmonic Injection Method". In: *2019 IEEE 8th International Conference on Advanced Power System Automation and Protection (APAP)*, pp. 36–39, 2019. doi: 10.1109/APAP47170.2019.9224898.

[37] RODRÍGUEZ-AMENEDO, J. L., ARNALTES-GÓMEZ, S., ARAGÜÉS-PEÑALBA, M., et al. "Control of the Parallel Operation of VSC-HVDC Links Connected to an Offshore Wind Farm", *IEEE Transactions on Power Delivery*, v. 34, n. 1, pp. 32–41, 2019. doi: 10.1109/TPWRD.2018.2841908.

[38] GUO, Z. "A harmonic current injection control scheme for active islanding detection of grid-connected inverters". In: *2015 IEEE International Telecommunications Energy Conference (INTELEC)*, pp. 1–5, 2015. doi: 10.1109/INTLEC.2015.7572482.

[39] HARNEFORS, L., KUKKOLA, J., ROUTIMO, M., et al. "A Universal Controller for Grid-Connected Voltage-Source Converters", *IEEE Journal of Emerging and Selected Topics in Power Electronics*, v. 9, n. 5, pp. 5761–5770, 2021. doi: 10.1109/JESTPE.2020.3039407.

[40] LIMA, L. A. M., WATANABE, E. H. "Hybrid Control Scheme for VSC Presenting Both Grid-Forming and Grid-Following Capabilities", *IEEE Transactions on Power Delivery*, , n. 6, pp. 4570–4581, 2022. doi: 10.1109/TPWRD.2022.3151715.

[41] TEODORESCU, R., LISERRE, M., RODRIGUEZ, P. *Grid Converters for Photovoltaic and Wind Power Systems.* Chichester, West Sussex, United Kingdom, John Wiley and Sons Ltd, 2011.

[42] ARTEAGA, M. U., RUIZ, A. G., RIVERA, M. "Control of Energy Storage and Photovoltaic Systems using Model Predictive Control". In: *2019 Inter-*

national Conference on Smart Energy Systems and Technologies (SEST), pp. 1–6, 2019. doi: 10.1109/SEST.2019.8849099.

[43] FLOURENTZOU, N., AGELIDIS, V. G., DEMETRIADES, G. D. "VSC-Based HVDC Power Transmission Systems: An Overview", *IEEE Transactions on Power Electronics*, v. 24, n. 3, pp. 592–602, 2009. doi: 10.1109/TPEL.2008.2008441.

[44] BOSE, B. K. *Modern Power Electronics and AC Drives.* Upper Saddle River, NJ, United States of America, Prentice Hall, 2002.

[45] NABAE, A., TAKAHASHI, I., AKAGI, H. "A New Neutral-Point-Clamped PWM Inverter", *IEEE Transactions on Industry Applications*, v. IA-17, n. 5, pp. 518–523, 1981. doi: 10.1109/TIA.1981.4503992.

[46] LESNICAR, A., MARQUARDT, R. "An innovative modular multilevel converter topology suitable for a wide power range". In: *2003 IEEE Bologna Power Tech Conference Proceedings,*, v. 3, pp. 6 pp. Vol.3–, 2003. doi: 10.1109/PTC.2003.1304403.

[47] ESRAM, T., CHAPMAN, P. L. "Comparison of Photovoltaic Array Maximum Power Point Tracking Techniques", *IEEE Transactions on Energy Conversion*, v. 22, n. 2, pp. 439–449, 2007. doi: 10.1109/TEC.2006.874230.

[48] DE BRABANDERE, K., BOLSENS, B., VAN DEN KEYBUS, J., et al. "A Voltage and Frequency Droop Control Method for Parallel Inverters", *IEEE Transactions on Power Electronics*, v. 22, n. 4, pp. 1107–1115, 2007. doi: 10.1109/TPEL.2007.900456.

[49] PARK, R. "Two Reaction Theory of Synchronous Machines", *AIEE Transactions*, v. 48, pp. 716–730, 1929.

[50] AKAGI, H., WATANABE, E. H., AREDES, M. *Instantaneous Power Theory and Applications to Power Conditioning.* Hoboken, NJ, United States of America, John Wiley and Sons, Inc, 2017.

[51] KAURA, V., BLASKO, V. "Operation of a phase locked loop system under distorted utility conditions", *IEEE Transactions on Industry Applications*, v. 33, n. 1, pp. 58–63, 1997. doi: 10.1109/28.567077.

[52] S. ZHOU, LIU, J., ZHANG, Y. "A decoupling method based on reference current feedforward for DQ-frame PI current control of grid-connected voltage source converters". In: *2015 IEEE 2nd International Future Energy*

Electronics Conference (IFEEC), pp. 1–6, 2015. doi: 10.1109/IFEEC.2015.7361405.

[53] ZHOU, J. Z., DING, H., FAN, S., et al. "Impact of Short-Circuit Ratio and Phase-Locked-Loop Parameters on the Small-Signal Behavior of a VSC-HVDC Converter", *IEEE Transactions on Power Delivery*, v. 29, n. 5, pp. 2287–2296, 2014. doi: 10.1109/TPWRD.2014.2330518.

[54] ROSSO, R., ANDRESEN, M., ENGELKEN, S., et al. "Analysis of the Interaction Among Power Converters Through Their Synchronization Mechanism", *IEEE Transactions on Power Electronics*, v. 34, n. 12, pp. 12321–12332, 2019. doi: 10.1109/TPEL.2019.2905355.

[55] ORIHARA, D., SAITOH, H. "Evaluation of battery capacity required for assist of balancing control", *Journal of International Council on Electrical Engineering*, v. 7, n. 1, pp. 119–124, 2017. doi: 10.1080/22348972.2017.1324273.

[56] ZHANG, L., HARNEFORS, L., NEE, H.-P. "Power-Synchronization Control of Grid-Connected Voltage-Source Converters", *IEEE Transactions on Power Systems*, v. 25, n. 2, pp. 809–820, 2010. doi: 10.1109/TPWRS.2009.2032231.

[57] ZHONG, Q.-C., WEISS, G. "Synchronverters: Inverters That Mimic Synchronous Generators", *IEEE Transactions on Industrial Electronics*, v. 58, n. 4, pp. 1259–1267, 2011. doi: 10.1109/TIE.2010.2048839.

[58] KUNDUR, P. *Power System Stability and Control.* 3412 Hillview Av, Palo Alto, CA, United States of America, McGraw-Hill, Inc., 1994.

[59] ARGHIR, C., JOUINI, T., DÖRFLER, F. "Grid-forming control for power converters based on matching of synchronous machines", *Automatica*, v. 95, pp. 273–282, 2018. ISSN: 0005-1098. doi: https://doi.org/10.1016/j.automatica.2018.05.037.

[60] RABELO, B. C., HOFMANN, W., DA SILVA, J. L., et al. "Reactive Power Control Design in Doubly Fed Induction Generators for Wind Turbines", *IEEE Transactions on Industrial Electronics*, v. 56, n. 10, pp. 4154–4162, 2009. doi: 10.1109/TIE.2009.2028355.

[61] CARVALHO, K. *Comportamento de Conmversores Fonte de Tensao e Filtro LCL na Presenca de Harmonicos na Rede.* Tese de Doutorado, Federal University of Rio de Janeiro, 2019.

[62] SADIKU, M., MUSA, S., ALEXANDER, C. *Applied Circuit Analysis.* New York, NY, 10020, United States of America, McGraw-Hilll, 2013.

[63] CLOSE, C. M. *The Analysis of Linear Circuits.* New York, NY, United States of America, Harcourt, Brace and World, Inc, 1966.

[64] NISE, N. *Control Systems Engineering.* 111 River Street, Hoboken, NJ, United States of America, John Wiley & Sons, Inc., 2011.

[65] PAPIC, I., MATVOZ, D., SPELKO, A., et al. "A Benchmark Test System to Evaluate Methods of Harmonic Contribution Determination", *IEEE Transactions on Power Delivery*, v. 34, n. 1, pp. 23–31, 2019. doi: 10.1109/TPWRD.2018.2817542.

[66] ALVES, A. G. P., ROLIM, L. G. B., DIAS, R. F. S., et al. "Online Impedance Estimation for Voltage Source Converters through the Discrete Fourier Transform", *J Control Autom Electr Syst*, v. 32, pp. 1279–1288, 2021. doi: 10.1007/s40313-021-00769-y.

[67] ALVES, A. G. P., ROLIM, L. G. B., DIAS, R. F. S., et al. "Analysis of Grid-Connected VSCs Subject to Voltage Harmonic Disturbances: Prediction and Design Tool of Resonant Controllers", *IEEE Transactions on Energy Conversion*, pp. 1–11, 2022. doi: 10.1109/TEC.2022.3196244.

[68] ALVES, A. G. P., ROLIM, L. G. B., DIAS, R. F. S., et al. "VSC plug-and-play operation using online grid parameter estimation for PI self-tuning", *IET Power Electronics*, v. 13, n. 18, pp. 4359–4367, 2021. doi: 10.1049/iet-pel.2020.0776.

[69] CARVALHO, K. *Comportamento de Conversores Fonte de Tensão e Filtro LCL na Presença de Harmônicos na Rede.* Tese de Doutorado, Federal University of Rio de Janeiro, 2019.

[70] DOUGLAS, B. "The Root Locus Method". `https://www.youtube.com/watch?v=CRvVDoQJjYI&list=PLUMWjy5jgHK3-ca6GP6PL0AgcNGHqn33f&ab_channel=BrianDouglas`, . Accessed: 2022-11-06.

[71] DOUGLAS, B. "Gain and Phase Margins Explained". `https://www.youtube.com/watch?v=ThoA4amCAX4&t=631s&ab_channel=BrianDouglas`, . Accessed: 2022-11-06.

[72] DOUGLAS, B. "What Is Robust Control? | Robust Control, Part 1". `https://www.youtube.com/watch?v=A7wHSr6GRnc&t=5s&ab_channel=MATLAB`, . Accessed: 2022-11-06.

[73] LISERRE, M., BLAABJERG, F., HANSEN, S. “Design and control of an LCL-filter-based three-phase active rectifier”, *IEEE Transactions on Industry Applications*, v. 41, n. 5, pp. 1281–1291, 2005. doi: 10.1109/TIA.2005.853373.

[74] ONS. “Requisitos técnicos mínimos para a conexão às instalações de transmissão”. `http://www.ons.org.br/paginas/sobre-o-ons/procedimentos-de-rede/vigentes`, 2020. Accessed: 2022-11-06.

[75] ZHOU, D., BLAABJERG, F. “Reliability evaluation of power capacitors in a wind turbine system”. In: *2018 IEEE Applied Power Electronics Conference and Exposition (APEC)*, pp. 3264–3269, 2018. doi: 10.1109/APEC.2018.8341570.

[76] SAU-BASSOLS, J., PRIETO-ARAUJO, E., GOMIS-BELLMUNT, O., et al. “Selective Operation of Distributed Current Flow Controller Devices for Meshed HVDC Grids”, *IEEE Transactions on Power Delivery*, v. 34, n. 1, pp. 107–118, 2019. doi: 10.1109/TPWRD.2018.2848547.

[77] KUNG, S. H., KISH, G. J. “Multiport Modular Multilevel Converter for DC Systems”, *IEEE Transactions on Power Delivery*, v. 34, n. 1, pp. 73–83, 2019. doi: 10.1109/TPWRD.2018.2846264.

[78] LI, B., LI, Q., WANG, Y., et al. “A Novel Method to Determine Droop Coefficients of DC Voltage Control for VSC-MTDC System”, *IEEE Transactions on Power Delivery*, v. 35, n. 5, pp. 2196–2211, 2020. doi: 10.1109/TPWRD.2019.2963447.

[79] BARRAL, J. M. M. *An Investigation of an Energy Diverting Converter for HVDC Applications.* Tese de Doutorado, Staffordshire University, 2019.